Fabrication and Application of Light Harvesting Nanostructures in Energy Conversion

by

Peng Hui Wang
B.Sc., University of Victoria, 2008

A Thesis Submitted in Partial Fulfillment
of the Requirements for the Degree of

DOCTOR OF PHILOSOPHY

in the Department of Chemistry

# Supervisory Committee

Fabrication and Application of Light Harvesting Nanostructures in Energy Conversion

by

Peng Hui Wang
B.Sc., University of Victoria, 2008

**Supervisory Committee**

Dr. Alexandre G. Brolo (Department of Chemistry)
**Supervisor**

Dr. Frank van Veggel (Department of Chemistry)
**Departmental Member**

Dr. Matthew Moffitt (Department of Chemistry)
**Departmental Member**

Dr. Chris Papadopoulos (Department of Electrical & Computer Engineering)
**Outside Member**

# Abstract

**Supervisory Committee**

Dr. Alexandre G. Brolo (Department of Chemistry)

**Supervisor**

Dr. Frank van Veggel (Department of Chemistry)

**Departmental Member**

Dr. Matthew Moffitt (Department of Chemistry)

**Departmental Member**

Dr. Chris Papadopoulos (Department of Electrical & Computer Engineering)

**Outside Member**

The production of an efficient and low cost device has been the ultimate goal in the photovoltaic cell development. The fabrication and application of nanostructured materials in the field of energy conversion has been attracting a lot of attention. In this work, applications of surface plasmons (SPs) and photonic nanostructures to the field of energy conversion, specifically in the area of silicon solar cells and lanthanide energy upconversion (UC) luminescence applications were studied. Enhanced power conversion efficiency in bulk (single crystalline) silicon solar cells was demonstrated using an optimized mixture of the silver and gold nanoparticles (NPs) on the front of the cell to tackle the negative effect in the Au NPs plasmonic application. Then, a comparison of identically shaped metallic (Al, Au and Ag) and nonmetallic ($SiO_2$) NPs integrated to the back contact of amorphous thin film silicon solar cells were investigated to solve a controversy issue in literature. The result indicates that parasitic absorption from metallic NPs might be a drawback to the SPs enhancement. A cost-effective fabrication of large area (5x5 $cm^2$) honeycomb patterned transparent electrode for "folded" thin film solar cell application by combining the nanosphere lithography and electrodeposition were realized. Furthermore, the SPs enhanced tunable energy upconversion from $NaYF_4:Yb^{3+}/Er^{3+}$ NPs in nanoslits were also demonstrated, our results shows that the relative red/green emission can be controlled by different plasmonic mode coupling.

# Table of Contents

# List of Tables

# List of Figures

# Acknowledgments

I would like to sincerely thank:

- My supervisor Professor Alexandre G. Brolo for his patience, help and support through the course of this thesis. I would not have been able to do this dissertation without his endless support and advice.
- I would really like to thank to Professor Frank van Veggel, Professor Matthew Moffitt, Professor Dennis Hore, Professor David Steuerman, Professor Byoung-Chul Choi and Dr. Elaine Humphrey for letting me use their equipment. Especially, Professor Frank van Veggel for his supervision for the related project and his kindness for lending me all his equipment. Professor Chris Papadopoulos for introduction of semiconductor theory and applications.
- All the past and current Brolo group members for general support and great discussions, especially, Dr. Meikun Fan, Dr. Jacson Menezes, Dr. Nick Britto Filho, Regivaldo Gomes and Daniel Collins for their help and friendship.
- Adam Schuetze for FIB, SEM training and assistance, Jonathan Rudge for EBL assistance in UVic.
- Our collaborators: Professor Martin Vehse and his group members in Germany; and Professor Walter J. Salcedo for the simulation support in Brazil.
- The instrument shop, chemical store, machine shop, CAMTEC and chemistry department office for their help and assistance.
- NSERC, UVic, BiopSys and IESVic for funding.
- My family for their love, support and encouragement, especially, my wife Yi.
- Everyone who helped me along the way.

# Chapter 1: Introduction

This chapter provides both an introduction to my research goals and a general basic background pertinent to the whole thesis. The general research objective was to explore the application of different types of nanostructured materials in the field of energy conversion. Especially, the work focused on the light trapping problem in solar cells and on the phenomenon of energy upconversion (UC), which can also be relevant in the field of photovoltaics. First, a motivation is given to the context of silicon photovoltaics and their role in energy conversion. Then, the organization of this thesis is presented. Third, the different types of nanomaterial fabrication approaches explored in this thesis are provided: including colloidal nanoparticle (NP) synthesis, nanosphere lithography (NSL), electrodeposition of Zinc oxide (ZnO) and focused ion beam (FIB). Finally, this chapter ends with a brief summary of our contributions to the field of energy conversion.

## 1.1 Research objectives

### 1.1.1 Motivations

Global energy demand is increasing each year; driven by the economic growth in developing countries, especially China. [1] Carbon emission[2] from increasing fossil fuel (mainly from coal, natural gas, and oil) consumption causes more environmental concerns: such as the "greenhouse" effect.[3] Therefore, there is an urgent need for clean and sustainable alternative energy sources. Nuclear power plants[1] can potentially provide huge energy output; however, the safety of their operation and potential dangers are often their main drawback, especially after the 2011 Japan's Fukushima nuclear plant incident. Wind, solar, biofuel and geothermal approaches are generally considered as viable alternative renewable energy strategies.

Among those renewable clean energy sources, solar radiation represents the largest energy flow that enters the earth. After reflection and absorption in the atmosphere, an estimated $1 \times 10^5$ TW hit the surface of the Earth and undergo conversion to all forms of energy used by humans, with the exception of nuclear, geothermal, and tidal energy.[4-6] This is almost 6,000 fold the current total global consumption[1] (~16 TW) of primary energy.[1, 4, 5] Thus, solar energy has the potential of becoming a major component of a sustainable energy system. The light-electricity conversion is a clean process and does not generate any greenhouse gas emission. Multicrystalline silicon and CdTe are the two most widely used photovoltaic technologies in the current market. The current generation of commercial photovoltaic cells are still presents a low efficiency on the light – electricity conversion.[7] The multi-junction photovoltaic cell has high conversion efficiency. However, the relative high cost of multi-junction photovoltaic cells compared to conventional energy still present a drawback to be used widely. There is a wealth of research activity in materials sciences aiming at finding more efficient and low cost alternatives to the silicon-based technology.[8-10] Thin-film photovoltaic such as $Cu(InGa)Se_2$ and hydrogenated amorphous silicon (a-Si:H) and other merging new technologies such as organic, perovskite cells[11, 12] have been attracted much attentions.

Besides different types of photovoltaic technology, there are many approaches to improve the efficiency of photovoltaic cells. Generally, the design principles of an

efficient photovoltaic cell including: optimizing optical property, minimizing recombination, maximizing charge collection. In this thesis, the focus is only on improving the optical properties of silicon photovoltaics. These included the integration of light trapping nanostructures that supports either surface plasmons (plasmonics)[13-19] or photonic effects.[20-24] in thin film solar cells and the investigation of energy upconversion.[6, 25-29] The plasmonic approach involved the utilization of metallic nanoparticles (NPs) to enhance the light energy conversion.[20, 30-32] Successful implementation of metallic NPs for enhanced performance in photocatalytic[33, 34] and photoelectrochemical[35] devices has been demonstrated, and several comprehensive reviews have been published recently.[20, 30-32] The proof-of-concept of lanthanide up/down energy conversion nanoparticles in solar cell application have also been reported [6, 25, 28] to harvest light lower/higher in energy than the band gap of a silicon photovoltaics.

### 1.1.2 The general objectives

The main objectives of this research project are: (1) to explore cost-effective alternatives to incorporate new types of light harvesting materials in the field of energy conversion applications; (2) to compare the effect of nanostructures that support surface plasmons and photonics effects systematically in terms of the enhanced light absorption and scattering in photovoltaics; (3) to investigate the surface plasmons roles in the upconversion effect.

## 1.2 Organization of this thesis

This thesis is divided into 4 parts: **(I)** the introduction; **(II)** SPs/photonics enhanced light trapping for photovoltaic application; **(III)** SP tuned energy upconversion from $Yb^{3+}$-$Er^{3+}$ codoped sodium yttrium fluoride ($NaYF_4$:$Yb^{3+}$/$Er^{3+}$) nano-crystal coupled with gold nanostructures; **(IV)** a summary and outlook.

Other than the introduction, summary and outlook chapters, each chapter is a paper that has been either published or submitted. Supporting information for each corresponding chapter (paper) was also included in the appendix.

**Part I** (chapters 1 and 2) is intended to provide some general background of the topics involved in this thesis for readers from different disciplines.

Chapter 1 provides a broad overview of the SP-based research projects and introduces the different types of nanostructure fabrication methodologies applied in parts II and III (Chapter 3 to 6): such as colloidal nanoparticle (NP) synthesis (Chapter 3); nanosphere lithography (NSL, chapter 4 and chapter 5); electrodeposition (Chapter 5); and focused ion beam (FIB, chapter 6) fabrication.

Chapter 2 provides the general basic background of the silicon solar cell and upconversion system and the definitions that were used to characterize the performance of the photovoltaics and UC photoluminescence.

**Part II** includes 3 chapters (chapter 3, 4 and 5) that relate to different types of nanostructured materials application in silicon photovoltaic cells. Random (chapter 3) and well organized (chapter 4) metallic NPs were investigated in the front and back of photovoltaic cells, respectively. Chapter 5 demonstrates a cost-effective fabrication of honeycomb patterned transparent electrode for the folded photovoltaic cell concept.

Chapter 3 presents the optimization of plasmonic silicon photovoltaics with Ag and Au nanoparticle mixtures in the front end of the cell. This chapter is a systematic investigation on how the two types of plasmonic NPs (Au and Ag) can be used to minimize a negative effect (decreasing external quantum efficient (EQE)) previously observed from plasmonic NPs integrated in photovoltaics. This negative effect was successfully minimized by adding silver NPs to the surface of an Au NPs-modified PV device. A maximum ~6% EQE enhancement (relative to a textured reference) was observed for PV devices modified with a mixture of metallic nanoparticles (Ag and Au) at the localized surface plasmon resonance (LSPR) wavelengths, and an overall increase in the white light power conversion efficiency of ~5% was obtained.

Chapter 4 focused on experimental and computational comparison of identically shaped and well-organized metallic (Al, Au and Ag) and non-metallic ($SiO_2$) NPs integrated to the back contact of amorphous silicon solar cells (a-Si:H). Our results show comparable performance for both samples, suggesting that minor influence arises from the nanoparticle material. Particularly, no additional beneficial effect of the plasmonic

features due to metallic nanoparticles could be observed. Our findings confirm that the interface textures are the main contribution for light trapping in this solar cell configuration.

Chapter 5 demonstrates a low-cost and scalable bottom-up approach to fabricate nanostructured thin-film solar cells. A folded solar cell with increased optical absorber volume was deposited on honeycomb patterned zinc oxide nanostructures, fabricated in a combined process of nanosphere lithography and electrochemical deposition. The periodicity of the honeycomb pattern can be easily varied in the fabrication process, which allows structural optimization for different absorber materials. The implementation of this concept in amorphous silicon thin-film solar cells with only 100 nm absorber layer was demonstrated. The nanostructured solar cell showed approximately 10% increase in the short circuit current density compared to a cell on an optimized commercial textured reference electrode. The concept presented here is highly promising for low-cost industrial fabrication of nanostructured thin-film solar cells, since no sophisticated layer stacks or expensive techniques were required.

**Part III** is related with SPs tuned energy upconversion (UC) from $Yb^{3+}$-$Er^{3+}$ codoped sodium yttrium fluoride ($NaYF_4$:$Yb^{3+}$/$Er^{3+}$) nano-crystal coupled with gold nanostructures (chapter 6).

In chapter 6, enhanced (maximum ~6 times) upconversion (UC) emission was experimentally demonstrated using gold nanoparticles double antennas coupled to nanoslits in gold films. The transmitted red emission from UC ytterbium ($Yb^{3+}$) and erbium ($Er^{3+}$) co-doped sodium yttrium fluoride ($NaYF_4$:$Yb^{3+}$/$Er^{3+}$) nanoparticles (UC NPs) at ~665 nm (excited with a 980 nm diode laser) was enhanced relative to the green emission at ~550 nm. The relative enhanced UC NPs emission could be tuned by the different polarization-dependent extraordinary optical transmission (EOT) modes coupled to the gold nanostructures. Finite-difference time-domain (FDTD) calculations suggest that the preferential enhanced UC emission was related to a combination of different surface plasmon (SP) modes excitation coupling to cavity Fabry-Perot (FP) interactions.

**Part IV** (chapter 7) is the summary of this thesis. The main results from part II and III are summarized, discussed and connected in the same big picture: enhanced energy conversion. In the meantime, future research directions for the related work are proposed.

## 1.3 General background

Each of the results chapters (parts II and III) has its own introduction. However, some common general information and experimental details are presented here (Part I). This information includes some basic physics of SP (chapter 1.3) and the nanostructure fabrication methodologies (chapter 1.4). Moreover, general background information in plasmonic-enhanced light trapping in photovoltaic and upconversion will be briefly reviewed in chapter 2.

### 1.3.1 The physics of surface plasmon (SPs)

The collective free electrons oscillation at metal surface induced by external electromagnetic field is referred as surface plasmon resonance (SPR).[36, 37] SPR is an interfacial phenomenon, where the electrical field at the metal surface is larger (enhanced) compared to the incoming excitation electric field. In the case of silver, gold and copper nanoparticles, this SPR response can be tuned in the optical visible range by manipulating the geometry and dielectric medium at the metal surface.[37] The light interaction with metallic nanostructures may result in two different types of surface plasmons: the localized surface plasmon (LSP) and the propagating surface plasmon (also known as surface plasmon polaritons (SPPs)).

### 1.3.2 Localized surface plasmon (LSP)

The optical excitation of the LSP can be performed through nanoparticles coupling with the incident light.[37] This type of SP is spatially stationary and does not propagate parallel to the metal surface.

Figure 1−1a illustrates the metallic particle electron cloud oscillation excited by the electric field from the incident light.[37] One of the important general characteristics of SPs is that the enhanced electric field decays exponentially away from the metal dielectric interface.[36]

Figure 1−1b shows that the enhanced electric field is bonded to the interface and decay exponentially away from the surface.

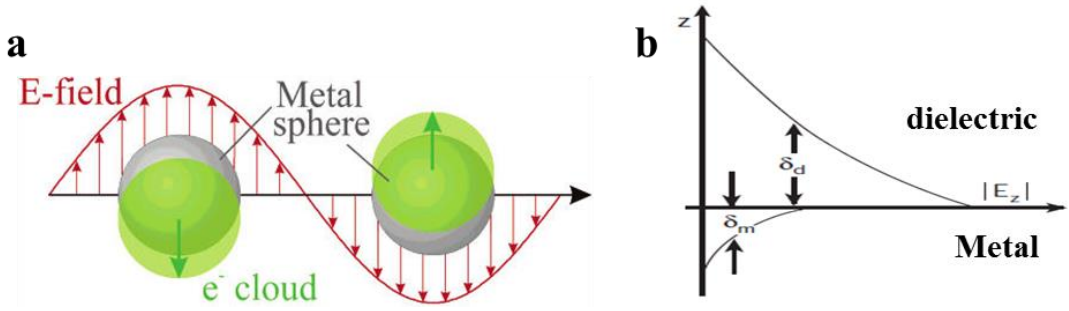


**Figure 1−1** (a) excitation of SPR by the electric field from an incident light[37](Reprinted with permission,[37] copyright 2003, American Chemical Society) (b) the SP electric field decay exponentially away from the metal dielectric interface[36] (reproduced with permission,[36] copyright 2003, Nature Publishing Group).$\delta_d$ and $\delta_m$ are the decay lengths in dielectric and metal, respectively.

The interaction of the electromagnetic field with metal structures can be calculated by solving the Maxwell's equations.[38, 39] Mie[40] presented a solution to Maxwell's equations that describes spherical particle extinction (extinction = scattering + absorption) in 1908. The response of a small metallic sphere (<100 nm in diameter) to an external electromagnetic field is described by the dipole oscillating electric field. The efficiency (Q) of this radiating dipole is given[37] by

$$Q_{ext} = 4x\ Im(g_d) \tag{1-1}$$

$$Q_{sca} = \frac{8}{3}x^4|g_d| \tag{1-2}$$

Where, $g_d = \frac{\varepsilon_i - \varepsilon_o}{\varepsilon_i + 2\varepsilon_o}$, $\varepsilon_i$ and $\varepsilon_o$ is wavelength-dependent dielectric constant of the metal particle and of the surrounding medium, respectively; $x = 2\pi a(\varepsilon_o)^{1/2}/\lambda$, $a$ is the radius of the sphere.

For larger particles (> 100 nm in diameter), higher multiples, especially the quadrupole mode become more important for the observed extinction and scattering spectra. The extinction and Rayleigh scattering efficiencies[37] relations (dipole + quadrupole) are:

$$Q_{ext} = 4xIm\left[g_d + \frac{x^2}{12}g_q + \frac{x^2}{30}(\epsilon_i - 1)\right] \quad (1\text{-}3)$$

$$Q_{sca} = \frac{8}{3}x^4\left\{|g_d|^2 + \frac{x^4}{240}|g_q|^2 + \frac{x^4}{900}|\varepsilon_i - 1|^2\right\} \quad (1\text{-}4)$$

Where, $g_q = \frac{\varepsilon_i - \varepsilon_o}{\varepsilon_i + 3/2\varepsilon_o}$.

### 1.3.3 Surface plasmon polaritons (SPPs)

These types of SPs propagate parallel to the surface upon excitation. The optical excitation of SPPs has historically been performed through prism coupling[41] (Figure 1−2a Kretschmann configuration). Recently, other highly efficient coupling approaches involving metallic subwavelength holes[42] and slits have been studied. A SPPs mode is also highly localized at the metal surface, but it can propagate for several micrometers parallel to the surface. The surface wave is based on the coupling between the surface free charges along the metal and light.[29] The dispersion relation is given by:

$$k_{spp} = \frac{w}{c}\sqrt{\frac{\varepsilon_m \varepsilon_d}{\varepsilon_m + \varepsilon_d}} \quad (1\text{-}5)$$

Where, $k_{spp}$ is the wavevector of SPP, ω is angular frequency, c is the speed of light, $\varepsilon_m$ is the dielectric constant for metal and $\varepsilon_d$ is the dielectric constant for dielectric.

Figure 1−2b presents SPPs excitation by momentum matching in the prism-coupling SPR;[41] besides the prism coupling excitation, another technique to excite SPPs is the grating coupling method. In Figure 1−2b, a schematic of periodic corrugated metallic surface with one-dimensional (1D) grating is shown and the condition for the SPP excitation is expressed[29, 41] as

$$K_{spp} = k_{x\,in} + \Delta k_x \quad (1\text{-}6)$$

$$\text{Where, } \Delta k_x = m\left(\frac{2\pi}{\Lambda}\right) \qquad m = \pm 1, \pm 2, \ldots \quad (1\text{-}7)$$

Where $k_{x\ in}$ is the x component of the incident light wavevector given by $k_{x\,in} = (\omega/c)\sqrt{\varepsilon_m}\sin\theta_{in}$.

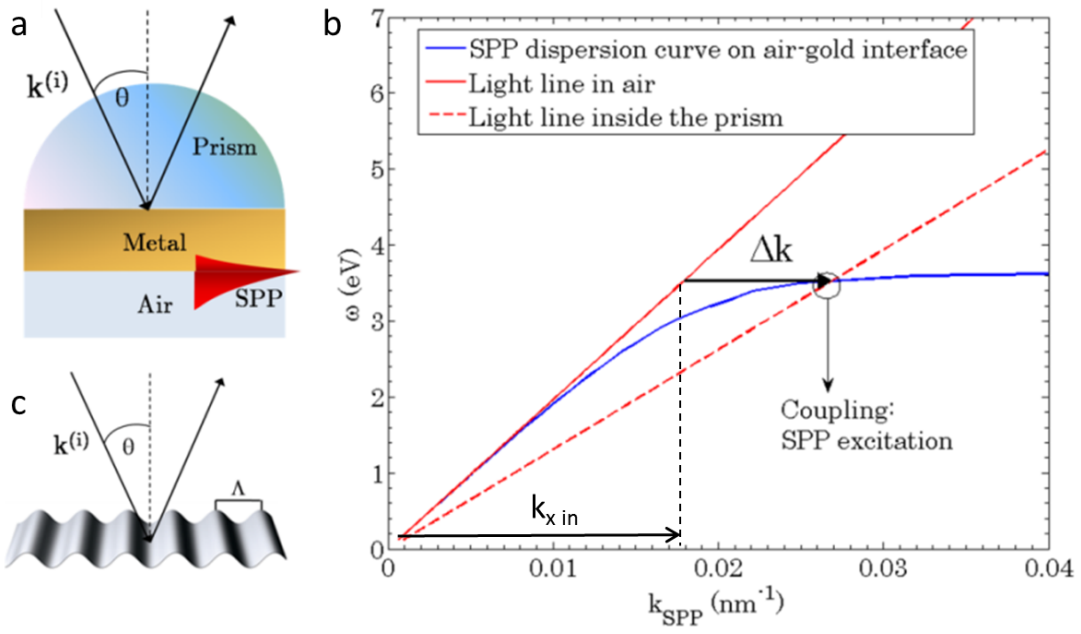


**Figure 1−2** Kretschmann configuration (b) SPPs excitation by momentum matching in prism coupling (c) Schematic of the light incident on a 1D metallic grating (reproduced with permission from InTech-Open Access Company[41]).

The right hand side of the equation (1-6) represents the x-component of the *m*th order of diffracted light. It can be seen that in equation (1-6), by adding the grating quasi-wavevector $\Delta k_x$ to the incident $k_{x\ in}$, a matching condition for the $k_{spp}$ would be satisfied the momentum is conserved.

## 1.4 Surface plasmon material/substrate fabrications approaches

### 1.4.1 Colloidal nanoparticle synthesis and immobilization

The nanoparticle-based application that takes advantage of LSP resonance could be dated back from the ancient Roman. For example, Ag nanoparticles were found to be responsible for the different optical color effects in the famous Lycurgus cup. The stained windows of churches also utilize the LSP from the trace amounts of Ag/Au nanoparticles mixture to produce colors.[43] Modern chemistry synthesis allows the material, size, and shape of the nanoparticle to be controlled. Ag/Au colloidal nanoparticles are commonly synthesised according to the Turkevich method;[44-46] i.e., through reducing the silver/gold salts by citrate. The different sizes of the Ag/Au NPs can be obtained by utilizing different amount of NPs seeds and reducing agents (hydroquinone was used to grow Au NPs in Chapter 3). The general chemical reactions are showed below:

*Ag NP ($Ag^o$) synthesis:*

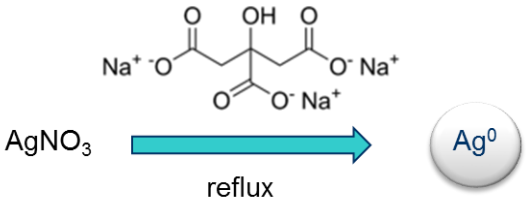


(1-8)

*Au NP ($Au^o$) seed synthesis:*

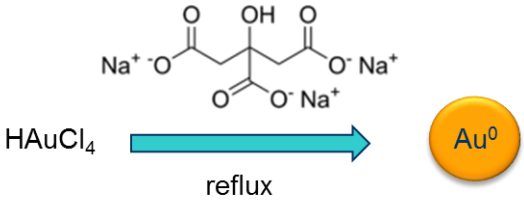


(1-9)

*Growth of Au NP ($Au^o$) seed with hydroquinone reducing agent:*[47, 48]

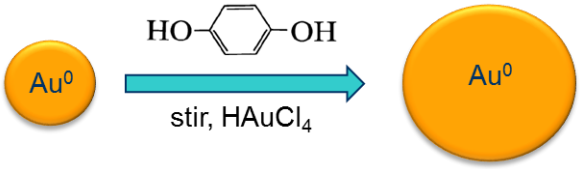


(1-10)

After colloid preparation, the individual NPs can be easily immobilized on a substrate. Figure 1−3 shows a scheme of NPs can be immobilized onto a silicon solar cell surface using a self-assembled monolayer (SAM) of 3-aminopropyltrimethoxysilane (APTMS) as a linker molecule. The application of NPs modified silicon solar device is shown in chapter 3.

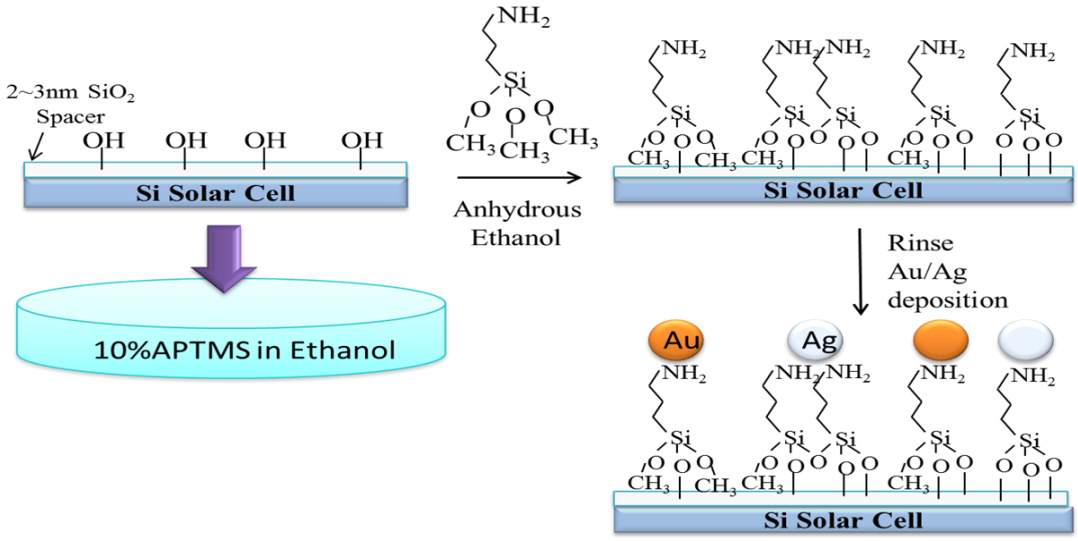


**Figure 1−3** Schematic of NPs immobilization on an APTMS modified silicon solar cell.

### 1.4.2 Nanosphere Lithography (NSL)

Nanosphere lithography (NSL) is a fabrication method that can provide large area nanostructure patterning at low-cost,[49, 50] since it does not require chemical etching and other more complex fabrication steps. NSL process have been used in making different nanostructured patterns: such as subwavelength holes,[51, 52] antireflection nanostructures,[50, 53] organized nanoparticles[54] and textured back electrode[55].

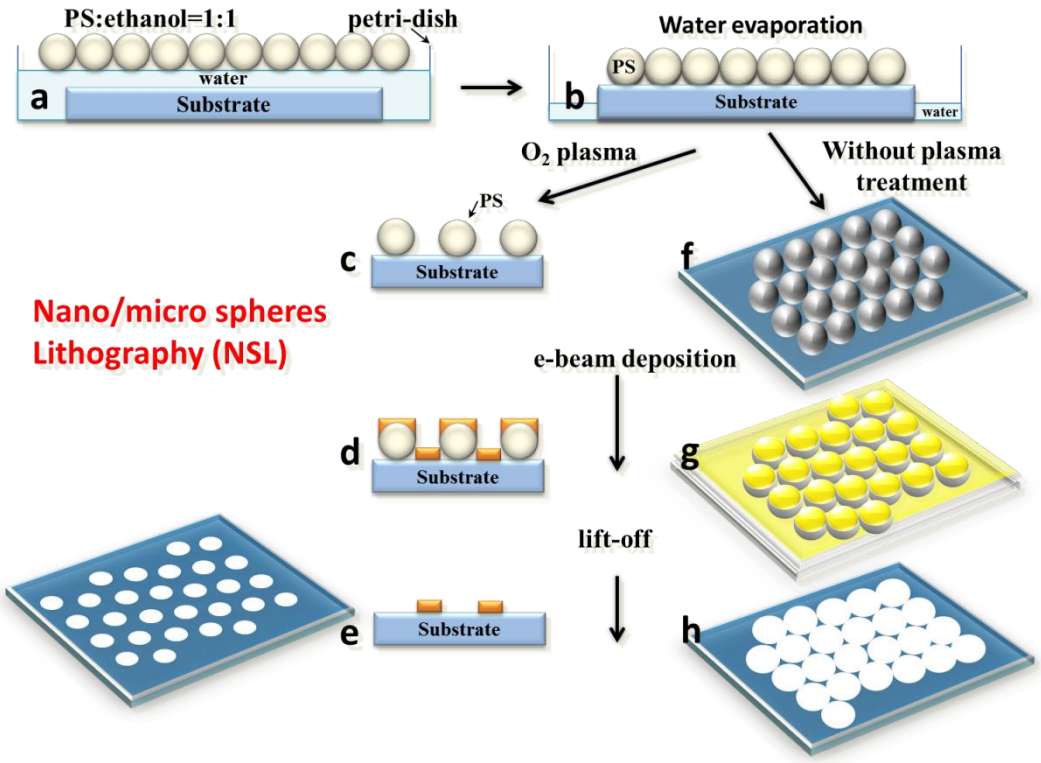


**Figure 1−4** Schematic of NSL process for metallic holes and NPs fabrication.

Figure 1−4 shows a general scheme of the NSL fabrication. The route II was applied in chapter 4 to fabricate NPs with the identical geometry and size but with different materials. A polystyrene (PS) nanospheres (different sizes were used): ethanol (1:1 v/v) mixture were dropped onto a water surface to create a SAM of nanospheres (a), and then, the excess water was drained slowly and allowed water to evaporate from the top of a substrate (b). This PS nanosphere layer served as a mask on the substrate surface. The PS mask could be modified with either route I or II:

Route I: the substrate is treated with oxygen plasma to make the PS nanosphere to shrink (c), metallic/dielectric material is evaporated on the top of the substrate (d), the PS mask that coated with metallic/dielectric material in toluene with sonication is removed, metallic/dielectric holes are formed on the substrate (e). The periodicity of holes can be controlled by the particular PS nanosphere diameter, and the diameter of holes can be controlled by the time of plasma treatment.

Route II: the substrate is used directly without $O_2$ plasma treatment (f). After PS nanosphere deposition, metallic/dielectric material is evaporated on the top of the substrate (g), and the evaporated material coats the surface of the substrate and also fills up the voids between the PS nanospheres. After removing PS mask that coated with metallic/dielectric material in toluene ("lift-off"), the metallic/dielectric particles are left on the substrate (h). The size, shape of the metallic/dielectric nanoparticles can be controlled by the PS mask voids, PS nanosphere diameter, and evaporated thickness.

### 1.4.3 Electrodeposition of Zinc Oxide (ZnO)

By applying the PS mask on the ZnO seeded substrate (section 1.4.2), nanostructured substrate could be also realized by ZnO electrodeposition process. Electrodeposition is a process broadly used in industries to deposit material by applying potential across electrodes. ZnO is a transparent (direct bandgap, 3.3 ~ 3.5 eV) n-type semiconductor[56]. ZnO is considered a good candidate for transparent conductive oxide (TCO) material compared to the expensive indium tin oxide (ITO). Figure 1−5 illustrates the experimental setup for the ZnO electrodeposition in Chapter 5. The ZnO seeded substrate (working electrode) is immersed in an electrolyte of 0.5 mM $ZnCl_2$ and 0.1 M KCl oxygen saturated water solution at 80 $^oC$. The deposition is in a standard three electrodes configuration with an $Ag|AgCl|Cl^-_{(3M)}$ reference and a Pt counter electrode. The cathodic electrodeposition of ZnO crystal result from the reduction of dissolved molecular oxygen in a zinc chloride solution. The general reaction mechanism can be summarized as: [56-59]

$$\frac{1}{2}O_2 + H_2O + 2e^- \rightarrow 2OH^- \quad (1\text{-}11)$$

$$Zn^{2+} + 2OH^- \rightarrow ZnO + H_2O \quad (1\text{-}12)$$

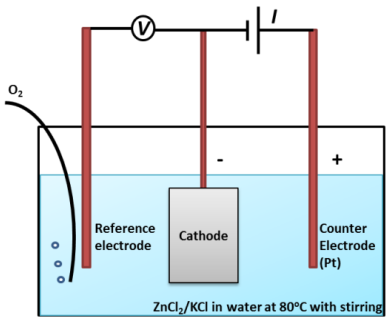


**Figure 1−5** Schematic of electrodeposition cell configuration for ZnO

### 1.4.4 Focused Ion Beam (FIB)

NSL is a bottom-up technique for preparing nanopatterned substrate that used in Chapter 4 and 5. FIB is a direct patterning technique that uses a focused beam of $Ga^+$ ions to write designed pattern onto a substrate. FIB is often used in the fabrication of solid state devices,[60] and preparation of transmission electron microscopy (TEM) specimens[61, 62] as a top-down technique for preparing nanopatterned substrate. This technique was mainly developed about 40 years ago, in the late 1970s and the early 1980s.[62]

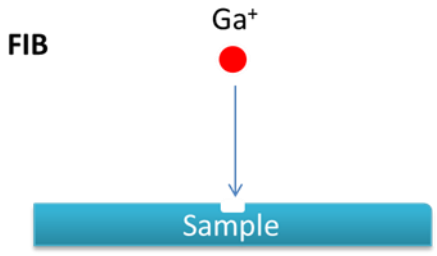


**Figure 1−6** Schematic of FIB process

Figure 1−6 illustrate the main aspect of the technique. When energetic $Ga^+$ ions are accelerated and hit a sample surface, they lose their energy to the electrons and atoms of the solid sample. The sample's material (atoms) can be knocked off (sputtered) from the surface.[62] Through scanning the focused ions beam on the sample surface, the designed pattern can be etched. The main benefits of the FIB fabrication are that the high spatial resolution (below 10 nm for milling), and the high flexibility with the shapes of the fabricated structures. In addition, FIB milling was also used to generate cross section cuts in chapters 4 and 5 to study the a-Si:H solar cell film stacking. An arbitrary nanostructure, gold double antenna nanostructures nested inside slits, was fabricated and investigated in this thesis (Chapter 6). The high cost and long processing time are often big drawbacks for the FIB method, especially for large area fabrications (>100 µm).

## 1.5 What are our contributions?

Enhanced energy conversion has attracted a lot of research attention in the past decades. Nanotechnology is one of the driving forces in this area. Our research results

offer new insights in the plasmonic/photonic enhanced photovoltaic and energy upconversion applications.

For example, the different plasmonic materials could be integrated as antireflection coating to improve the light trapping in silicon solar cell (Chapter 3). Furthermore, we experimentally compared different type of metallic and dielectric NPs on the back of the thin-film a-Si:H solar cell (Chapter 4). Our results indicated that the surface texturing was more important than the field enhancement in the thin-film a-Si:H solar cell. A cost-effective and feasible on large scale approach for pattering the transparent electrode is realized in a combined process of nanosphere lithography and electrodeposition (Chapter 5). The concept is highly promising for an industrial fabrication of nanostructured thin-film solar cells with excellent optical performance. In addition, we also experimentally demonstrated that the enhanced upconversion emission could be tuned by the different SPR modes and polarizations in a nanoslit structure (Chapter 6).

# Chapter 2: Light Management in Silicon Photovoltaics

This chapter provides a general background, including: a brief overview of fundamental of semiconductors; silicon photovoltaic operation and characterization methods; plasmonic light trapping; the concept of “folded” solar cell designs; and energy upconversion.

## 2.1 Introduction

Photovoltaic (PV) devices are the technology used for direct generation of electricity from solar radiation. PV effect is the electric charge or current creation and collection under light illumination.[63] Although silicon solar cell is widely utilized in the market[64, 65], there are many other different kinds of solar cells. The current best research solar cells (National Renewable Energy Laboratory (NREL), certified) are listed in Figure 2−1 below.[66] Note that the theoretical maximum energy conversion efficiency for a crystalline silicon solar cell with a bandgap energy ($E_g$) of 1.1 eV is about 30%. This is known as the Shockley-Queisser limit.[67] The Shockley-Queisser limit is a theoretical maximum efficiency that a single p-n junction solar cell can achieve. The efficiency is limited primarily by three factors: blackbody radiation, radiative recombination and spectrum losses.

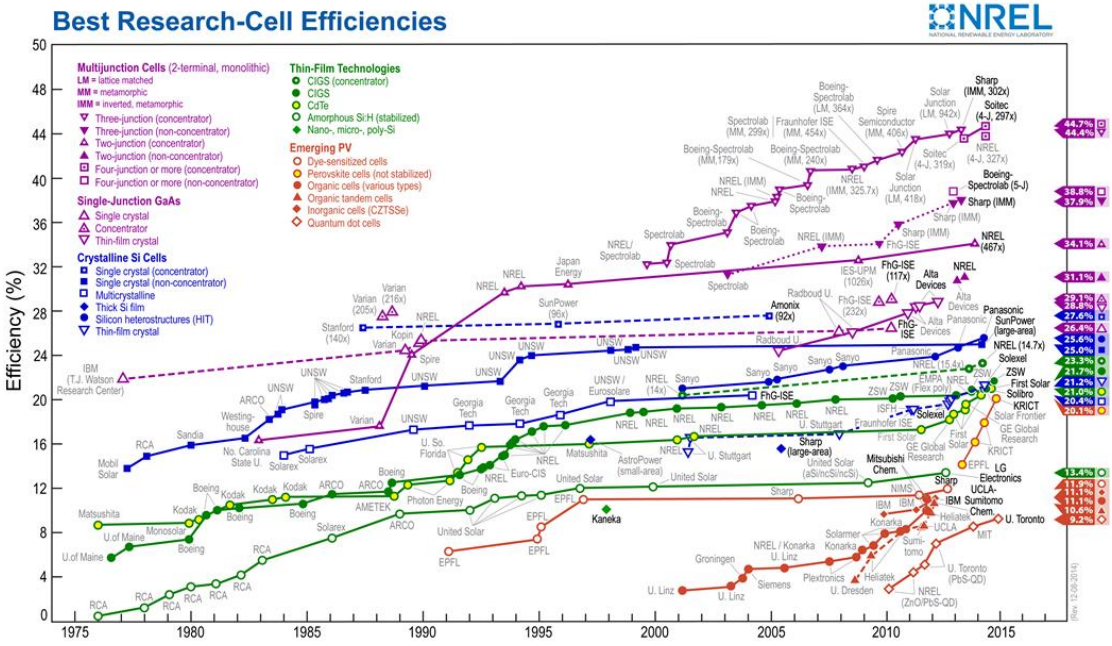


**Figure 2−1** Best research-cell efficiencies achieved in the research labs (this plot is courtesy of the National Renewable Energy Laboratory, Golden, CO.)

## 2.2 Solar spectrum

The sun emits a wide range of electromagnetic radiation in terms of energy and wavelength. The relation between a photon energy ($E$) and its wavelength ($\lambda$) is given by the equation:

$$E = \frac{hc}{\lambda} \qquad (2.1)$$

where $h$ is the Planck's constant and $c$ is the speed of light.

The sunlight that enters the earth atmosphere is just a small fraction of the total energy emitted by the sun. The solar spectrum that reaches the earth surface is different than in outer space, due to atmospheric absorption, scattering and reflection. A typical standardized solar spectrum is defined as AM1.5G (AM is the air mass and G strands for "global", and includes both direct and diffuse light) with a power density of 1kW/m$^2$ that is used for evaluating the performance of solar cells. Figure 2−2 presents[26] the fraction of AM1.5G spectrum currently utilized by the commercial bulk silicon devices, and the additional spectral region that can potentially be used for up and down conversion (UC and DC respectively).

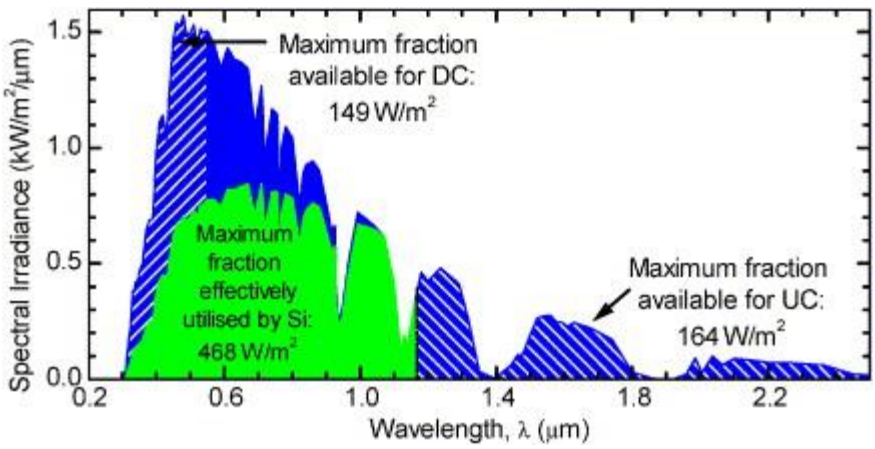


**Figure 2−2** A typical AM1.5G spectrum that utilized by the bulk silicon PV device and the additional spectrum regions that can be utilized for up and down conversion[26] (UC and DC on the graph, respectively. Reproduced with permission, copyright 2006, ELSEVIER B.V)

### 2.3 The operating principle of photovoltaics

The fundamental operating principle of PV is based on the conversion of the electromagnetic energy into electrical energy that is known as "photovoltaic effect".[6] How the electrons are filled in a material' orbitals often determine whether a material is a metal; or, an insulator. Figure 2−3 illustrates a simple schematic of energy band diagram of a metal and semiconductor. The band (electronic states) filled with electrons is called

valance band ($E_v$) and the unfilled band is called conduction band ($E_c$). The energy gap between the $E_v$ can $E_c$ is called bandgap ($E_g$).

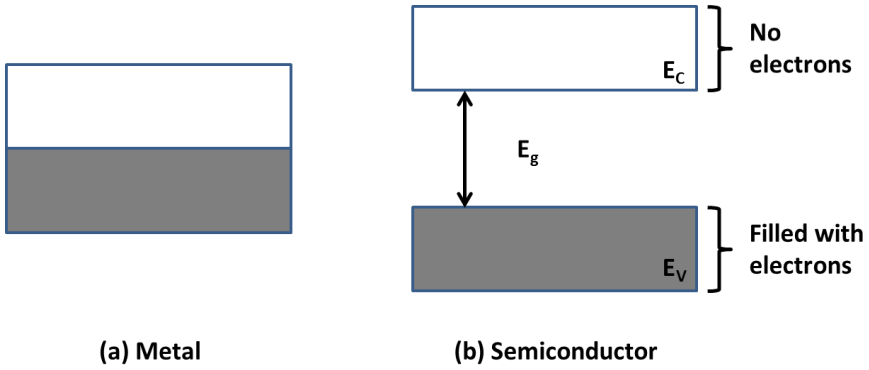


**Figure 2−3** Schematic simple illustration of energy band of a metal (a) and semiconductor (b)

Note that semiconductors is typically with an energy band gap ($E_g$) that is in the range of a few eV or less, if $E_g$ is large (4-12ev), then a material is considered as an insulator.[68] A photon with energy ($E_{ph}$) larger than the semiconductor bandgap ($E_g$) is able to excite the electrons from the $E_v$ to $E_c$ to generate electron hole pairs. After electrons have been excited to the $E_c$, the vacant states left in the valence band are called "holes". In an intrinsic (undoped) material (silicon for example), the number of electrons in the conduction band is equal to the number of holes in the valence band. The silicon is often doped with different impurities to have the concentration of one type of carrier (either electrons or holes) greater than the other. This is achieved by doping the Si crystal with impurity atoms that either donate electrons to the conduction band or accept electrons form the valence band. When electrons are the dominant carrier (typically doped with group V atoms: P, As, Sb), the semiconductor is called n-type; when holes are the dominant carriers, (typically doped with group III atoms: B, Al, Ga, In), the semiconductor is called p-type. When the n-type and p-type doped material are brought together a "p-n junction" is formed. As the two regions are brought together, there is transfer of carriers to achieve thermal equilibrium. This leads to a "depletion layer" or "space-charge" region near the interface, caused by the uncompensated impurity ions that remain. Therefore, an internal electric field is formed at this p-n junction[69] as show in Figure 2−4.

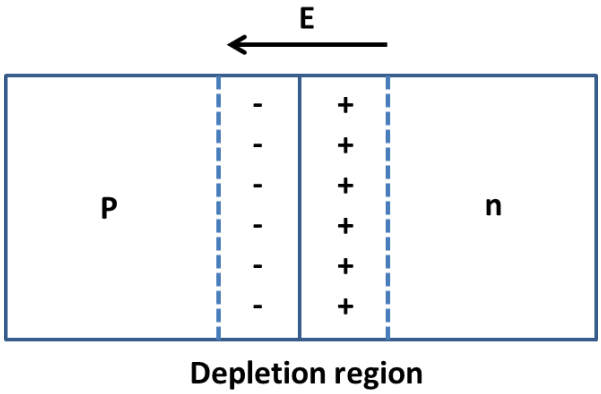


**Figure 2−4** a p-n junction is formed by jointing n-type and p-type semiconductor material.

In this thesis, two types of silicon solar cells are investigated. One is the crystalline silicon solar cell (c-Si); and the other is the hydrogenated amorphous silicon (a-Si:H) solar cell . c-Si solar cells are widely used and commercially available. They often have a very thick (200~300 μm) absorption layer. On the other hand, a-Si:H solar cells are very thin (100~500 nm) and they are often used as a front absorber. The schematic of the cell configuration and energy diagrams for both types of solar cells are presented in Figure 2−5. The main difference between them is that the c-Si solar cell is a diffusion driven type junction (p-n) while the a-Si:H is a field driven junction (p-i-n).[70] When photons with energy greater than the semiconductor bandgap are absorbed, electrons and holes (e-h) pairs are generated in the whole silicon solar cell (Figure 2−5a). If the generation is inside the p-n junction, the electric field at p-n junction rapidly sweeps electrons to the n-side and holes to the p-side. Because of the low defect density in the c-Si, the minority charge carrier generated from the p- and n-layer could diffuse in a long distance (typically 100~300 μm for the diffusion length) to the p-n junction before they recombined.[70] The diffusion is driven by the carrier concentration gradient. When the charge carrier diffuse to the p-n junction, the charge would be also separated by the electric field in the p-n junction. However, in the case of a-Si:H solar cell (Figure 2−5b), due to the high defect density of doped a-Si:H (p- and n-layer), the charge carrier generated inside the p- and n-layer often suffer a strong recombination. Thus, an intrinsic (i-layer) is added between the p-n junction. Therefore, the field driven p-i-n mechanism is

applied in this case. The charge carriers (e-h pairs) are generated inside i-layer and separated instantaneously by the electric field across the i-layer.[70] If the solar cell is connected to the external load, the separated charge carriers can provide power under illumination.

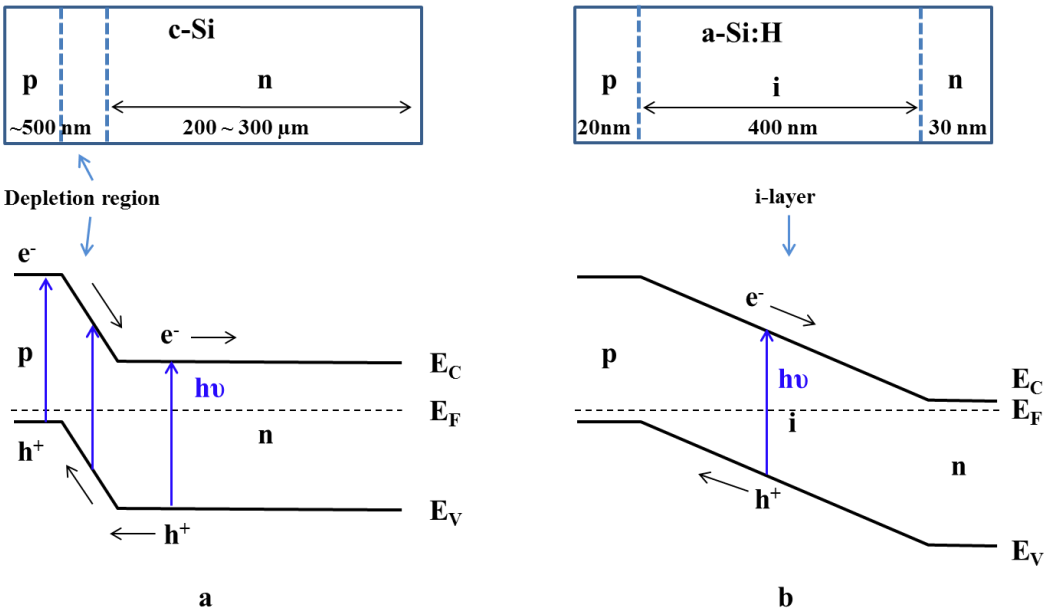


**Figure 2−5** Schematic and of the p-n and p-i-n junctions and energy band diagrams for (a) c-Si and (b) a-Si:H solar cell, respectively.

### 2.1.1 Solar cell parameters

#### Current-voltage (I-V) curve[71]

The performance of a solar cell is characterized by the I-V curve as shown[72] in Figure 2−6. This curve can be obtained by measuring the current under illumination with a voltage sweep applied across the solar cell device. The two points indicated on the I-V curve (Figure 2−6) are very important:

1. ***Short circuit current ($I_{SC}$):*** the maximum current at a zero voltage. $I_{SC}$ is proportional the light intensity.
2. ***Open circuit voltage ($V_{OC}$):*** The maximum voltage at zero current. $V_{OC}$ increases logarithmically with increase light intensity.

The photogenerated current is defined by

$$I = I_L - I_o \left[\exp\left(\frac{qV}{nkT}\right) - 1\right] \tag{2.2}$$

$I$ is the current, $I_L$ is the light generated current, $I_o$ is the dark saturation current, $q$ is the charge on an electron, $V$ is the applied voltage, $k$ is the Boltzmann's constant and, $T$ is absolute temperature, $n$ is the ideality factor.

At I = 0,

$$V_{OC} = \frac{nkT}{q} ln\left(\frac{I_L}{I_o} + 1\right) \tag{2.3}$$

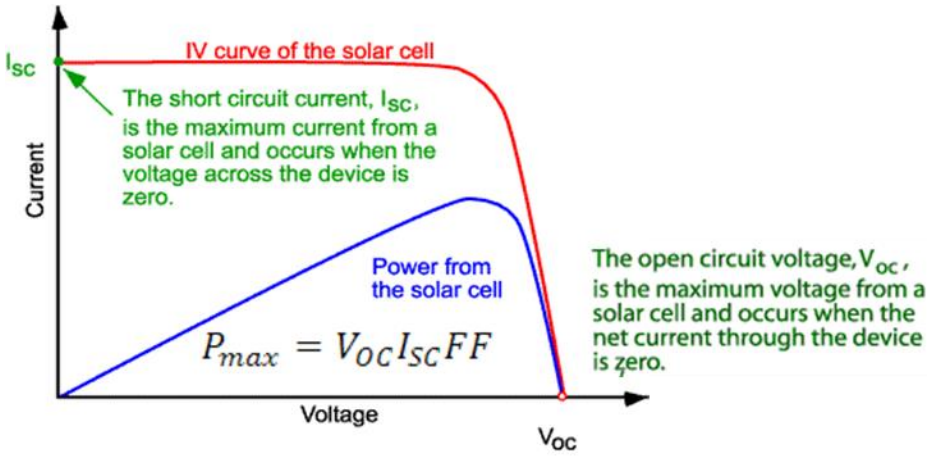


**Figure 2−6** Schematic of a solar cell I-V characteristic under illumination[72] (Reproduced with permission from PVeducation.org[72])

The fill factor (FF) is defined by how rectangular is the I-V curve; and it measures the combination of the p-n junction quality and series resistance of a solar cell.

$$FF = \frac{V_{mp} I_{mp}}{V_{oc} I_{sc}} \tag{2.4}$$

where $V_{mp}$ and $I_{mp}$ is the maximum power ($P_{max}$) point on the I-V curve, when the product of voltage (V) and current (I) is its maximum values. Therefore,

$$P_{max} = V_{oc} I_{sc} FF \tag{2.5}$$

**External quantum efficiency (EQE)**

The external quantum efficiency measure the ratio of the number of charge carriers collected by a solar cell to the number of total incoming photons of a given energy. In an ideal case, the EQE should be close to the unity that means all the incoming photons are covered into charge carriers and all the charge carriers are collect by the external circuit. However, the EQE for most solar cells are less than unity because of the effects of recombination, reflections, and a low diffusion length as illustrated in Figure 2−7.

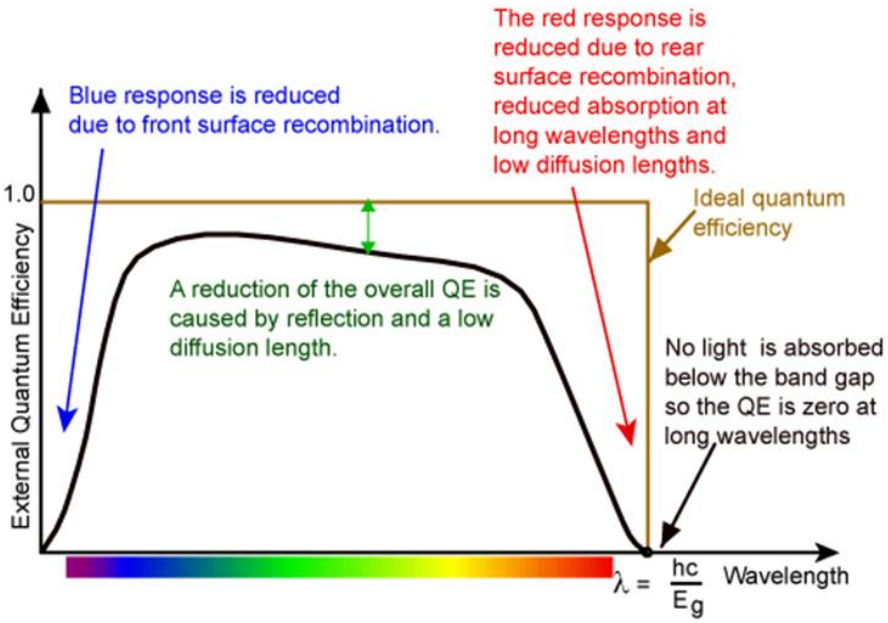


**Figure 2−7** Illustration of EQE curve and the regions that responses were affected in a typical silicon solar cell[72] (reproduced with permission from PVeducation.org[72]).

## 2.3 Light harvesting in a solar cell

Light harvesting in a solar cell is also very important to achieve high light-photocurrent conversion efficiency. In a bulk silicon solar cell, the dominant technology in the market, standard anti-reflection coatings are often optimized for a particular wavelength and incident angle to increase the light path length inside the PV device. In the thin film solar

cells design, the conversional texture method (HF etching) often found to be problematic because the active layer is very thin[4] (range from 100 nm to 1 μm). Most importantly, for thin-film solar cells, the absorbers are not optically thick enough to absorb all incoming light for photocurrent generation. Figure 2−8 shows a spectrum from a 2-μm-thick crystalline Si absorber illuminated with the AM1.5G solar source. The light in the range of 600 ~ 1000 nm is poorly absorbed.[55] Thus, a good light trapping method is crucial to improve the current generated from thin-film solar cells.

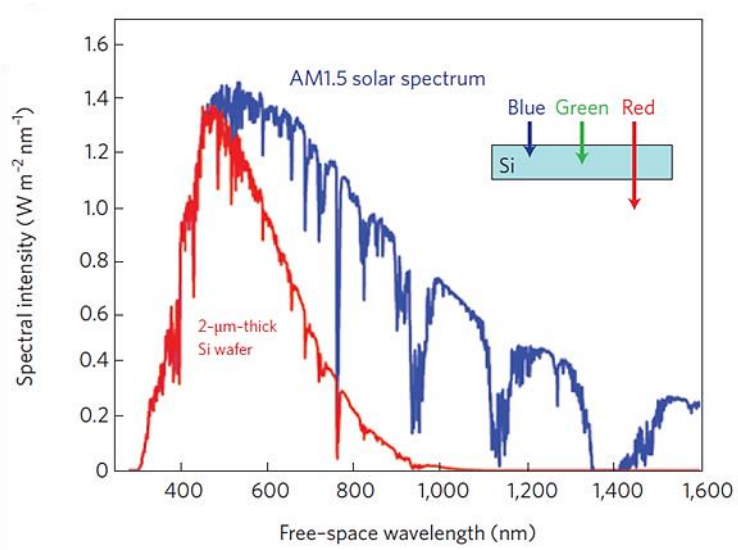


**Figure 2−8** A 2-μm-thick crystalline Si film (assuming single-pass absorption and no reflection) absorption profile with a AM1.5G solar spectrum.[18] (Reproduced with permission,[18] copyright 2010, Nature Publishing Group).

### 2.3.1 Surface plasmon light trapping in thin film photovoltaics

Plasmonic structures offer various ways to increasing the light path length inside the PV absorber layer.[18] Figure 2−9 shows three common SP light trapping strategies in solar cell application. When the NPs are large, the scattering dominates over absorption, then the incidence light can be preferentially scattered into the absorber layer (Figure 2−9a); Figure 2−9b shows the NPs can be used as subwavelength antennas. In this case, the absorber layer can take advantage of the near field concentrated light; Figure 2−9c shows that a structured metallic back surface can support SP modes propagating at the metal/semiconductor interface, trapping the sunlight inside of the absorber layer.[18]

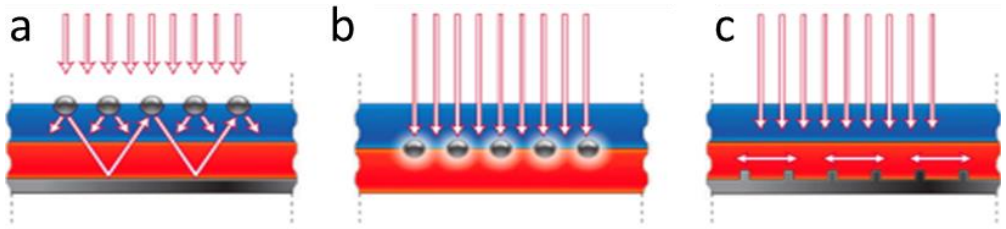


**Figure 2−9** Light trapping by metallic nanostructures[18] (a) scattering; (b) excitation localized SP (c) SP at metal/semiconductor interface. (Reproduced with permission, [18] copyright 2010, Nature Publishing Group). The blue and red region represent p and n layer, respectively.

### 2.3.2 Photonic light trapping in thin film photovoltaics

Besides the SP approaches mentioned above, another way to increase the light path length inside the PV absorber layer is to pattern the solar cell with various dielectric nanostructures.[20, 24, 31, 73] One of the many approaches investigated in the literature is the fabrication of a cost effective "folded" solar cell design. The "folded" solar cell design enables a large optical thickness and a small electrical thickness, which have been pointed out recently by Vanecek et al.[74] Figure 2−10 presents a schematic of the "folded" solar cell design. The absorber layer (a-Si) is packed inside a three-dimensional transparent conductive oxide (TCO) column. Thus, the optical path is increased in the vertical direction and electric thickness in horizontal direction is kept small for the charge collections.

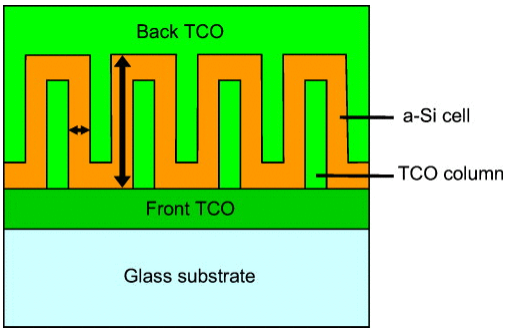


**Figure 2−10** Schematic of a folded a-Si thin film solar cell design, vertical arrow represents the optical thickness and the horizontal arrow represents the electrical thickness (Reproduced with permission,[74] copyright 2011, AIP Publishing LLC) .

### 2.3.3 SP enhanced upconversion for silicon photovoltaics

The typical crystalline silicon solar cell has a band gap about 1.1 eV and 1.7 for amorphous silicon solar cell, which means light energy below the band gap energy will not be converted into useful electricity in a silicon PV. There are two regions in the AM1.5G spectrum that are not utilized by the current silicon PV, as shown above in Figure 2−2. Upconversion (UC) materials have been demonstrated to harvest light lower in energy than the band gap of amorphous silicon PV for the current generation.[75-78] For example, the lower energy photons can be absorbed by $Yb^{3+}$ and then energy transfer to $Er^{3+}$ to generate higher energy photon through radiative emission process (red and green arrows). Then, the emission of the higher energy photon can be used to generate electricity in the amorphous silicon solar cell. Figure 2−11a shows $Er^{3+}/Yb^{3+}$ upconversion mechanism.[79, 80] The red emission corresponds to the $^4F_{9/2} \rightarrow {}^4I_{15/2}$ transition. The green emission is a direct radiative recombination and the red emission is a process with internal interband relaxation. A typical $Er^{3+}/Yb^{3+}$ emission spectrum is shown in Figure 2−11b.

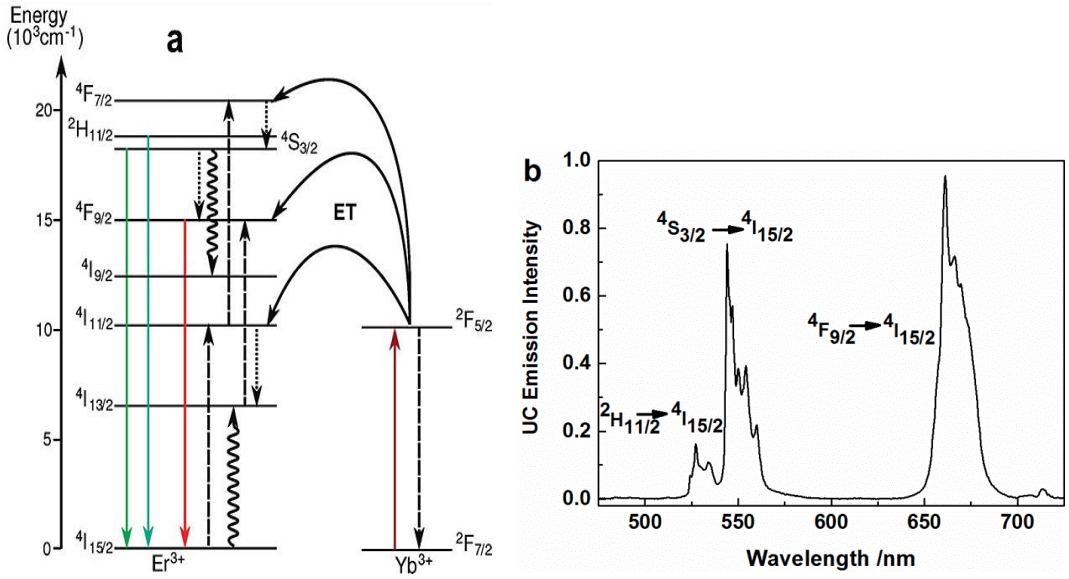


**Figure 2−11** (a) upconversion process for $Er^{3+}$-$Yb^{3+}$ (reproduced with permission, copyright 2010, Royal Society of Chemistry). (b) Emission spectrum of $NaYF_4$:$Er^{3+}/Yb^{3+}$

However, due to the high excitation intensity required and narrow emission peaks, it was not an ideal structure in solar cell applications. However, SPs could be used to

improve upconversion process in PV, either by enhancing the excitation or enhancing the radiative emission process[81] (Figure 2−12). If the SPs are in resonance with the UC material excitation, the enhanced near field at excitation could increase the UC luminescence (Figure 2−12a) that provides more light for a solar cell. If UC material emission is in resonance with AuNPAs, the enhanced directional scattering and near field light localization could also bring more light into the silicon solar cell by coupling SPs nanostructures and UC materials (Figure 2−12b).

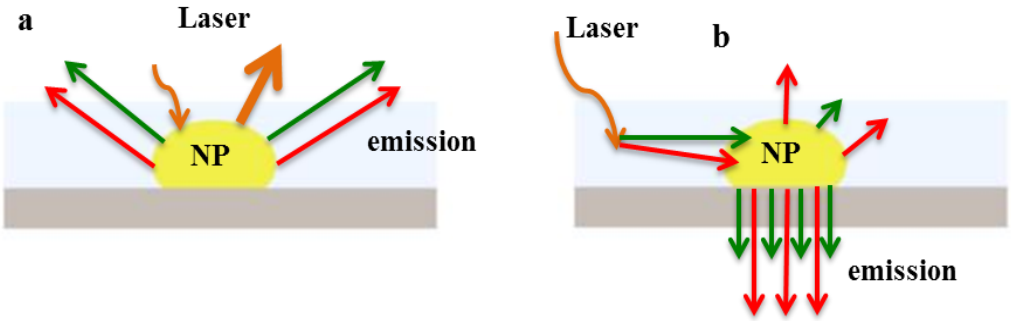


**Figure 2−12** (a) Au NP enhanced excitation; (b) NP enhanced directional UC radiative emission. Representation: laser excitation (orange arrow), emission (green and red color)

## 2.4 Reference

(1) B.P Statistical Review of World Energy. *British Petroleum* 2014.

(2) Ucak, H.; Aslan, A.; Yucel, F.; Turgut, A., A Dynamic Analysis of $CO_2$ Emissions and the GDP Relationship: Empirical Evidence from High-Income OECD Countries. *Energy Sources Part B* **2015,** *10* (1), 38-50.

(3) *Climate Change 2007: The Physical Science Basis*. Cambridge University Press: Cambridge, United Kingdom and New York, NY, USA., 2007.

(4) Bosshard, P., An Assessment of Solar Energy Conversion Technologies and Reserach Opportunities. **2006**.

(5) Richa Khare, S. a. J. P., Energy as a Natural Resource *International Journal of Green and Herbal Chemistry* **2012,** *1* (3), 340-347.

(6) Tanabe, K., A Review of Ultrahigh Efficiency III-V Semiconductor Compound Solar Cells: Multijunction Tandem, Lower Dimensional, Photonic up/down Conversion and Plasmonic Nanometallic Structures. *Energies* **2009,** *2* (3), 504-530.

(7) Miles, R. W.; Hynes, K. M.; Forbes, I., Photovoltaic Solar Cells: An Overview of State-of-the-Art Cell Development and Environmental Issues. *Prog. Cryst. Growth Charact. Mater.* **2005,** *51* (1-3), 1-42.

(8) Strumpel, C.; McCann, M.; Beaucarne, G.; Arkhipov, V.; Slaoui, A.; Svrcek, V.; Canizo del, C.; Tobias, I., Modifying the Solar Spectrum to Enhance Silicon Solar Cell Efficiency - an Overview of Available Materials. *Sol. Energy Mater. Sol. Cells* **2007,** *91* (4), 238-249.

(9) Li, B.; Wang, L. D.; Kang, B. N.; Wang, P.; Qiu, Y., Review of Recent Progress in Solid-State Dye-Sensitized Solar Cells. *Sol. Energy Mater. Sol. Cells* **2006,** *90* (5), 549-573.

(10) Kazmerski, L. L., Solar Photovoltaics R&D at the Tipping Point: A 2005 Technology Overview. *J. Electron Spectrosc. Relat. Phenom.* **2006,** *150* (2-3), 105-135.

(11) Liu, D.; Kelly, T. L., Perovskite Solar Cells with a Planar Heterojunction Structure Prepared Using Room-Temperature Solution Processing Techniques. *Nat Photon* **2014,** *8* (2), 133-138.

(12) Zhou, H., *et al.*, Interface Engineering of Highly Efficient Perovskite Solar Cells. *Science* **2014,** *345* (6196), 542-546.

(13) Sun, Z.; Zuo, X.; Yang, Y., Role of Surface Metal Nanoparticles on the Absorption in Solar Cells. *Opt. Lett.* **2012,** *37* (4), 641-643.

(14) Ferry, V. E.; Polman, A.; Atwater, H. A., Modeling Light Trapping in Nanostructured Solar Cells. *ACS Nano* **2011,** *5* (12), 10055-10064.

(15) Spinelli, P.; Ferry, V. E.; Groep, J. v. d.; Lare, M. v.; Verschuuren, M. A.; Schropp, R. E. I.; Atwater, H. A.; Polman, A., Plasmonic Light Trapping in Thin-Film Si Solar Cells. *Journal of Optics* **2012,** *14* (2), 024002.

(16) Paetzold, U. W.; Moulin, E.; Pieters, B. E.; Carius, R.; Rau, U., Design of Nanostructured Plasmonic Back Contacts for Thin-Film Silicon Solar Cells. *Opt. Express* **2011,** *19* (S6), A1219-A1230.

(17) Ferry, V. E.; Munday, J. N.; Atwater, H. A., Design Considerations for Plasmonic Photovoltaics. *Adv. Mater.* **2010,** *22* (43), 4794-4808.

(18) Atwater, H. A.; Polman, A., Plasmonics for Improved Photovoltaic Devices. *Nat Mater* **2010,** *9* (3), 205-213.

(19) Kim, J.; Choi, H.; Nahm, C.; Park, B., Surface-Plasmon Resonance for Photoluminescence and Solar-Cell Applications. *Electronic Materials Letters* **2012,** *8* (4), 351-364.

(20) Narasimhan Vijay, K.; Cui, Y., Nanostructures for Photon Management in Solar Cells. In *Nanophotonics*, 2013; Vol. 2, p 187.

(21) Lin, H., *et al.*, Rational Design of Inverted Nanopencil Arrays for Cost-Effective, Broadband, and Omnidirectional Light Harvesting. *ACS Nano* **2014**.

(22) Leung, S.-F., *et al.*, Roll-to-Roll Fabrication of Large Scale and Regular Arrays of Three-Dimensional Nanospikes for High Efficiency and Flexible Photovoltaics. *Sci. Rep.* **2014,** *4*.

(23) Lare van, M.; Lenzmann, F.; Polman, A., Dielectric Back Scattering Patterns for Light Trapping in Thin-Film Si Solar Cells. *Opt. Express* **2013,** *21* (18), 20738-20746.

(24) Brongersma, M. L.; Cui, Y.; Fan, S., Light Management for Photovoltaics Using High-Index Nanostructures. *Nat Mater* **2014,** *13* (5), 451-460.

(25) Huang, X.; Han, S.; Huang, W.; Liu, X., Enhancing Solar Cell Efficiency: The Search for Luminescent Materials as Spectral Converters. *Chem. Soc. Rev.* **2013,** *42* (1), 173-201.

(26) Richards, B. S., Enhancing the Performance of Silicon Solar Cells via the Application of Passive Luminescence Conversion Layers. *Sol. Energy Mater. Sol. Cells* **2006,** *90* (15), 2329-2337.

(27) Zhou, Z.; Wang, J.; Nan, F.; Bu, C.; Yu, Z.; Liu, W.; Guo, S.; Hu, H.; Zhao, X.-Z., Upconversion Induced Enhancement of Dye Sensitized Solar Cells Based on Core-Shell Structured β-$NaYF_4$:$Er^{3+}$, $Yb^{3+}$@$SiO_2$ Nanoparticles. *Nanoscale* **2014,** *6* (4), 2052-2055.

(28) Sark van, W.; de Wild, J.; Rath, J.; Meijerink, A.; Schropp, R. E., Upconversion in Solar Cells. *Nanoscale Research Letters* **2013,** *8* (1), 81.

(29) Shinji, H.; Takayuki, O., Plasmonics: Visit the Past to Know the Future. *J. Phys. D: Appl. Phys.* **2012,** *45* (43), 433001.

(30) Kamat, P. V., Meeting the Clean Energy Demand: Nanostructure Architectures for Solar Energy Conversion. *J. Phys. Chem. C* **2007,** *111* (7), 2834-2860.

(31) Wang, H.-P.; Lien, D.-H.; Tsai, M.-L.; Lin, C.-A.; Chang, H.-C.; Lai, K.-Y.; He, J.-H., Photon Management in Nanostructured Solar Cells. *Journal of Materials Chemistry C* **2014,** *2* (17), 3144-3171.

(32) Spinelli, P.; Ferry, V. E.; Groep van de, J.; Lare van, M.; Verschuuren, M. A.; Schropp, R. E. I.; Atwater, H. A.; Polman, A., Plasmonic Light Trapping in Thin-Film Si Solar Cells. *Journal of Optics* **2012,** *14* (2).

(33) Watanabe, K.; Menzel, D.; Nilius, N.; Freund, H. J., Photochemistry on Metal Nanoparticles. *Chem. Rev.* **2006,** *106* (10), 4301-4320.

(34) Warren, S. C.; Thimsen, E., Plasmonic Solar Water Splitting. *Energy Environ. Sci.* **2012,** *5* (1), 5133-5146.

(35) Taima, T.; Chikamatsu, M.; Yoshida, Y.; Saito, K.; Yase, K., Nanocrystalline Metal Electrodes for High-Efficiency Organic Solar Cells. *Appl. Phys. Lett.* **2004,** *85* (10), 1832-1834.

(36) Barnes, W. L.; Dereux, A.; Ebbesen, T. W., Surface Plasmon Subwavelength Optics. *Nature* **2003,** *424* (6950), 824-830.

(37) Kelly, K. L.; Coronado, E.; Zhao, L. L.; Schatz, G. C., The Optical Properties of Metal Nanoparticles: The Influence of Size, Shape, and Dielectric Environment. *J. Phys. Chem. B* **2002,** *107* (3), 668-677.

(38) Maxwell, J. C., A Dynamical Theory of the Electromagnetic Field. *Philos. Trans. R. Soc. London* **1865,** *155*, 459-512.

(39) Kerker, M., Chapter 3 - Scattering by a Sphere. In *The Scattering of Light and Other Electromagnetic Radiation*, Kerker, M., Ed. Academic Press: 1969; Vol. 16, pp 27-96.

(40) Mie, G., Beiträge Zur Optik Trüber Medien, Speziell Kolloidaler Metallösungen. *Annalen der Physik* **1908,** *330* (3), 377-445.

(41) Ruffato G., Zacco G. and Romanato F., Innovative Exploitation of Grating-Coupled Surface Plasmon Resonance for Sensing, Plasmonics-Principles and Applications, Dr. Ki Young Kim (Ed.), **2012,** ISBN: 978-953-51-0797-2, InTech, DOI: 10.5772/51044.

(42) Coe, J. V.; Heer, J. M.; Teeters-Kennedy, S.; Tian, H.; Rodriguez, K. R., Extraordinary Transmission of Metal Films with Arrays of Subwavelength Holes. *Annu. Rev. Phys. Chem.* **2008,** *59* (1), 179-202.

(43) Rivera, V. A. G.; Ferri, F. A.; Jr., E. M., Localized Surface Plasmon Resonances: Noble Metal Nanoparticle Interaction with Rare-Earth Ions. In *Plasmonics - Principles and Applications*, Kim, K. Y., Ed. InTech: 2012.

(44) Turkevich, J., Colloidal Gold. Part I Historical and Preparative Aspects, Morphology and Structure. *Gold bulletin* **1985,** *18* (3), 86-91.

(45) Fan, M.; Brolo, A. G., Silver Nanoparticles Self Assembly as SERS Substrates with near Single Molecule Detection Limit. *PCCP* **2009,** *11* (34), 7381-7389.

(46) Kimling, J.; Maier, M.; Okenve, B.; Kotaidis, V.; Ballot, H.; Plech, A., Turkevich Method for Gold Nanoparticle Synthesis Revisited. *J. Phys. Chem. B* **2006,** *110* (32), 15700-15707.

(47) Perrault, S. D.; Chan, W. C. W., Synthesis and Surface Modification of Highly Monodispersed, Spherical Gold Nanoparticles of 50−200 nm. *J. Am. Chem. Soc.* **2009,** *131* (47), 17042-17043.

(48) Li, J.; Wu, J.; Zhang, X.; Liu, Y.; Zhou, D.; Sun, H.; Zhang, H.; Yang, B., Controllable Synthesis of Stable Urchin-Like Gold Nanoparticles Using Hydroquinone to Tune the Reactivity of Gold Chloride. *J. Phys. Chem. C* **2011,** *115* (9), 3630-3637.

(49) Gonçalves, M. R.; Makaryan, T.; Enderle, F.; Wiedemann, S.; Plettl, A.; Marti, O.; Ziemann, P., Plasmonic Nanostructures Fabricated Using Nanosphere-Lithography,

Soft-Lithography and Plasma Etching. *Beilstein Journal of Nanotechnology* **2011,** *2*, 448-458.

(50) Li, X. H.; Li, P. C.; Hu, D. Z.; Schaadt, D. M.; Yu, E. T., Light Trapping in Thin-Film Solar Cells via Scattering by Nanostructured Antireflection Coatings. *J. Appl. Phys.* **2013,** *114* (4), 044310-7.

(51) Luhman, W. A.; Hoon Lee, S.; Johnson, T. W.; Holmes, R. J.; Oh, S.-H., Self-Assembled Plasmonic Electrodes for High-Performance Organic Photovoltaic Cells. *Appl. Phys. Lett.* **2011,** *99* (10), 103306.

(52) Gao, T.; Wang, B.; Ding, B.; Lee, J.-k.; Leu, P. W., Uniform and Ordered Copper Nanomeshes by Microsphere Lithography for Transparent Electrodes. *Nano Lett.* **2014**.

(53) Xu, H.; Lu, N.; Qi, D.; Gao, L.; Hao, J.; Wang, Y.; Chi, L., Broadband Antireflective Si Nanopillar Arrays Produced by Nanosphere Lithography. *Microelectron. Eng.* **2009,** *86* (4–6), 850-852.

(54) Brodoceanu, D.; Fang, C.; Voelcker, N. H.; Bauer, C. T.; Wonn, A.; Kroner, E.; Arzt, E.; Kraus, T., Fabrication of Metal Nanoparticle Arrays by Controlled Decomposition of Polymer Particles. *Nanotechnology* **2013,** *24* (8), 085304.

(55) Niesen, B.; Rand, B. P.; Van Dorpe, P.; Cheyns, D.; Tong, L.; Dmitriev, A.; Heremans, P., Plasmonic Efficiency Enhancement of High Performance Organic Solar Cells with a Nanostructured Rear Electrode. *Advanced Energy Materials* **2013,** *3* (2), 145-150.

(56) Goux, A.; Pauporte, T.; Chivot, J.; Lincot, D., Temperature Effects on Zno Electrodeposition. *Electrochim. Acta* **2005,** *50* (11), 2239-2248.

(57) Elias, J.; Tena-Zaera, R.; Levy-Clement, C., Electrochemical Deposition of Zno Nanowire Arrays with Tailored Dimensions. *J. Electroanal. Chem.* **2008,** *621* (2), 171-177.

(58) Tena-Zaera, R.; Elias, J.; Levy-Clement, C.; Bekeny, C.; Voss, T.; Mora-Sero, I.; Bisquert, J., Influence of the Potassium Chloride Concentration on the Physical Properties of Electrodeposited Zno Nanowire Arrays. *J. Phys. Chem. C* **2008,** *112* (42), 16318-16323.

(59) Peulon, S.; Lincot, D., Cathodic Electrodeposition from Aqueous Solution of Dense or Open-Structured Zinc Oxide Films. *Adv. Mater.* **1996,** *8* (2), 166-&.

(60) Matsui, S.; Ochiai, Y., Focused Ion Beam Applications to Solid State Devices. *Nanotechnology* **1996,** *7* (3), 247-258.

(61) Giannuzzi, L. A.; Stevie, F. A., A Review of Focused Ion Beam Milling Techniques for Tem Specimen Preparation. *Micron* **1999,** *30* (3), 197-204.

(62) Steve, R.; Robert, P., A Review of Focused Ion Beam Applications in Microsystem Technology. *Journal of Micromechanics and Microengineering* **2001,** *11* (4), 287.

(63) Zhang, J.; Su, X.; Shen, M.; Dai, Z.; Zhang, L.; He, X.; Cheng, W.; Cao, M.; Zou, G., Enlarging Photovoltaic Effect: Combination of Classic Photoelectric and Ferroelectric Photovoltaic Effects. *Sci. Rep.* **2013,** *3*.

(64) PV Markets Support Measures and Costs. In *Photovoltaic Solar Energy Generation*, Rhodes, W., *et al.*, Eds. Springer Berlin Heidelberg: 2005; Vol. 112, pp 163-185.

(65) Green, M. A., Third Generation Photovoltaics: Ultra-High Conversion Efficiency at Low Cost. *Progress in Photovoltaics: Research and Applications* **2001,** *9* (2), 123-135.

(66) N.R.E.L Certified Best Research-Cell Efficiencies (accessed Accessed 01/09/2014).

(67) Shockley, W.; Queisser, H. J., Detailed Balance Limit of Efficiency of P-N Junction Solar Cells. *J. Appl. Phys.* **1961,** *32* (3), 510-519.

(68) Strehlow, W. H.; Cook, E. L., Compilation of Energy Band Gaps in Elemental and Binary Compound Semiconductors and Insulators. *J. Phys. Chem. Ref. Data* **1973,** *2* (1), 163-200.

(69) Sze, S. M.; Ng, K. K., P-N Junctions. In *Physics of Semiconductor Devices*, John Wiley & Sons, Inc.: 2006; pp 77-133.

(70) Shah, A. V.; Schade, H.; Vanecek, M.; Meier, J.; Vallat-Sauvain, E.; Wyrsch, N.; Kroll, U.; Droz, C.; Bailat, J., Thin-Film Silicon Solar Cell Technology. *Progress in Photovoltaics: Research and Applications* **2004,** *12* (2-3), 113-142.

(71) Physics of Solar Cells. In *Photovoltaic Solar Energy Generation*, Rhodes, W., *et al.*, Eds. Springer Berlin Heidelberg: 2005; Vol. 112, pp 11-21.

(72) Honsberg, C.; Bowden, S. http://pveducation.org/ (accessed Accessed 01/09/2014).

(73) Ralf, B. W.; Johannes, Ü., 3D Photonic Crystals for Photon Management in Solar Cells. *Journal of Optics* **2012,** *14* (2), 024003.

(74) Vanecek, M.; Babchenko, O.; Purkrt, A.; Holovsky, J.; Neykova, N.; Poruba, A.; Remes, Z.; Meier, J.; Kroll, U., Nanostructured Three-Dimensional Thin Film Silicon Solar Cells with Very High Efficiency Potential. *Appl. Phys. Lett.* **2011,** *98* (16), 163503-163503-3.

(75) Wild de, J.; Meijerink, A.; Rath, J. K.; Sark van, W. G. J. H. M.; Schropp, R. E. I., Towards Upconversion for Amorphous Silicon Solar Cells. *Solar Energy Materials and Solar Cells* **2010,** *94* (11), 1919-1922.

(76) Fischer, S.; Goldschmidt, J. C.; Loper, P.; Bauer, G. H.; Bruggemann, R.; Kramer, K.; Biner, D.; Hermle, M.; Glunz, S. W., Enhancement of Silicon Solar Cell Efficiency by Upconversion: Optical and Electrical Characterization. *J. Appl. Phys.* **2010,** *108* (4), 044912.

(77) Cheng, Y. Y., *et al.*, Improving the Light-Harvesting of Amorphous Silicon Solar Cells with Photochemical Upconversion. *Energy & Environmental Science* **2012,** *5* (5), 6953-6959.

(78) Wang, N.; Zhu, Y.; Wei, W.; Chen, J.; Li, P.; Wen, Y., Conversion Efficiency Enhanced Photovoltaic Device with Nanohole Arrays in Antireflection Coating Layer. *Opt. Commun.* **2011,** *284* (19), 4773-4777.

(79) Johnson, N. J. J.; Sangeetha, N. M.; Boyer, J.-C.; Veggel van, F. C. J. M., Facile Ligand-Exchange with Polyvinylpyrrolidone and Subsequent Silica Coating of Hydrophobic Upconverting β-$NaYF_4$:$Yb^{3+}$/$Er^{3+}$ Nanoparticles. *Nanoscale* **2010,** *2* (5), 771-777.

(80) Schietinger, S.; Aichele, T.; Wang, H.-Q.; Nann, T.; Benson, O., Plasmon-Enhanced Upconversion in Single $NaYF_4$:$Yb^{3+}$/$Er^{3+}$ Codoped Nanocrystals. *Nano Lett.* **2009,** *10* (1), 134-138.

(81) Lu, D.; Cho, S. K.; Ahn, S.; Brun, L.; Summers, C. J.; Park, W., Plasmon Enhancement Mechanism for the Upconversion Processes in $NaYF_4$:$Yb^{3+}$,$Er^{3+}$ Nanoparticles: Maxwell Versus Förster. *ACS Nano* **2014,** *8* (8), 7780-7792.

# Chapter 3: Optimizing Plasmonic Silicon Photovoltaics with Ag and Au Nanoparticles Mixtures

*This chapter is a systematic investigation on how the two types of plasmonic NPs (Au and Ag) can be used to minimize a negative effect (decreasing EQE) previously observed from plasmonic NPs integrated in photovoltaics. This Chapter is published as: Wang, P. H.; Millard, M.; Brolo, A. G., Optimizing Plasmonic Silicon Photovoltaics with Ag and Au Nanoparticle Mixtures. J. Phys. Chem. C* ***2014,*** *118 (11), 5889-5895. Copyright: Reproduced with permission.*

*All the measurements presented here were obtained by myself. Morgan Millard, develop the surface chemistry protocol implemented in this project under my direct supervision.*

The effects of size and surface coverage of gold nanoparticles (Au NPs) on the performance of modified silicon photovoltaic (Si PV) devices were investigated. An increase in external quantum efficiency (EQE) above 600 nm (relative to the unmodified Si PV) was observed for PV devices modified with Au NPs with an average diameter greater than 80 nm, and the maximum in enhanced photocurrent red-shifted as the Au NP size increased. A decrease in EQE was observed for wavelengths shorter than 600 nm, leading to minimum overall advantage in terms of electrical power generated by white light illumination relative to the unmodified standard. However, this negative effect was successfully minimized by adding silver (Ag) NPs to the surface of the modified PV device. A maximum ~6% EQE enhancement was observed for PV devices modified with a mixture of metallic nanoparticles (Ag and Au) at the localized surface plasmon resonance (LSPR) wavelengths, and an overall increase in the white light power conversion efficiency of ~5% was obtained.

## 3.1 Introduction

Light trapping plays a very important role in the efficiency of power conversion in photovoltaic (PV) devices.[1] For instance, the surface of commercial bulk silicon solar cells is generally textured[2] and coated with antireflective films to improve light capturing.[3] Recently, surface plasmon resonance (SPR) has received a lot of attention as a new alternative approach to enhance light collection in PV devices.[4−6] It is known that the scattering from a subwavelength metallic particle placed at a silicon−air interface is preferentially directed toward the high dielectric material (Si).[7,8] This interesting optical phenomenon has been explored to enhance the photocurrent conversion efficiency of silicon PV devices by using Ag, Au, or Cu nanoparticles (NPs).[9−11] However, another consistent observation is that the presence of the NPs leads to a severe degradation in the PV performance in a wavelength range located at the blue side of the localized surface plasmon resonance (LSPR). This decrease in photocurrent has been assigned to light absorption by the particles due to the metallic interband transition.[12] Alternatively, the low efficiency has also been ascribed to destructive interferences between the incidence and the scattered light within a certain wavelength range shorter than the LSPR of the particular NPs.[5,11,13−15] Although large photocurrent enhancement (as large as ∼20-fold) has been reported in the literature around the LSPR for Si PVs modified with Cu, Ag, and Au NPs,[10,11,16] the negative effect observed at shorter wavelengths than the LSPR sometimes compensate those gains, and even a strong overall decrease in photocurrent generated under white light illumination has been reported.[15] Furthermore, both the surface coverage and size of the NPs also play a very important role in terms of enhanced light scattering and photocurrent generation in silicon-based PV devices. However, there are not many controlled experiments that clearly show the trend of the enhanced photocurrent dependence on the NP size. The goal of this work is to experimentally tackle the problem of suppressed photocurrent for wavelengths shorter than the LSPR in plasmonic Si PV devices. The suppression effect was minimized here by modifying the surface of the Si PV with a mixture of Ag and Au NPs, achieving optimized overall photocurrent increase in the PV absorption spectrum in the visible range. The size of the Ag and the Au NPs was well controlled by wet chemistry synthesis. The surface coverage of NPs was controlled by adjusting the concentration of NPs in the suspensions deposited

on a self-assembled monolayer of 3-aminopropyltrimethoxysilane (APTMS). The photocurrent conversion efficiency was compared to references on the same piece of the Si PV device. This experimental investigation provides then strong experimental support to surface plasmon enhanced light trapping in PVs, and the use of an optimized mixture of different types of metallic (Ag and Au) NPs solves a critical problem in the development of plasmonic Si PV devices.

### 3.2 Experimental section

**3.2.1 Materials.** All chemicals were purchased from Sigma Aldrich and used without further purification. Au and Ag NP colloidal suspensions were synthesized based on methods previously reported.[17−19] Basically, gold (III) chloride hydrate ($HAuCl_4 \cdot 3H_2O$, 99.999% purity) and sodium citrate dihydrate ($C_6H_5O_7Na_3 \cdot 2H_2O$, >99% purity), were used to synthesize Au NP seeds (∼15 nm). Then, the larger size (40, 80, and 135 nm) Au NPs were synthesized by mixing different amounts of 15 nm Au NP seeds (1.000, 0.480, and 0.050 mL, respectively) with 25 μL of 10 mM hydroquinone (benzene-1,4-diol, ≥99%) in 50 mL of deionized water under constant stirring for 1 h. Finally, the solutions were centrifuged to yield a final volume of 1 mL. Ag NPs were synthesized by a similar procedure but using $AgNO_3$, as reported previously.[19] Si PV devices (1 in. square) were constituted of approximately 200 ± 20 μm thick single crystalline c-Si, boron doped, with rear aluminum contacts and Al front finger contacts (sheet resistance was about 45−50Ω). The boron doping depth was ∼500 nm, and the Si PV devices were textured but had no front antireflection coating. The Si PV devices were provided by Yangzhou Huaer Solar-PV Technology Co., Ltd., China.

**3.2.2 Nanoparticle Immobilization on Si PV**. Ag and Au NPs were immobilized on Si PV surfaces using our previous metal NP immobilization method with a minor change.[10,19] The clean silicon PV device surface was first treated with 3-aminopropyltrimethoxysilane (APTMS, 97% purity) to provide the adequate (amino) functionality for metallic NP immobilization. Then, 7 μL of different NP colloids suspended in water were dropped between the metal fingers on the silicon surface, yielding a modified area of about 2 mm × 1.5 cm, as shown in Figure 3−1. The water did not spread out due to a slight hydrophobic surface (APTMS modified), and this

confinement between the two metal fingers produced a fixed modified width of ~2 mm (Figure 3−1). The water was allowed to slowly evaporate at room temperature. After that, the PV devices were rinsed with abundant deionized water and anhydrous ethanol and blow dried under nitrogen flow. The PV devices were then kept under 80 °C in an oven for 5 min to remove traces of washing solvent. Figure 3−1 shows one of the Si PV devices and illustrates the areas modified with metal NPs. In the case of Figure 3−1, the Si surface between metal fingers is modified with Au and Ag NPs of different sizes. Several reference lanes, indicated in Figure 3−1, were defined between two modified lanes. The photocurrent results from the NP-modified areas were always compared to the adjacent reference lane, to minimize device-to-device variations. Our experiments indicated that no significant spectral and electrical responses were observed from the different reference lanes on the same PV device. In addition to the devices modified with single types of nanoparticles, as shown in Figure 3−1, experiments were also realized on lanes modified with mixtures of Ag and Au NPs. In those cases, the Si PV surface was first modified with Ag NPs following the procedure described above. Then the Si PV devices were washed and cleaned, and the procedure was repeated for Au NPs. Notice that modifying the surface with Au NPs first and then adding the Ag NPs yields the same results within the experimental uncertainties.

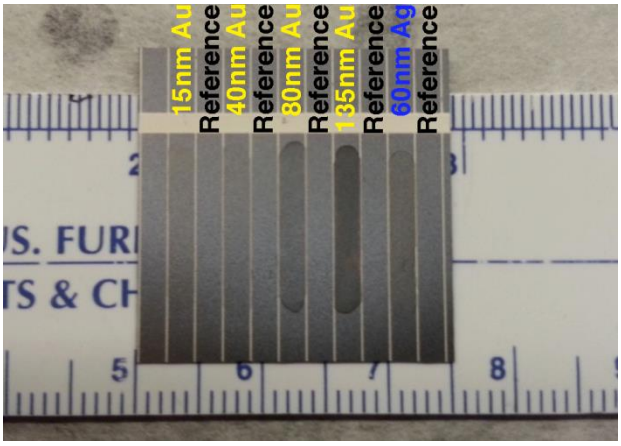


**Figure 3−1** Example of Au and Ag NPs modified Si photovoltaic device. The lanes were modified with 15, 40, 80, 135nm Au NPs and 60nm Ag NPs, respectively. The references were taken just beside each modified area, as indicated in the Figure.

### 3.3 Result and discussion

Figure 3−2 shows the normalized extinction spectra for each synthesized colloid dispersed in water. Ag NPs show a typical LSPR peak at about ~430 nm. The LSPR of Au NPs red shifted as the NP size increased from 15 to 135 nm. The red shift was accompanied by a broadening (increase in the fwhm), consistent with that expected for larger NPs. The inset in Figure 3−2 shows pictures of the NP colloidal suspensions. The typical characteristic colors observed in Figure 3−2 are correlated to the NP sizes and type (from left to right, 60 nm Ag NPs, 15, 40, 80, 135 nm Au NPs).

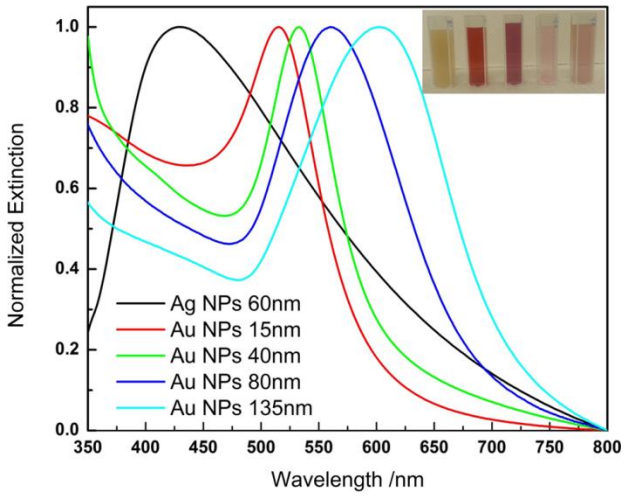


**Figure 3−2** Normalized extinction spectra of Ag (black curve) and Au NPs (sizes indicated in the Figure) dispersed in water. The LSPR peaks red-shifts as the size of the Au NPs increases. The picture in the inset shows the suspensions in glass cuvettes: 60nm Ag NPs, 15, 40, 80 and 135nm Au NPs, from left to right, respectively.

SEM images of five Si PV surfaces modified with different NPs are shown in Figure 3−3. Note that the Si PV surfaces were not smooth due to the standard industrial NaOH base cleaning process (texturing), but no noticeable spectral or external quantum efficiency (EQE) variations in different areas of a given Si PV device were observed. Figure 3−3 also shows no signs of large aggregations on the surface for all the immobilized NPs. The surface coverage is then considered uniform and random. The surface coverage of metallic NPs will affect the reflection and absorption properties of the modified PV devices.[10,20] The different surface coverages for Ag and Au NPs on the

PV surfaces were controlled by systematically diluting the concentrated stock of NP suspensions with deionized water, although the same volume (7 μL) of NP suspensions was applied on the APTMS-modified PV device surface every time, as described in the Experimental Section. The %EQE was measured for all NP-modified and reference Si PV devices under monochromatic light, with 10 nm steps (data available as Supporting Information (SI), Figure A−SI−1). Relative EQE variations (%ΔEQE(λ)), defined as in eq 1, are presented in Figure 3−4 for different wavelengths

$$\%\Delta EQE(\lambda) = \frac{EQE_{NPs}(\lambda) - EQE_{ref}(\lambda)}{EQE_{ref}(\lambda)} x100\% \quad (1)$$

where EQENPs(λ) and EQEref(λ) are the external quantum efficiencies measured from the NP-modified Si PV and the reference (on the same PV device, as shown in Figure 3−1), respectively. According to the definition in eq 1, when the %ΔEQE (λ) is positive, the presence of NPs improved the efficiency of the device, compared to the unmodified reference Si PV. The EQE is directly proportional to the photocurrent. Assuming that only electron−hole pairs generated by light absorption contribute to the photocurrent, the increase in EQE indicates that more photons have been absorbed by the Si PV device at certain wavelengths when the NPs were present. On the other hand, negative %ΔEQE(λ) values mean that less photons (than the reference) were absorbed by the Si PV device in the presence of the NPs. The general profiles of %ΔEQE(λ) for different Si PV coated with NPs are shown in Figure 3−4. These results agreed with our previous finding[10] and with findings from others in the literature.[11] The profiles (Figure 3−4) are clearly strongly dependent on the type and on the size of the metallic NPs coating the Si PV surface, as expected. The surface coverage (calculated from the SEM images) for the 60 nm Ag NPs was 7.1 ± 1.2 $\mu m^{-2}$ and for the 15, 40, 80, and 135 nm Au NPs was 298 ± 35, 39.8 ± 2.2, 5.4 ± 1.5, and 7.9 ± 3.1 $\mu m^{-2}$, respectively.

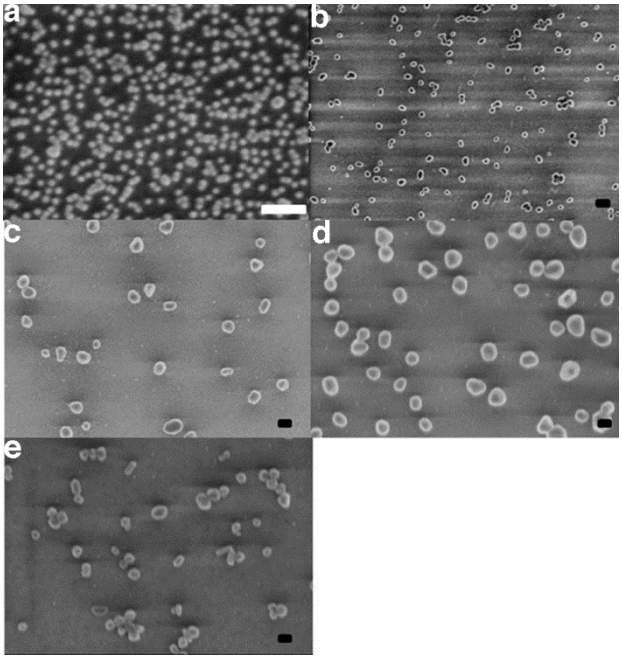


**Figure 3−3** SEM images of NPs of various average size immobilized on Si PV devices: (a) 15nm Au NPs; (b) 40 nm Au NPs; (c) 80 nm Au NPs; (d) 135nm Au NPs; (e) 60nm Ag NPs. Scale bars are 100nm.

The %ΔEQE(λ) curves in Figure 3−4 for Ag and large Au NPs (80 and 135 nm) present negative dips and positive maxima. The positions of the maxima can be correlated to the LSPR peaks of the colloids immobilized on APTMS-modified Si PV (reflectance curves from the modified Si PV surfaces are shown as SI (Figure A−SI−2). The reflectance curves for the larger Au NPs presented multiple peaks, as expected, due to the contributions from higher multipole modes[21] (Figure A−SI−2, SI). Figure 3−4 shows that the maximum in the %ΔEQE(λ) red shifts as the size of the Au NPs increased, following the expected trend of the LSPR. The characteristic %ΔEQE(λ) profile apparently matches closely the NP extinction spectrum (coincidence between the positive peak in the %ΔEQE(λ) and the LSPR extinction peak) when the surface coverage of the NPs attached to the surface increased (Figure 3−4, SI, Figure A−SI−2 and Figure A−SI−3). The positive %ΔEQE(λ) values in Figure 3−4 are mainly attributed to the preferential light scattering into the silicon mediated by the LSPR.[15,20] This effect becomes more apparent for larger particles, and it is dominant at longer wavelengths. Negative %ΔEQE (λ) is observed in Figure 3−4 for the entire wavelength range for small

NPs (diameters < 60 nm). In those cases, the presence of NPs is actually deleterious to the performance of the PV cell, yielding devices with lower power generation than the references in the whole spectral range. On the other hand, PVs coated with larger NPs (diameters > 60 nm) presented negative ΔEQE(λ) only at the blue-end of the profiles in Figure 3−4. The negative performance observed for larger NPs has been attributed to a combination of scattering and transmission effects that leads to a destructive interference of the light waves combined at the surface of the Si PV[15] and also due to the light absorption at the interband transition[10,12] (in the blue region relative to the LSPR). The positive %ΔEQE performance observed for larger NPs presents a broad profile that extends toward longer wavelengths (Figure 3−4). The broadening of the LSPR at longer wavelengths is attributed to NP−NP interactions. Although the SEM in Figure 3−3 does not point out large-scale aggregation, small clusters containing between two and five NPs were common, mainly for larger particle diameters. Those strong interacting clusters provided the main contributions to the scattering at longer wavelengths, leading to a relative "flat" %ΔEQE profile beyond ∼700 nm. The multipole contributions, clearly seen in the reflectivity data in Figure A−SI−2 (SI), are expected to appear blue shifted relative to the dipole peak from individual particles and from the interacting aggregates (clusters) discussed above. Although multipolar scattering (such as quadrupolar contributions) can be very efficient,[21] their effect at shorter wavelengths is offset by the mechanisms (interband transition, for instance) that lead to an overall negative ΔEQE.

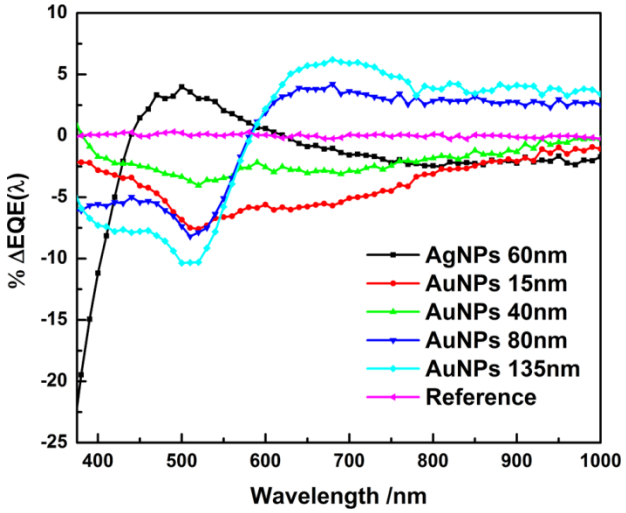


**Figure 3−4** %ΔEQE(λ) plots from Ag and Au NPs modified Si PV devices (the pink curve is a reference lane compared to another reference lane on the same Si PV device). Surface coverages (calculated from 3~4 random places in each SEM image): for 60nm Ag NPs = 7.1±1.2μm$^{-2}$; for 15 nm Au NPs = 298±35 μm$^{-2}$; for 40 nm Au NPs = 39.8±2.2 μm$^{-2}$, for 80 nm Au NPs = 5.4±1.5 μm$^{-2}$; and for 135nm Au NPs = 7.9±3.1 μm$^{-2}$.

In summary, Si PV modified with Au NPs that are less than 80 nm diameter experienced a decrease in %ΔEQE(λ) in the whole visible range. In these cases, the Au NP modified PV always generates less photocurrent than the reference device. However, for Ag and Au NPs with diameters larger than 60 nm, a decrease in %ΔEQE(λ) was observed only at the blue-end of the visible spectrum, followed by a positive %ΔEQE peak at a wavelength range that matches the LSPR of the NPs immobilized in Si PVs (Figure A−SI−3, SI).

The negative effect at shorter wavelengths can offset some of the gain in efficiency at longer wavelengths. Those types of situations are then not ideal since they can lead to either no overall gain or even negative performance of the Si PV (relative to the reference) under white light illumination. This effect is illustrated by the power curves obtained for the Si PV devices modified with either Au or Ag NPs, presented as Supporting Information (Figure A−SI−1c). The goal of this work is to minimize that negative %ΔEQE(λ) effect observed for larger NPs in Figure 3−4. A quick analysis of Figure 3−4 shows that the position of the negative %ΔEQE(λ) observed for Au NPs

overlaps with the positive %ΔEQE(λ) effect from Ag NPs. This indicates that it might then be possible to compensate for some of the negative %ΔEQE(λ) effect by combining both Au and Ag NPs on the Si surface. This approach should work, as long as one optimizes the Ag:Au NP ratio at the surface to guarantee that the negative effect of Au NPs on the %ΔEQE(λ) will be countered by the positive effect of the Ag NPs. Figure 3−5a shows a typical SEM image of a Ag:Au NPs mixture at a Si PV surface. Images such as Figure 3−5a were used to confirm and quantify the Ag:Au NP ratios on the Si PV surface. EDX elemental analysis mapping of the green square area in Figure 3−5a is presented in Figure 3−5b. The mapping shows that both Ag and Au NPs were successfully immobilized on top of the Si PV. The Ag:Au NP mixture balances some of the negative effect on the performance of a Si PV modified with just one type of NP. Figure 3−6a presents the %ΔEQE(λ) profile for Si PV devices modified with 60 nm Ag NPs, 135 nm Au NPs, and two mixtures of these particles at different ratios (1.8:1 (ratio a) and 2.7:1 (ratio b), calculated from the SEM images). The %ΔEQE(λ) trend for the Ag:Au mixtures is the sum of the contributions from the individual types of NPs (Ag and Au). An optimized condition was found where the negative %ΔEQE(λ) from Au NPs was totally suppressed by Ag NPs. Although that mixture still carries negative %ΔEQE for wavelengths shorter than 400 nm, this negative %ΔEQE response in the blue-wavelength range (<400) is not as significant since the regular performance of PV devices suffers in that range due to the typical high front surface recombination. The results from Figure 3−6a show that the LSPR conditions can be carefully tuned to achieve an optimized light trapping condition for applications in Si PV. Large nanoparticles (>80 nm) are preferable because their extinction is dominated by light scattering, which is required for that type of plasmonic application.[8,9,22]

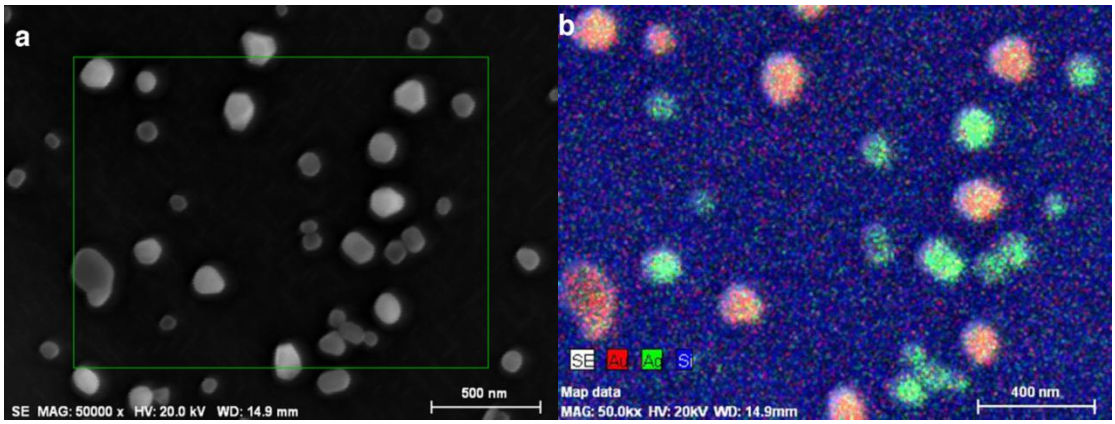


**Figure 3−5** (a) SEM image of Ag:Au NPs mixture adsorbed at a Si PV surface. (b) EDX elemental analysis mapping of the green square area in Figure 3−5a. Au NPs are red, Ag NPs are green, and Si surface is blue; scale bar are 500nm and 400nm for Figures 5a and 5b, respectively.

The role of the LSPR from Ag and Au NP mixtures on the enhanced power conversion mechanisms was confirmed by further reflectance measurements and numerical calculations. Figure 3−6b shows the measured extinction for a mixture of 60 nm Ag and 135 nm Au NPs on the Si PV device (obtained in reflection mode). The reflectance of Si PVs coated with either only Au or Ag NPs is also presented in Figure 3−6b. The extinction peaks on Si PV were, as expected, broader than for the NP suspensions in water (Figure 3−2). The extinction spectrum from the 60 nm Ag NPs (black curve in Figure 3−6b) presents a strong peak at ~500 nm, but it does not extend as much into the red as the spectrum of the 135 nm Au NPs (blue curve in Figure 3−6b). The overall extinction (red curve) of the Ag:Au NP mixture immobilized on the Si PV surface shows higher extinction in the blue wavelength range (<530 nm, due to the Ag NP contribution) than the 135 nm Au NPs alone. In addition, the position of the broad shoulder at ~650 nm, observed in the spectrum of the Ag:Au NP mixture, agrees with the LSPR enhanced photoconversion measured in Figure 3−6a

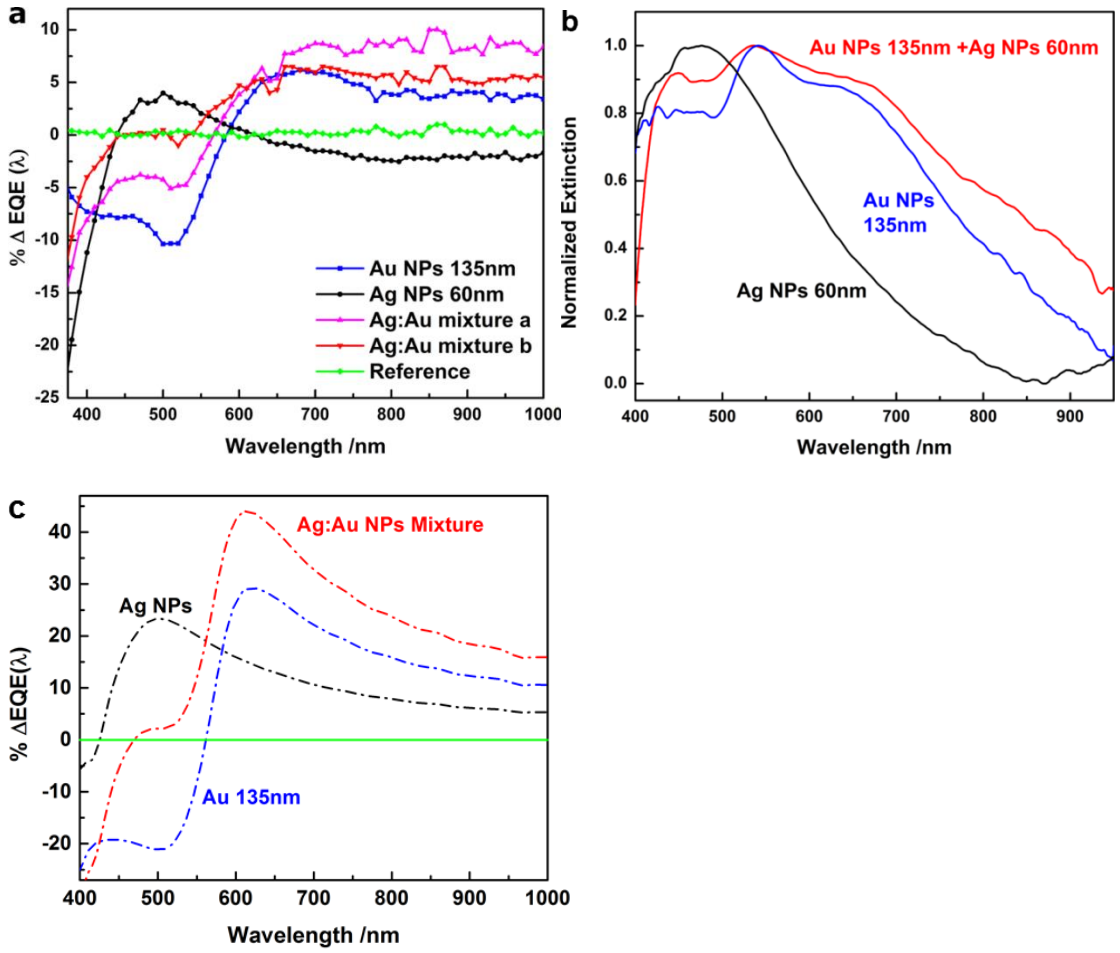


**Figure 3−6** (a) %ΔEQE plots for modified Si PV devices. The surface coverage of the NPs, obtained from SEM images at several random places, were: for 60nm diameter AgNPs = 7.1±1.2 $\mu m^{-2}$; 135 nm diameter Au NPs = 7.9±3.1 $\mu m^{-2}$; Ag:Au mixture a (Ag:Au ratio=1.8:1) = 8.7±2.3 $\mu m^{-2}$; and Ag:Au mixture b (Ag:Au ratio=2.7:1) = 6.4±3.0 $\mu m^{-2}$. Reference means a reference lane (without NPs) compared to another reference lane on the same device. The noise for the reference are due to measurements.(b) Normalized extinction (obtained by the reflection of white light from the modified Si surface (using the unmodified Si PV as reference) for Ag NPs (black), Au 135nm NPs (blue) and a mixture of Au 135nm and Ag 60nm NPs (red) immobilized on a Si PV device. (c) FDTD calculated %ΔEQE (λ) plots for Si PV devices modified with Ag NPs (black curve); Au NPs (blue curve) and Ag:Au NPs (red curve). The profile from the Si PV modified with Ag NPs was normalized by a factor of 0.5 and the calculations presented were also for 135nm diameter Ag NPs (rather than 60nm) to provide a better match with the experimental result.

The general characteristics of the profiles presented in Figure 3−6b were confirmed by numerical calculations. A finite-difference time-domain (FDTD) model, based on the approach demonstrated by Lim et al.,[11] was implemented. The calculated %ΔEQE (λ) for different sizes and types of NPs are shown as SI (Figure A−SI−4). Note that the calculated %ΔEQE (λ) enhancements are higher than the experimental results (Figure 3−4). This overestimation occurs because our model considers that all photons inside the Si PV are absorbed and converted to electron−hole pairs. Moreover, the collection efficiency of the electrons (holes) is also deemed to be 100%. Otherwise, the calculated profiles mimic the experimental results relatively well (Figure 3−4), and the small discrepancies can be attributed to defects in the Si PV, the influence of the textured surface, inhomogeneous NPs size distribution and aggregation. The NP absorption contribution to the negative effect in the %ΔEQE (at about 500 nm for 135 nm Au NPs) is clearly demonstrated in the inset of Figure A−SI−4 (SI). The enhanced light−electricity conversion (positive %ΔEQE) observed at longer wavelengths was confirmed by the calculations to originate mainly from the preferential forward radiative scattering by the metallic NPs. Figure 3−6c shows the FDTD calculated %ΔEQE plots for Si PV devices modified with only Ag NPs, only Au NPs, and a Au:Ag NP mixture. The model assumed no significant aggregation on the surface and that the Ag and Au NPs are distanced enough from each other to avoid significant particle-to-particle LSPR interference. In that case, the %ΔEQE profile is just a linear combination of the %ΔEQE curves from the Si PV modified with Ag NPs and the Si PVs modified with Au NPs. The calculated %ΔEQE(λ) for the Si PV Ag:Au NP mixture (red curve in Figure 3−6c) confirms that the negative %ΔEQE for wavelengths < 560 nm, observed from the devices modified with Ag NPs alone, is offset by the presence of Au NPs. This is exactly the effect observed experimentally in Figure 3−6a.

The overall power conversion efficiency (measured under white light) of the Si PV device modified with 135 nm Au NPs presented no noticeable enhancement (data presented in Figure A−SI−1c, SI), mainly because the positive effect of the NPs on the %ΔEQE(λ) (>560 nm) was counteracted by the negative values of %ΔEQE observed at the blue end (<560 nm). On the other hand, when the Si surface contained a mixture of 60

nm Ag and 135 nm Au NPs (Ag:Au NPs 2.7:1/ APTMS/$SiO_2$/Si PV), the photocurrent−voltage (I−V) curve of the Si PV device, under white light illumination, shows a significant increase in photocurrent density (20.9 mA/$cm^2$) compared to the reference device (19.8 mA/$cm^2$, the same piece of Si PV device but without NP modification, APTMS/ $SiO_2$/Si PV). These I−V curves are shown in Figure 3−7a. Figure 3−7b shows the white light power curves for the reference cell and for the Si PV modified with the optimized mixture of Ag:Au NPs. The generated power (Pmax) by the NP-modified device in Figure 3−7b shows about 5% increase compared to the reference; this value is comparable with previous reports.[11] The nature of the enhancement mechanism is well established in the literature[15,21,22] and was confirmed by the FDTD calculations presented in Figure 3−6c. The enhanced conversion is simply assigned to favorable light scattering toward the Si by large sized metallic nanoparticles. The presence of both Ag and Au NPs on the same PV device further enables the optimization of the LSPR conditions for enhanced photocurrent generation.

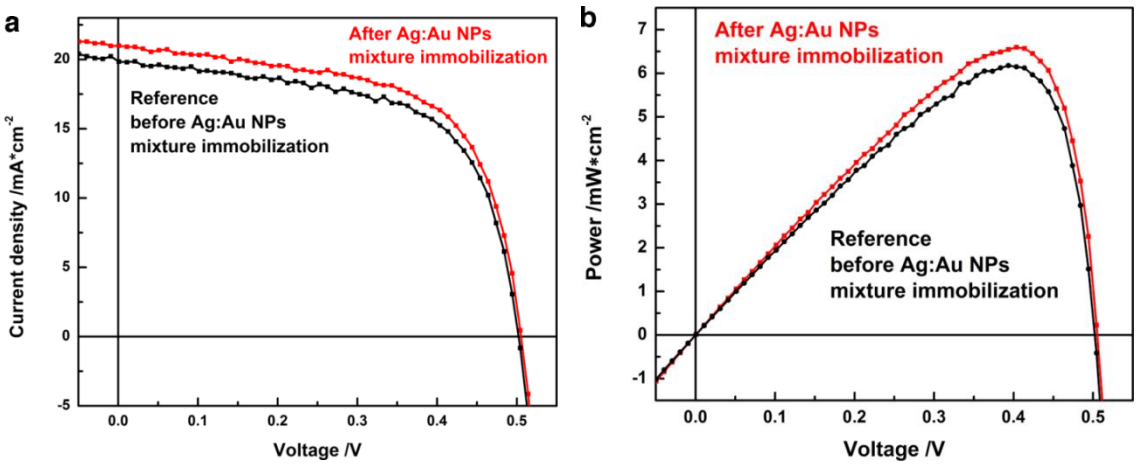


**Figure 3−7** (a) Si PV current-voltage (IV) curve under white light illumination (b) calculated power under white light illumination before and after Ag:Au NPs mixture immobilization, respectively.

### 3.4 Conclusions

We have successfully shown that mixed Ag and Au NPs can be immobilized on the top of Si PV devices to improve their overall efficiency. The surface coverage and size dependence of Au NPs on the EQE were studied systematically. %ΔEQE(λ)

enhancement was strongly dependent on the forward scattering efficiency, and these coincided with the LSPR. Au NPs larger than 80 nm led to increased %ΔEQE(λ) response above 600 nm. The highest %ΔEQE(λ) enhancement efficiency experimentally achieved at ~670 nm for Au NPs was ~6%. More importantly, we have experimentally shown the tunable %ΔEQE(λ) enhancement by utilizing two types of (Ag and Au) metallic NPs. The use of the Ag:Au NP mixture at the Si PV surface minimized the decreased efficiency observed from this type of PV, maximizing the device efficiency over a broader spectral range (425 nm to over 1000 nm). The overall power conversion efficiency, compared to the reference, increased by about 5%. A possible drawback of this approach, however, can be related to the higher reactivity of silver relative to gold. However, the chemical integrity of the NPs at the surface can be easily protected by the deposition of a thin dielectric layer, which is already part of the manufacturing procedure of Si based solar cells. The results presented here show that mixed metallic NPs can be explored as light capturing alternatives in commercial Si PVs.

**3.5 Reference**

(1) Mokkapati, S.; Catchpole, K. R., Nanophotonic Light Trapping in Solar Cells. *J. Appl. Phys.* **2012,** *112* (10), 101101.

(2) Campbell, P.; Green, M. A., Light Trapping Properties of Pyramidally Textured Surfaces. *J. Appl. Phys.* **1987,** *62* (1), 243-249.

(3) Bauer, G., Absolutwerte Der Optischen Absorptionskonstanten Von Alkalihalogenidkristallen Im Gebiet Ihrer Ultravioletten Eigenfrequenzen. *Annal. Phys.* **1934,** *411* (4), 434-464.

(4) Chen, X.; Jia, B.; Saha, J. K.; Cai, B.; Stokes, N.; Qiao, Q.; Wang, Y.; Shi, Z.; Gu, M., Broadband Enhancement in Thin-Film Amorphous Silicon Solar Cells Enabled by Nucleated Silver Nanoparticles. *Nano Lett.* **2012,** *12* (5), 2187-2192.

(5) Tan, H.; Santbergen, R.; Smets, A. H. M.; Zeman, M., Plasmonic Light Trapping in Thin-Film Silicon Solar Cells with Improved Self-Assembled Silver Nanoparticles. *Nano Lett.* **2012,** *12* (8), 4070-4076.

(6) Battaglia, C.; Hsu, C.-M.; Söderström, K.; Escarré, J.; Haug, F.-J.; Charrière, M.; Boccard, M.; Despeisse, M.; Alexander, D. T. L.; Cantoni, M.; Cui, Y.; Ballif, C., Light Trapping in Solar Cells: Can Periodic Beat Random? *ACS Nano* **2012,** *6* (3), 2790-2797.

(7) Atwater, H. A.; Polman, A., Plasmonics for Improved Photovoltaic Devices. *Nat Mater* **2010,** *9* (3), 205-213.

(8) Akimov, Y. A.; Koh, W. S., Design of Plasmonic Nanoparticles for Efficient Subwavelength Light Trapping in Thin-Film Solar Cells. *Plasmonics* **2011,** *6* (1), 155-161.

(9) Pors, A.; Uskov, A. V.; Willatzen, M.; Protsenko, I. E., Control of the Input Efficiency of Photons into Solar Cells with Plasmonic Nanoparticles. *Opt. Commun.* **2011,** *284* (8), 2226-2229.

(10) Souza de, M. L.; Corio, P.; Brolo, A. G., Cu Nanoparticles Enable Plasmonic-Improved Silicon Photovoltaic Devices. *Phys. Chem. Chem. Phys.* **2012,** *14* (45), 15722-15728.

(11) Lim, S. H.; Mar, W.; Matheu, P.; Derkacs, D.; Yu, E. T., Photocurrent Spectroscopy of Optical Absorption Enhancement in Silicon Photodiodes Via Scattering from Surface Plasmon Polaritons in Gold Nanoparticles. *J. Appl. Phys.* **2007,** *101* (10), 104309.

(12) Link, S.; El-Sayed, M. A., Shape and Size Dependence of Radiative, Non-Radiative and Photothermal Properties of Gold Nanocrystals. *Int. Rev. Phys. Chem.* **2000,** *19* (3), 409-453.

(13) Catchpole, K. R.; Polman, A., Plasmonic Solar Cells. *Opt. Express* **2008,** *16* (26), 21793-21800.

(14) Schaadt, D. M.; Feng, B.; Yu, E. T., Enhanced Semiconductor Optical Absorption Via Surface Plasmon Excitation in Metal Nanoparticles. *Appl. Phys. Lett.* **2005,** *86* (6), 063106.

(15) Spinelli, P.; Hebbink, M.; de Waele, R.; Black, L.; Lenzmann, F.; Polman, A., Optical Impedance Matching Using Coupled Plasmonic Nanoparticle Arrays. *Nano Lett.* **2011,** *11* (4), 1760-1765.

(16) Stuart, H. R.; Hall, D. G., Island Size Effects in Nanoparticle-Enhanced Photodetectors. *Appl. Phys. Lett.* **1998,** *73* (26), 3815-3817.

(17) Addison, C. J.; Brolo, A. G., Nanoparticle-Containing Structures as a Substrate for Surface-Enhanced Raman Scattering. *Langmuir* **2006,** *22* (21), 8696-8702.

(18) Perrault, S. D.; Chan, W. C. W., Synthesis and Surface Modification of Highly Monodispersed, Spherical Gold Nanoparticles of 50−200 Nm. *J. Am. Chem. Soc.* **2009,** *131* (47), 17042-17043.

(19) Fan, M.; Brolo, A. G., Silver Nanoparticles Self Assembly as Sers Substrates with near Single Molecule Detection Limit. *Phys. Chem.Chem. Phys.* **2009,** *11* (34), 7381-7389.

(20) Akimov, Y. A.; Koh, W. S.; Ostrikov, K., Enhancement of Optical Absorption in Thin-Film Solar Cells through the Excitation of Higher-Order Nanoparticle Plasmon Modes. *Opt. Express* **2009,** *17* (12), 10195-10205.

(21) Morawiec, S.; Mendes, M. J.; Mirabella, S.; Simone, F.; Priolo, F.; Crupi, I., Self-Assembled Silver Nanoparticles for Plasmon-Enhanced Solar Cell Back Reflectors: Correlation between Structural and Optical Properties. *Nanotechnology* **2013,** *24* (26), 265601.

(22) Ferry, V. E.; Munday, J. N.; Atwater, H. A., Design Considerations for Plasmonic Photovoltaics. *Adv. Mater.* **2010,** *22* (43), 4794-4808.

# Chapter 4: Enhanced Light Trapping in Three-Dimensional Nano-structured a-Si:H Solar Cells

*This chapter compares the effect of different types of metallic (Al, Ag, and Au) and nonmetallic ($SiO_2$) nanostructures on the efficiency of a-Si:H solar cells. A version of this chapter (only containing the data for Ag and $SiO_2$ nanoparticles) is published as: Theuring, M.; Wang, P. H.; Vehse, M.; Steenhoff, V.; von Maydell, K.; Agert, C.; Brolo, A. G., Comparison of Ag and $SiO_2$ Nanoparticles for Light Trapping Applications in Silicon Thin Film Solar Cells. J. Phys. Chem. lett.* ***2014****, 3302-3306. Copyright: Reproduced with permission.*

*The complete published paper is in Appendix B. The published comparison between Ag and $SiO_2$ nanoparticles for light trapping applications in a-Si:H thin film solar cells used the current state-of-art transparent conductive oxide (TCO) based on indium tin oxide (ITO). On the other hand, the data in this chapter was obtained using ZnO:Al. The conclusions obtained using ITO TCO were the same as the ones using ZnO:Al, which are presented in this chapter.*

*This was a collaboration project with Dr. Vehse at the University of Oldenburg in Germany. The intellectual conception of the project is from our group. I fabricated the nanostructured substrates. Martin Theuring and Volmer Steenhoff helped with the a-Si:H solar cells fabrication. Martin Theuring and I worked together on the measurements and simulations during this project.*

The integration of nano-structures, such as plasmonic and photonic architectures, in ultrathin film silicon solar cells enables better light trapping and management. A suite of plasmonic (Al, Au and Ag) and photonic nano-structures ($SiO_2$) were integrated in thin film (250 nm i-layer) hydrogenated amorphous silicon (a-Si:H) NIP solar cells through one simple “top-down” approach based on nano-sphere lithography (NSL). The integration of $SiO_2$ nano-particles (NPs) on the back of the a-Si:H NIP solar cell shows comparable performance than the plasmonic, the Asahi-U (surface textured) and

outperforms the flat reference solar cells in term of enhanced broad band light absorption. A maximum external quantum efficiency (%ΔEQE) enhancement of ~30% (compared to commercial textured reference) was achieved near 700 nm with the a-Si:H NIP solar cell modified with $SiO_2$ NPs arranged with a 700 nm periodicity. Numerical simulations were conducted to confirm the nature of the broad band enhancement observed experimentally. Potentially, the proposed NSL fabrication process could be an effective and inexpensive approach for the fabrication of large area surface textured three dimensional nano-structured solar cells. 10 x 10 $cm^2$ nano-structured a-Si:H NIP solar cells were fabricated and tested in this work.

## 4.1 Introduction

The production of an efficient and low cost device has been the ultimate goal in the thin film a-Si:H (hydrogenated amorphous silicon) NIP solar cell development. Nano-structured ultra-thin film solar cells have been attracting a lot of attention due to their ultimate light trapping characteristics and excellent charge separation.[1-4] In principle, either plasmonic[4-6] or photonic[7-9] nano-structures integrated in thin film solar cells have the potential to achieve higher efficiencies (than reference cells), mainly through enhanced light absorption and better light management[6]. Metallic nano-particles (NPs) have shown great promise as integrated materials in thin film solar cells that enhance both light absorption and scattering within the localized surface plasmon resonance (LSPR) region.[6,10] However, when integrated at the front end of the cell, the characteristic energy losses associated to metals limits the solar cell performance.[11, 12]On the other hand, plasmonic structures placed at the back of a thin film solar cell have demonstrated enhanced photo-conversion in the SPR region.[5, 13, 14] Increased efficiency has also been demonstrated for photonic nano-structured (organized arrays of dielectric nanoparticles) thin film solar cells. [2, 9, 15, 16]

Although several types of nano-structured thin film solar cells have demonstrated enhanced efficiency, the various common nano-patterning methods, such as e-beam lithography (EBL), focused ion beam (FIB), and nano-imprinting techniques,[17] can be costly and often limits the size of the nano-structured active area. Nano-sphere lithography (NSL) is a fabrication method that can provide large area nano-structure patterning at low-cost,[18,19] since it does not require chemical etching and other more complex fabrication steps.

This work presents a systematic investigation on the effect of identically shaped but different types of plasmonic (Al, Au and Ag) and photonic ($SiO_2$) nano-structures integrated in thin film (250 nm i-layer) hydrogenated amorphous silicon (a-Si:H) NIP solar cells. The nano-structured substrate was fabricated through a one simple "top-down" nano-sphere lithography (NSL) step, as shown in Figure 4−1. The a-Si:H NIP solar cells modified with $SiO_2$ NPs dielectric ($SiO_2$-NPs/a-Si:H) shows comparable performance to the plasmonic (Au, Ag, or Al-NPs/Si:H) NIP solar cell, yielding a maximum of ~30% external quantum efficiency (%ΔEQE) enhancement (relative to the

Asahi-U reference) near 700 nm for the 700 nm periodicity $SiO_2$ NPs array. The experimental results were confirmed by numerical simulations.

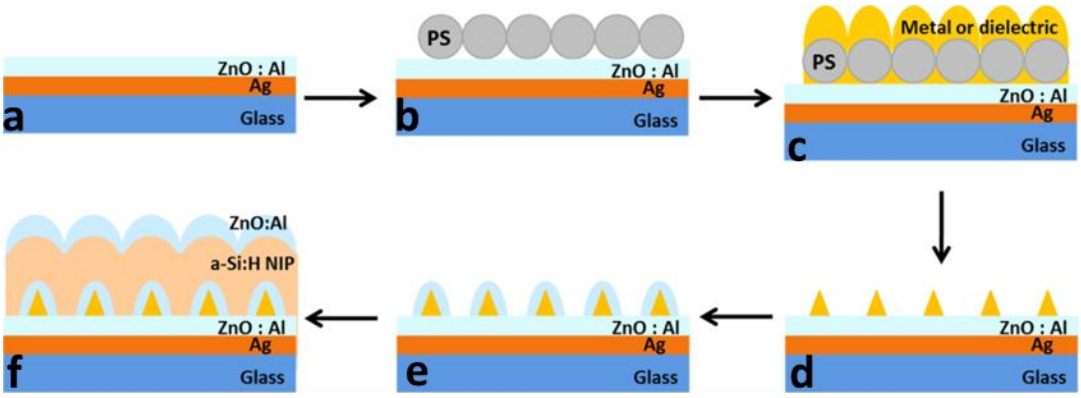


**Figure 4−1** Schematic representation of a periodic nanostructured a-Si:H NIP solar cell fabrication process (the method section contains additional details ). Basically, an self-assembled monolayer (SAM) of 700 nm polystyrene (PS) beads (b) was deposited on top a of ZnO:Al/Ag/glass substrate (a), followed by e-beam evaporation (c) of different materials (Au, Ag, Al and $SiO_2$), after the "lift-off" process (d), a hexagonal packed pyramid NPs were formed; then, the NPs were encapsulated in another buffer layer of ZnO:Al (e); finally, a thin-film a-Si:H NIP solar cell was fabricated by plasma-enhanced chemical vapor deposition (PECVD) process (f).

## 4.2 Experimental section

### 4.2.1 Fabrication of Periodic Nanostructure Substrate.

First, 120 nm Ag thin film was e-beam evaporated (30 nm Al as an adhesive layer) on a pre-cut 10 cm x 10 cm flat glass (Schott ECO32) substrate. 20 nm ZnO:Al was sputtered on top of the Ag thin film to protect Ag from oxidation (Figure 4−1a). Then, a monolayer of the 700 nm PS (721± 20nm, microParticles GmbH Berlin, 10 wt% aqueous dispersion) was deposited on top of the substrate (Figure 4−1b). To make the different type of NPs on the substrate (as in Figure 4−1d), 140nm of Au, Ag, Al and $SiO_2$ were e-beam evaporated on the PS covered substrates (Figure 4−1c), respectively; followed by a "lift-off" process in toluene, washed in ethanol with sonication and nitrogen blow dried. Lastly, another 60 nm ZnO:Al was sputtered on top of NPs serves as a diffusion barriers

and optical spacer (Figure 4−1e) between the metallic/dielectric NPs and a-Si:H layer during the growth of a-Si:H NIP at elevated temperature.

### 4.2.2 Fabrication of a-Si:H Solar Cell.

Subsequently, amorphous silicon solar cells were deposited by plasma-enhanced chemical vapor deposition (PECVD) in an industrial reactor (LEYBOLD OPTICS: Phoebus Lab Coater) with a parallel plate configuration at 200 $^{o}$C. All different type of nanostructured solar cells was fabricated in the same batch by PECVD to minimize the possible batch to batch variation. The cells are deposited in n-i-p configuration: First, a thin N-type silicon layer (10 nm) was deposited, followed by an intrinsic amorphous silicon layer (250 nm i-layer), and a thin P-type of silicon layer (20 nm) to make a NIP configuration. A front transparent conducive oxide (TOC) layer of 70 nm ZnO:Al was puttered by PECVD with a help of additional 10 nm Ag layer to improve the electrical conductivity (Figure 4−1f and Figure 4−2c).

### 4.2.3 Solar Cell Characterization.

The EQE was measured with a dual-lamp sun simulator (RiRa, SpeQuest) calibrated with a standard Si cell. The absorptions were measured with Cary 5000 UV-VIS-NIR spectrometer quipped with an integrating sphere on a large area ~1 cm$^2$ with 5nm step size. The current voltage (IV) characterizations of the a-Si:H solar cell were measured under illumination of a WACOM dual lamp solar simulator according to standard test conditions (AM1.5G spectrum, 1000W/m$^2$, 25 °C), illumination area were 0.25 cm$^2$. Note that 0.25 cm$^2$ illumination area was measured here even the solar cells were fabricated by 10cm x 10cm scale, in order to minimize the poor conductivity of the front ZnO:Al layer. Jsc was determined by convolution of EQE and the incoming photon flux of AM1.5G spectrum. Hitachi FB-2100 FIB was used to cut the cross section on a nano-structure a-Si:H NIP solar cell and Hitachi S4800 FESEM was used to characterize the a-Si:H NIP solar cells at 5KV using in-lens secondary electron backscattering detector.

### 4.2.4 Simulation for the different type NPs modified a-Si:H solar cell.

The EQE and absorption were calculated by Lumerical FDTD simulation. The simulation configuration and domain (orange box) shown in Figure 4−5a. It was designed according to the experiment setup using basic geometrical shapes. For the simulation, all the material dielectric property were obtained directly and available from the Lumerical data base, except, ZnO:Al layer was set with a refractive index n=2. For the EQE and the absorption profile calculation, only the absorption in the intrinsic layer (not in the doped layers) was taken into account, and the top 10 nm Ag layer was omitted in the simulation to further simplify the model. A plane wave excitation was used with a step size 5 nm and mess order 3 nm near the material interface. The simulated EQE was based on the absorption spectrum under the assumption that each photon absorbed generates one pair of electron and holes, and all the generated charges are collection.

## 4.3 Result and discussion

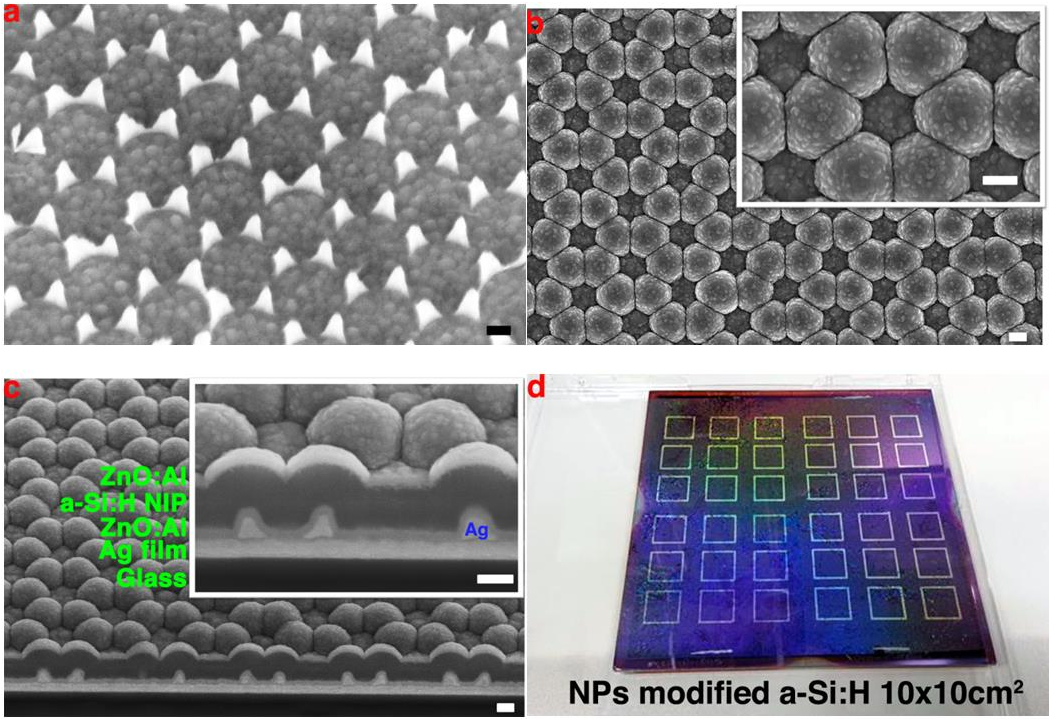


**Figure 4−2** (a) SEM of hexagonal packed Ag-NPs fabricated by NSL on top of a ZnO/Ag substrate imaged at 45 degrees tilt. (b) An top view of the surface of the final assembled a-Si:H NIP solar cell integrated with Ag nanostructures. (c) A cross section of a Ag-NPs modified a-Si:H NIP solar cell (Ag-NPs/Si:H). The cross section was milled by focused

ion beam (FIB) and imaged by SEM; viewed at 45 degrees titled angle; the cell stacks are indicated in the inserted SEM image. (d) An optical image of NPs modified a-Si:H NIP solar cells fabricated in a 10 cm x 10 cm scale with NSL. Scale bar in (a), (b) and (c) are all 200 nm.

Figure 4−2a presents a scanning electron micrograph (SEM) of a hexagonally packed Au-NPs structure fabricated on top of a ZnO/Ag substrate. The SEM imaged was obtained at a 45 degrees tilt. The Au-NPs fabricate by NSL were tri-facial pyramids with 150~200 nm base and 140 nm height (e-beam evaporated). The periodicity (distance between the structures) depended on the diameter of the polystyrene sphere used in the NSL template. Similar structures as in Figure 4−2a, with 700 nm periodicity, were also prepared using Ag, Al and $SiO_2$ NPs. A top view of a final assembled Ag-NPs/a-Si:H NIP solar cell (250nm i-layer) is presented in Figure 4−2b. The close packed hexagonal structure of the nanoparticles fabricated by NSL was nicely transferred to the top surface of the solar cell, despite some minor defects observed over the entire solar cell. The inset image in Figure 4−2b shows a closer view of the patterned structure.

Although this manuscript focus exclusively on a systematic study involving a-Si:H NIP solar cells fabricated with 700 nm periodicity, 250 nm i-layer, and hexagonal packed NPs, the features of the top structure of the a-Si:H NIP solar cell, such as periodicities and dome sizes, were easily controlled by tuning the different sizes, periodicities and geometry of the NPs deposited on the back of the substrate by NSL. Figure 4−2c presents a SEM cross section of a Ag-NPs/a-Si:H NIP cell milled using focused ion beam (FIB). The cross section image clearly confirms that each individual layer of the film (indicated in the inset of Figure 4−2c) was isotropically grown on top of the nano-structures. The images in Figure 4−2b-c indicate that texturing of both the front and the back surface of the a-Si:H NIP solar cell were easily achieved through the NPs modification. Figure 4−2d illustrates the potential of the technique for large area nano-fabrication. The picture in Figure 4−2d shows a NPs modified a-Si:H NIP solar cell fabricated in a 10 cm x 10 cm scale using NSL.

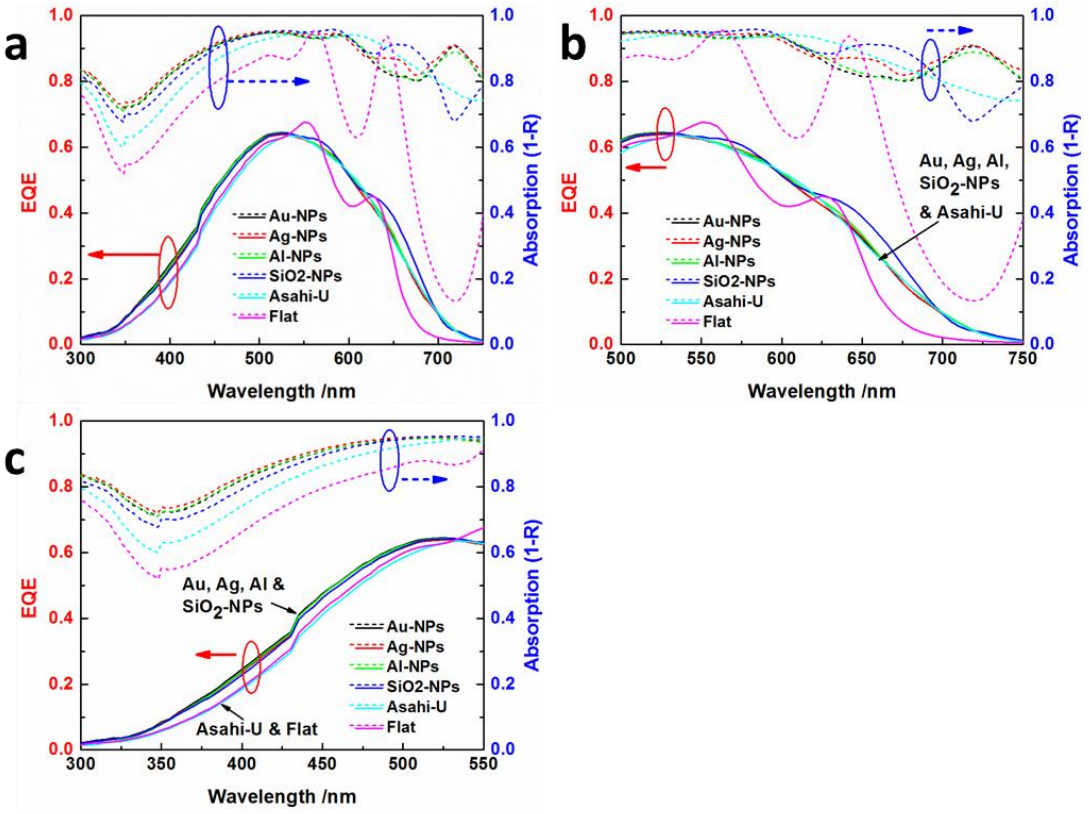


**Figure 4−3** (a) The external quantum efficiency (EQE, solid lines) and absorption (1-R, dashed lines) for a-Si:H NIP cells modified with different NPs materials (Au, Ag, Al, and $SiO_2$) at 700 nm periodicity compared to Asahi-U and flat references. (b, c) EQE and absorption (1-R) plots in red (500 nm and 750 nm) and blue (300 nm to 550 nm) spectrum region are from Figure a, respectively.

External quantum efficiency (EQE) and absorption (1-R) plots for a-Si:H NIP solar cells modified with different types of NPs (Au, Ag, Al, and $SiO_2$) are summarized in Figure 4−3a-c. The periodicity for all nanostructures was kept constant at 700 nm. It is important to note that all the NP-modified solar cells were fabricated under the exact same conditions and they were compared from the same batch. This minimizes cell-to-cell and batch-to-batch variations. The only difference between the NP-modified solar cells was the e-beam evaporation of different materials (Au, Ag, Al, and $SiO_2$), which required a change to an appropriate evaporation source. Figure 4−3a present the EQE and absorption result of NPs (Au, Ag, Al, and $SiO_2$) modified a-Si:H NIP cells compared to the industrial standard random pyramid textured Asahi-U and a flat a-Si:H NIP solar cell,

both of them used as references. As expected, texturing the back surface increases the total absorption in a broad range (relative to the flat surface), as seen in the Figure 4−3a. Figure 4−3b and Figure 4−3c are just zoomed versions of Figure 4−3a that highlight the spectra features in the red and blue spectral regions, respectively. In the red part of the spectrum, from 550 nm to 750 nm in Figure 4−3b, the absorption (1-R) responses were quite different for each solar cell modified with different types of materials and the references. The flat reference (magenta color, in Figure 4−3) shows a strong interference effect as peaks and valleys, due to the Fabry-Perot resonance within the thin film.[3, 8, 16, 19-21] The destructive interference (negative peaks) causes a decrease in the EQE (magenta color). Introduction of the surface random roughness (Asahi-U) and periodic (NPs modified) texturing on the back of the cell help to eliminate the interference effect, increasing the solar cell absorption in the red region. The EQE curves in Figure 4−3b show that the $SiO_2$-modified solar cell (blue color) are more efficient (evident by the "shoulder" in the blue EQE plot) in that spectral region when compared to the a-Si:H NIP modified with plasmonic NPs (Au, Ag and Al) and the Asahi-U reference. The "shoulder" in EQE measurements observed for the $SiO_2$-NPs/a-Si:H solar cells matched the increased absorption (1-R, blue dash) observed for the $SiO_2$ NPs modified solar cell in the same region (compared to the Asahi-U and the metallic NPs-modified solar cell – see Figure 4−3b, dashed lines, around 650 nm). The features of the absorption spectrum (1-R) were almost independent of the plasmonic material (Au, Ag and Al) up to 750 nm (Figure 4−3a) with the Fabry-Parot interference[3, 8, 16, 19-21] dominating the red part of the spectrum (550 nm to 750nm, Figure 4−3b). Overall, considering the absorption losses in metallic nanoparticles and material cost, both EQE and absorption results suggest that the $SiO_2$-based nanostructures were the best candidate for improved light trapping in a-Si:H NIP solar cells (Figure 4−3a and Figure 4−3b). Figure 4−3c shows a closer view of the solar cell absorption and performance parameters at the blue end of the spectrum, from 300nm to 550nm. In this case, all the NPs modified a-Si:H NIP solar cells showed enhanced EQE and absorption (1-R) compared to both the Asahi-U and the flat references. Blue light is expected to be preferentially absorbed at the front surface of the solar cell. The enhancement in the blue end can then be assigned mainly to the effect of the periodic front Si surface texturing[3] (Figure 4−2c). The periodic structure supports

Bloch photonic mode[3, 22, 23] that are known to facilitate light absorption. The nano-structured a-Si:H NIP solar cell has more materials per unit area compared to the flat reference a-Si:H NIP solar cell, this could also facilitate enhanced light absorption in the blue region. It is important to notice from Figure 4−3c that the metallic NPs-modified solar cell presented more absorption (1-R, dash lines) in the blue spectral region than the $SiO_2$ NPs-modified solar cell; however, this increased absorption was not translated into a larger EQE for the cells modified with metallic nano-structures. This indicates that the metallic NPs absorption increases the amount of light captured by the solar cell, but this enhanced absorption does not translate into increased efficiency due to the lossy nature of the metal.

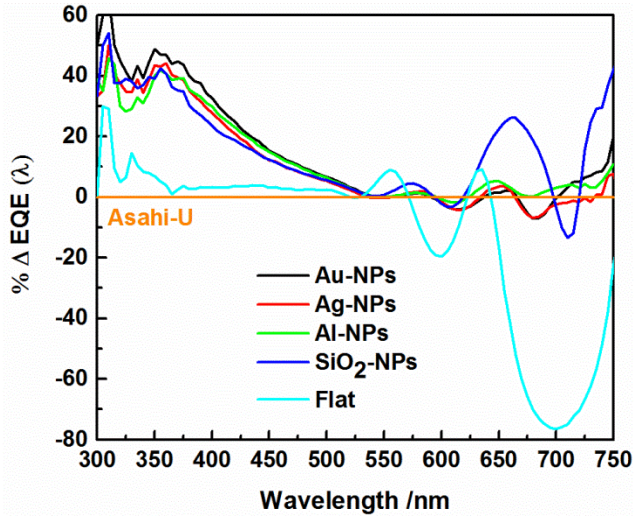


**Figure 4−4** % ΔEQE(λ) plot for NPs (Au, Ag, Al, and $SiO_2$) modified a-Si:H NIP solar cell and flat reference compared to Asahi-U reference, respectively.

The relative EQE variations (%ΔEQE), defined as in equation 4-1, were calculated and plotted in Figure 4−4 as a function of the wavelength.[11]

$$\% \, \Delta EQE(\lambda) = \frac{EQE_{NPs}(\lambda) - EQE_{Asahi-U}(\lambda)}{EQE_{Asahi-U}(\lambda)} \, x \, 100 \, \% \qquad (4\text{-}1)$$

where $\Delta EQE_{NPs}$ ($\lambda$) and $EQE_{Asahi\text{-}U}(\lambda)$ are the EQE measured from NPs modified and the commercial textured reference a-Si:H NIP solar cells, respectively. Figure 4−4 indicates that the NPs modified a-Si:H NIP solar cells outperform the Asahi-U and flat references in the blue end of the spectrum (between 300 nm and 500 nm) (positive %ΔEQE ($\lambda$) values) as discussed above. In the red end of the spectrum (between 500 nm and 750 nm), Figure 4−4 shows that the NPs-modified solar cells had comparable performance to the Asahi-U reference, although some positive peaks and negative valleys were clearly present in the %ΔEQE curve. Figure 4−4 also shows that the $SiO_2$-NPs/a-Si:H NIP solar cell presented a maximum ~30% ΔEQE enhancement near 700 nm compared to the commercial textured reference and slightly broader peak compared to the other type of solar cells.

The overall performance comparison between the different types of a-Si:H NIP solar cells investigated in this work is summarized in Table 4−1. Table 4−1 shows that the $SiO_2$-NPs/a-Si:H NIP solar cell presented ~4% smaller fill factor (FF≈63%) values than observed from the solar cells modified with metallic NPs and the two types of reference cells (FF≈67%). This effect arises from the non-conductive nature of the $SiO_2$ dielectric, which leads to an increase in back contact sheet resistant. The slight open circuit voltage (Voc) drop (~40mV) for all a-Si:H NIP solar cells modified with NPs relative to the references might be due to a thinner n- and p-doped layers formed on the sharp edges of the pyramidal NPs. On the other hand, the short circuit current density (Jsc) for the $SiO_2$-NPs/a-Si:H NIP solar cell (9.33mA/cm$^2$) shows comparable performance than the plasmonic solar cells (Au NPs: 9.10mA/cm$^2$; AgNPs: 9.02mA/cm$^2$ and Al NPs: 9.15mA/cm$^2$); and outperforms the Asahi-U (8.73mA/cm$^2$) solar cell and the flat reference (8.19mA/cm$^2$). This Jsc increase can be directly related to the improved light trapping in NPs modified a-Si:H NIP solar cells, as discussed above.

| a-Si:H solar cell | Jsc [mA/cm$^2$] | Voc [mV] | FF [%] | Efficiency [%] |
|---|---|---|---|---|
| Asahi-U | 8.73 | 886 | 66.9 | 5.17 |
| Flat | 8.19 | 881 | 67.4 | 4.87 |
| Au NPs | 9.10 | 849 | 67.1 | 5.19 |
| Ag NPs | 9.02 | 844 | 66.2 | 5.04 |
| Al NPs | 9.15 | 843 | 66.8 | 5.15 |
| $SiO_2$ NPs | 9.33 | 854 | 62.9 | 5.01 |

**Table 4−1** The overall performance comparison between the different types of a-Si:H NIP solar cells. Note that Jsc was determined by convolution of the EQE and the incoming photon flux of the AM1.5G spectrum. The IV characterizations were measured under the standard conditions.

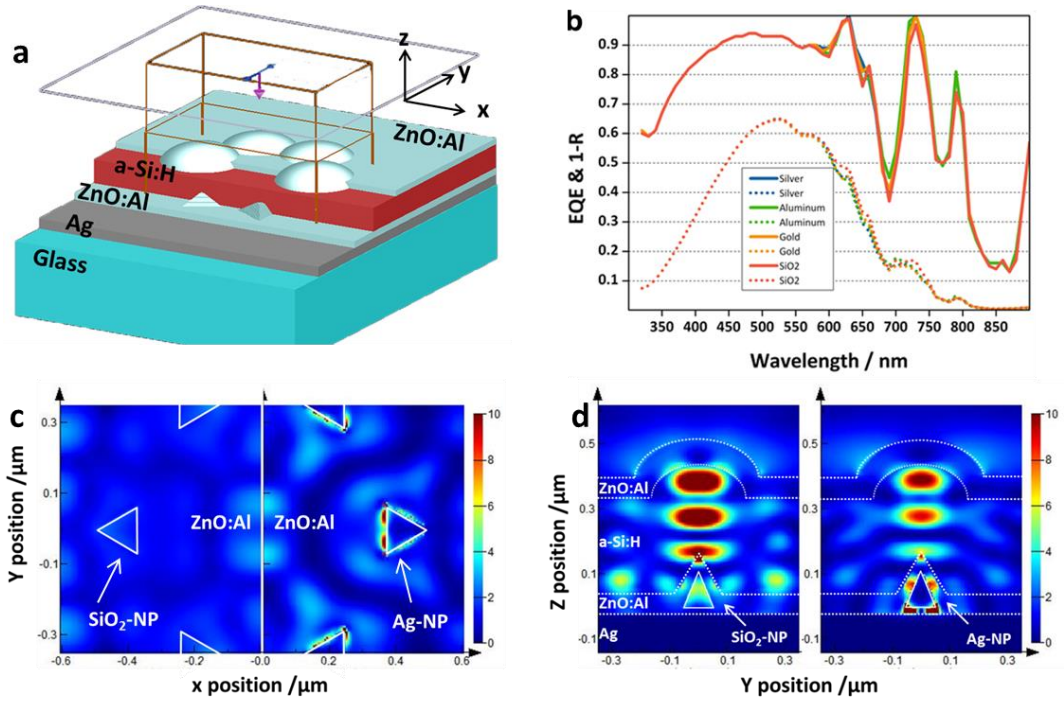


**Figure 4−5** Simulation comparison of different types of NPs materials modified a-Si:H NIP solar cell. (a) Schematic of a-Si:H NIP solar cell simulation configuration and domain (orange box). (b) Simulation results of EQE and absorption (1-R) for different types of NPs inside the a-Si:H NIP solar cell. (c) FDTD-calculated absorption for Ag and $SiO_2$ NPs modified substrates covered with ZnO:Al layer (n=2). (d) Calculated the electric field intensity (absorption) for Ag and $SiO_2$ NPs modified a-Si:H NIP solar cell in y-z direction at 662 nm excitation wavelength.

Figure 4−5 compares the calculated EQE and absorption for the four different type of NPs (Au, Ag, Al and $SiO_2$) modified a-Si:H NIP solar cells (see method section for the simulation details). Figure 4−5a presents a schematic of the a-Si:H NIP simulation configuration designed according to experimentally obtained SEM, presented in Figure 4−2c. Figure 4−5b shows the FDTD-calculated EQE and absorption (1-R) for a-Si:H NIP solar cells modified with the four different types of NPs (Au, Ag, Al, and $SiO_2$). The calculated EQE shows a similar EQE trend as the experimental result that presented in Figure 4−3a. The simulated EQE results didn't show much material dependence, as expected from the experimental results; however, the calculated EQE for the $SiO_2$

modified-solar cell also shown a small improvement after 600 nm as observed in the experimental result (Figure 4−3). In order to verify the small EQE enhancement in the red part (> 600 nm), the absorption for the metallic Ag NPs and dielectric $SiO_2$ NPs modified substrate were plotted in Figure 4−5c. As in the experiments, the presence of the Ag NPs always showed a higher absorption than the $SiO_2$ NPs modified substrate due the Ag NPs absorption. The calculated near electric field intensity at 662 nm in Figure 4−5d shows that the absorption was concentrated near the surface of Ag NPs, and that the Ag NPs absorb more than $SiO_2$ NPs. The absorption profiles inside silicon absorber layer resemble each other. It is important to realized that due to the 60 nm ZnO:Al buffer layer sputtered on top of the metallic/dielectric NPs, which served as both a diffusion barrier and an optical spacer between the metallic/dielectric NPs and a-Si:H layer, the enhanced field near the Ag NPs cannot contribute significantly to the electron-hole generation inside the a-Si:H layer, thus, this absorption represents a light loss. Therefore, both calculated (Figure 4−5b) and experimental EQE result (Figure 4−3) did not shown significant EQE enhancement near the red part of spectrum from the enhanced near field promoted by SPR.

### 4.4 Conclusion

In summary, we were able to show that similar light trapping properties are obtained with identically shaped nonmetallic NPs and metallic NPs features. As significant improvements were achieved with both NPs types over the textured and flat references, we conclude that the geometry of the structure has a much higher influence on the light trapping properties compared to its material for those types of cells. Specifically, the front side textures seem to have a major influence on the light distribution inside the cell. Finally, we deduce two major findings from our study: Firstly, one should aspire to use nonmetallic particles for a-Si:H cells because of the lower parasitic absorption associated with them. Secondly, but not of less importance, the influence of the light trapping structure on the electrical properties of the solar cell needs to be taken into account. In our example, the insulating nature of the $SiO_2$-NPs in the contact layer hinders an efficient charge extraction. Hence, shifting the SPR away from the absorber band gap or using non-metallic but conductive scattering features such as ZnO:Al (Chapter 5) or

indium tin oxide (ITO) nanostructures might be the best options to optimize the performance of thin film silicon solar cells.

**4.5 Reference**

(1) Seo, K.; Yu, Y. J.; Duane, P.; Zhu, W.; Park, H.; Wober, M.; Crozier, K. B. Si Microwire Solar Cells: Improved Efficiency with a Conformal Sio2 Layer. *ACS Nano* **2013,** *7*, 5539-5545.

(2) Kim, J.; Hong, A. J.; Nah, J.-W.; Shin, B.; Ross, F. M.; Sadana, D. K. Three-Dimensional a-Si:H Solar Cells on Glass Nanocone Arrays Patterned by Self-Assembled Sn Nanospheres. *ACS Nano* **2011,** *6*, 265-271.

(3) Ferry, V. E.; Polman, A.; Atwater, H. A. Modeling Light Trapping in Nanostructured Solar Cells. *ACS Nano* **2011,** *5*, 10055-10064.

(4) Nathan, C. L.; Prashant, N.; Kevin, M. M.; David, J. N.; Sang-Hyun, O. Engineering Metallic Nanostructures for Plasmonics and Nanophotonics. *Rep. Prog. Phys.* **2012,** *75*, 036501.

(5) Paetzold, U. W.; Moulin, E.; Pieters, B. E.; Carius, R.; Rau, U. Design of Nanostructured Plasmonic Back Contacts for Thin-Film Silicon Solar Cells. *Opt. Express* **2011,** *19*, A1219-A1230.

(6) Atwater, H. A.; Polman, A. Plasmonics for Improved Photovoltaic Devices. *Nat Mater* **2010,** *9*, 205-213.

(7) Mokkapati, S.; Catchpole, K. R. Nanophotonic Light Trapping in Solar Cells. *J. Appl. Phys.* **2012,** *112*, 101101.

(8) Ralf, B. W.; Johannes, Ü. 3d Photonic Crystals for Photon Management in Solar Cells. *Journal of Optics* **2012,** *14*, 024003.

(9) Lare van, M.; Lenzmann, F.; Polman, A. Dielectric Back Scattering Patterns for Light Trapping in Thin-Film Si Solar Cells. *Opt. Express* **2013,** *21*, 20738-20746.

(10) Morawiec, S.; Mendes, M. J.; Mirabella, S.; Simone, F.; Priolo, F.; Crupi, I. Self-Assembled Silver Nanoparticles for Plasmon-Enhanced Solar Cell Back Reflectors: Correlation between Structural and Optical Properties. *Nanotechnology* **2013,** *24*, 265601.

(11) Wang, P. H.; Millard, M.; Brolo, A. G. Optimizing Plasmonic Silicon Photovoltaics with Ag and Au Nanoparticles Mixtures. *J. of Phys.Chem.C* **2014**. *18*, 5889-5895.

(12) Lim, S. H.; Mar, W.; Matheu, P.; Derkacs, D.; Yu, E. T. Photocurrent Spectroscopy of Optical Absorption Enhancement in Silicon Photodiodes Via Scattering from Surface Plasmon Polaritons in Gold Nanoparticles. *J. Appl. Phys.* **2007,** *101*, 104309.

(13) Dai, W.; Yap, D.; Chen, G. Wideband Enhancement of Infrared Absorption in a Direct Band-Gap Semiconductor by Using Nonabsorptive Pyramids. *Opt. Express* **2012,** *20*, A519-A529.

(14) Ferry, V. E.; Munday, J. N.; Atwater, H. A. Design Considerations for Plasmonic Photovoltaics. *Adv. Mater.* **2010,** *22*, 4794-4808.

(15) Teck Kong, C.; Jonathan, W.; Sudha, M.; Kylie, R. C. Optimal Wavelength Scale Diffraction Gratings for Light Trapping in Solar Cells. *Journal of Optics* **2012,** *14*, 024012.

(16) Micco, A.; Ricciardi, A.; Pisco, M.; La Ferrara, V.; Mercaldo, L. V.; Veneri, P. D.; Cutolo, A.; Cusano, A. Light Trapping Efficiency of Periodic and Quasiperiodic Back-Reflectors for Thin Film Solar Cells: A Comparative Study. *J. Appl. Phys.* **2013,** *114*, 063103.

(17) Mohamed, M. H.; Shuqiang, Y.; Mike, M.; Frank, X.; Sanjay, B.; Sreenivasan, S. V. Enhanced Photocurrent in Thin-Film Amorphous Silicon Solar Cells Via Shape Controlled Three-Dimensional Nanostructures. *Nanotechnology* **2012,** *23*, 405203.

(18) Gonçalves, M. R.; Makaryan, T.; Enderle, F.; Wiedemann, S.; Plettl, A.; Marti, O.; Ziemann, P. Plasmonic Nanostructures Fabricated Using Nanosphere-Lithography, Soft-Lithography and Plasma Etching. *Beilstein Journal of Nanotechnology* **2011,** *2*, 448-458.

(19) Li, X. H.; Li, P. C.; Hu, D. Z.; Schaadt, D. M.; Yu, E. T. Light Trapping in Thin-Film Solar Cells Via Scattering by Nanostructured Antireflection Coatings. *J. Appl. Phys.* **2013,** *114*, 044310-044317.

(20) Park, H. J.; Xu, T.; Lee, J. Y.; Ledbetter, A.; Guo, L. J. Photonic Color Filters Integrated with Organic Solar Cells for Energy Harvesting. *ACS Nano* **2011,** *5*, 7055-7060.

(21) Naqavi, A.; Söderström, K.; Haug, F.-J.; Paeder, V.; Scharf, T.; Herzig, H. P.; Ballif, C. Understanding of Photocurrent Enhancement in Real Thin Film Solar Cells: Towards Optimal One-Dimensional Gratings. *Opt. Express* **2011,** *19*, 128-140.

(22) Ferry, V. E.; Verschuuren, M. A.; Lare, M. C. v.; Schropp, R. E. I.; Atwater, H. A.; Polman, A. Optimized Spatial Correlations for Broadband Light Trapping Nanopatterns in High Efficiency Ultrathin Film a-Si:H Solar Cells. *Nano Lett.* **2011,** *11*, 4239-4245.

(23) Deceglie, M. G.; Ferry, V. E.; Alivisatos, A. P.; Atwater, H. A. Design of Nanostructured Solar Cells Using Coupled Optical and Electrical Modeling. *Nano Lett.* **2012,** *12*, 2894-2900.

# Chapter 5: Cost-Effective Nanostructured Thin-Film Solar Cell with Enhanced Absorption

*This chapter presents a low-cost and scalable bottom-up approach to fabricate nanostructured thin-film solar cells with an electrodeposited honeycomb patterned zinc oxide electrode. This chapter is published as: Wang, P. H.; Nowak, R.-E.; Geißendörfer, S.; Vehse, M.; Reininghaus, N.; Sergeev, O.; von Maydell, K.; Brolo, A. G.; Agert, C., Cost-Effective Nanostructured Thin-Film Solar Cell with Enhanced Absorption. Appl. Phys. Lett. 2014, 105 (18), 183106. Copyright: Reproduced with permission*

*This work is also based on a collaboration with Dr. Martin Vehse's group in Germany. I proposed the intellectual conception using a combined process of nanosphere lithography and electrochemical deposition to pattern the ZnO transparent conductive electrodes. I prepared the nanostructured electrodes, characterized the solar cells performance, conducted FIB cut and characterized the solar cell with SEM. Regina Nowak did the ZnO electrochemical deposition, SEM characterization and measured the solar cell performance. Stefan Geißendörfer performed the numerical simulation and solar cell deposition. N. Reininghaus further optimized the solar cell deposition recipe.*

Nanostructured transparent conductive electrodes are highly interesting for efficient light management in thin-film solar cells, but they are often costly to manufacture and limited to small scales. This work reports on a low-cost and scalable bottom-up approach to fabricate nanostructured thin-film solar cells. A folded solar cell with increased optical absorber volume was deposited on honeycomb patterned zinc oxide nanostructures, fabricated in a combined process of nanosphere lithography and electrochemical deposition. The periodicity of the honeycomb pattern can be easily varied in the fabrication process, which allows structural optimization for different absorber materials. The implementation of this concept in amorphous silicon thin-film solar cells with only 100 nm absorber layer was demonstrated. The nanostructured solar cell showed approximately 10% increase in the short circuit current density compared to a cell on an

optimized commercial textured reference electrode. The concept presented here is highly promising for low-cost industrial fabrication of nanostructured thin-film solar cells, since no sophisticated layer stacks or expensive techniques are required.

## 5.1 Introduction

Thin-film solar cells are promising candidates for cost-effective electricity production in a future sustainable global energy system. A key topic in thin-film solar cell research is centered on efforts to further reduce their absorber layer thicknesses to save material and processing time[1,2] as well as to benefit from higher cell voltages.[3] Closely related to this is the development of efficient light management concepts to guarantee high absorption of the incoming light in the thin absorber layer.[4,5]

Well-known approaches to improve optical absorption in thin-film solar cells are quarter-wavelength antireflective coatings,[6-9] rough interfaces for an enhancement of the optical path length,[10-12] and scattering with metallic nanoparticles.[13-16] Beyond these concepts, further approaches using nanostructures, such as nanorods,[17-19] nanobeams,[20] spherical nanoshells,[21] and nanocones,[22-24] have been presented recently, many of them with remarkable potential for light trapping. Nevertheless, several of these structures require top-down lithography, advanced etching techniques or vacuum processes with high temperatures, which are costly and, in most cases, not suitable for mass production. However, as thin-film solar cells already have the constraint of lower efficiencies compared to conventional wafer-based solar cells, they will only be competitive in the long term if they are produced at drastically reduced costs. Therefore, instead of elaborate multilayer structures fabricated by sophisticated techniques, facile cell designs based on industrial fabrication processes are required.

## 5.2 Experiment and discussion

In this work, a concept to fabricate nanostructured thin-film solar cells with enhanced optical performance based on a low-cost two-step bottom-up process is presented. By combining nanosphere lithography and electrochemical deposition, transparent ZnO electrodes with honeycomb pattern of either nano- or micrometer dimensions were fabricated. These techniques are cost-effective bench-top methods that do not require process chambers, high temperatures, and they are applicable on industrial scale. The geometric aspects of the ZnO structure, such as size and periodicity, were easily controlled by the diameter of the nanospheres. The honeycomb structure induced a strong folding of the solar cell, leading to an enhanced optical absorption due to an increased

absorber volume and antireflection at the modified ZnO interface. The feasibility of this fabrication methodology was demonstrated for a hydrogenated amorphous silicon (a-Si:H) solar cell with only 100 nm absorber layer thickness. The concept proposed here is general and it can be applied for any thin-film solar cell material. The approach allows for simple optimization of desired structure sizes, and it is compatible with low-cost substrates, such as polymers and metal foils.

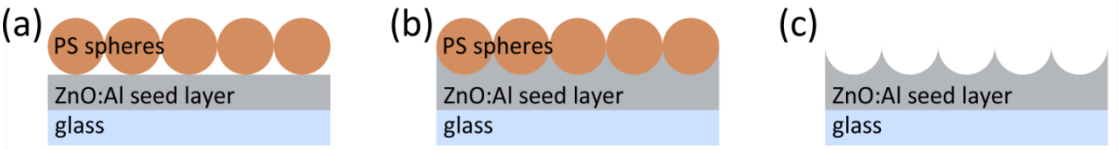


**Figure 5−1** Schematic of the ZnO honeycomb electrode fabrication process. (a) A seed layer of ZnO is covered with polystyrene (PS) spheres. The PS self-assembled monolayer on the surface generates a hexagonal two dimensional pattern. (b) ZnO is electrochemically deposited. The packed arrangement directs the ZnO deposition to the interstices between the PS spheres. (c) The PS spheres are removed, leaving a structured ZnO arrangement.

Figure 5−1 shows a schematic of the fabrication process of the honeycomb structures. First, a self-assembled monolayer of hexagonal close-packed polystyrene (PS) nanospheres (microParticles GmbH) was formed on top of a ZnO:Al seeded glass substrate via drop-coating (Figure 5−1a).[25,26] Then, the substrate, coated with the nanospheres, was used as working electrode for the electrochemical deposition of ZnO (Figure 5−1b). The self-assembled monolayer is not affected during the electrochemical growth of ZnO; this allows the combination of both, nanosphere lithography and electrochemical deposition.[27–30] An aqueous solution containing 0.5 mM $ZnCl_2$ and 0.1 M KCl was used as electrolyte. The solution was continuously saturated with oxygen during the process. The deposition was carried out in a three electrodes setup with an AglAgCl|Cl-(3M) reference and a Pt counter electrode at a constant temperature of 80°C. Further details about the electrochemical deposition process can be found elsewhere.[19,31–34] The PS spheres were removed by 5 min sonication in toluene after the ZnO growth

(Figure 5−1c). The honeycomb arrays presented a homogeneous coverage over the entire glass substrate (5 x 5 $cm^2$).

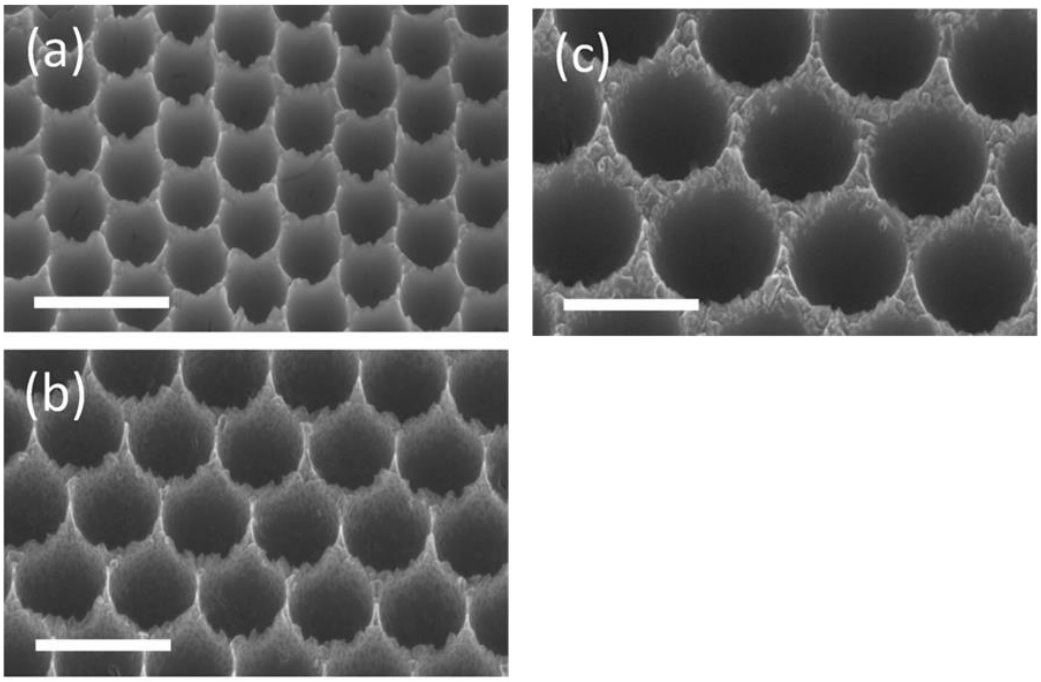


**Figure 5−2** Electrochemically deposited ZnO honeycomb arrays with periodicities of (a) 500 nm, (b) 700 nm and (c) 1 µm. Scale bar is 1 µm.

Figure 5−2 displays scanning electron microscope (SEM) images (under 45° tilt) of honeycomb arrays fabricated with three different PS sphere diameters of 500 nm, 700 nm and 1 µm. The images illustrate the control over the periodicity of the honeycomb array via the size of the PS spheres. Due to the continuous growth of ZnO in the interstices between the PS spheres, the surfaces inside the honeycomb holes are very smooth, as seen in Figure 5−2.

The effect of the ZnO honeycomb electrode on the performance of a thin-film solar cell was then tested. Thin a-Si:H p-i-n solar cells, with an intrinsic layer thickness of approximately 100nm, were fabricated onto 500 nm periodicity honeycomb arrays and on standard commercial wet-chemically etched (textured) ZnO:Al electrodes for comparison. A very thin layer of amorphous SiOx:H was used as p-doped layer. The n-doped layer consisted of nanocrystalline SiOx:H of approximately 60 nm thickness. Additionally, two $SiO_2$ buffer layers were inserted between the intrinsic and the doped

layers to limit doping cross contamination of the thin intrinsic layer.[35] The intrinsic and doped layers were fabricated by plasma enhanced chemical vapor deposition (PECVD) from a $SiH_4$:$H_2$ gas mixture at a temperature of 200 °C. $B_2H_6$ and $PH_3$ were added for p- and n-doping, respectively. The solar cells were terminated with electron beam evaporated Ag back contacts defining an active cell area of 1 $cm^2$. After fabrication, the cells were annealed for 30 min at 160 °C.

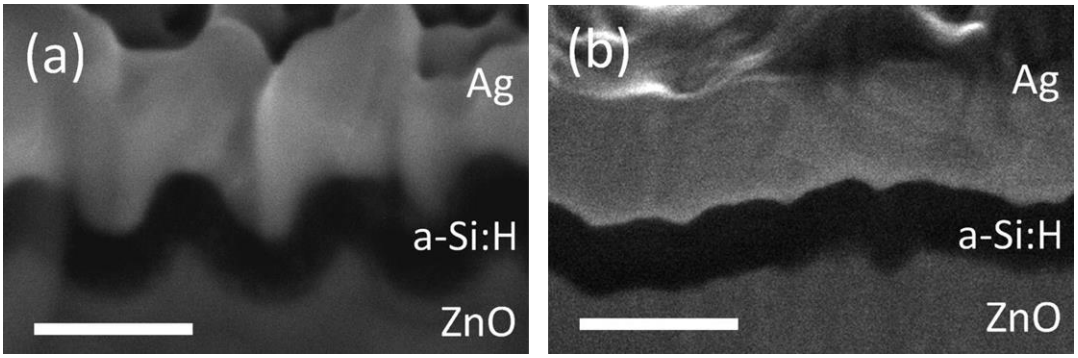


**Figure 5−3** SEM cross-sections of a-Si:H p-i-n solar cells on ZnO (a) honeycomb electrode and (b) textured reference. Scale bar is 500 nm.

Cross-sections of the cells, cut by focused ion beam and recorded by SEM, are displayed in Figure 5−3. For both cells, nanostructured (Figure 5−3a) and textured (Figure 5−3b), the cross-sections show the isotropic growth of a-Si:H from the PECVD process, which can be inferred from the constant absorber thickness along to the surface normal of the substrate. In case of the honeycomb cell, this leads to a pronounced folded cell, with increased optical absorber volume due to the larger surface area, still with constant thickness along the surface normal.

The advantages of a folded solar cell design, with “large optical” but “small electrical thickness”, have been pointed out recently by Vanecek et al, who realized this kind of structure with photolithography and reactive ion etching.[36] Experimentally, similar cell designs with silicon thin-film absorbers have been fabricated by patterning of a thermally grown $SiO_2$ layer with photolithography by Sai et al.,[37] and by a combined process of nanosphere lithography and reactive ion etching by Zhu et al.,[22] Hsu et al.,[23] and Battaglia et al.[38] While intrinsic absorber layer thicknesses of ≥ 250 nm were used in those studies, the advantages of the folded cell concept are especially relevant for thinner absorber

layers (≤ 100nm), as studied here. Another very important practical advantage, relative to previous reports, is that the nanostructures in this work were fabricated completely without the need of process chambers, but merely by solution-based bottom-up techniques.

The optical benefits of the honeycomb structure can be observed from the external quantum efficiency (EQE) and total cell absorption (reported as one minus reflection, 1-R, under the assumption that no light is transmitted through the cell stack), plotted in Figure 5−4. EQEs were calculated from differential spectral response measurements; the cell reflections were recorded in a photospectrometer with an integrating sphere. The EQE of the honeycomb cell is enhanced, relative to the textured reference, in nearly the entire spectral range (Figure 5−4). As discussed before, the larger surface area of the honeycomb electrode results in an increased absorber volume due to the isotropic growth of a-Si:H, although fabricated under equal conditions in the PECVD process as the textured reference. Only for shorter wavelengths (< 370 nm), the honeycomb cell showed increased parasitic absorption due to the additional amount of ZnO.

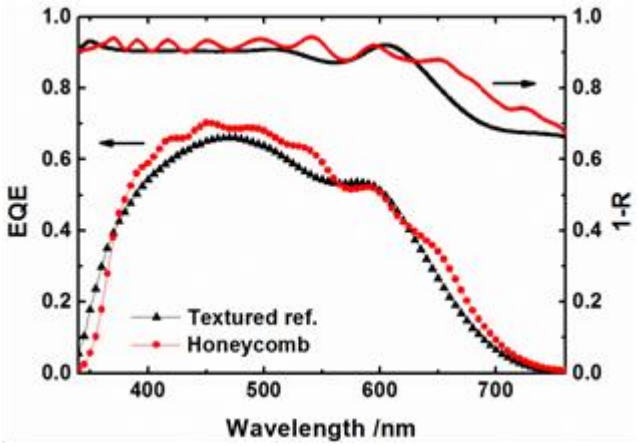


**Figure 5−4** EQE and total cell absorption (1-R) plots of a-Si:H p-i-n solar cells on honeycomb electrode (red) and a textured reference (black).

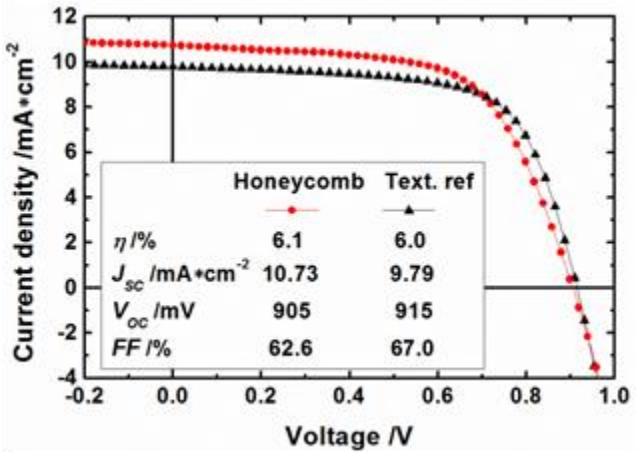


**Figure 5−5** Illuminated *JV*-curves of a-Si:H p-i-n solar cells on honeycomb electrode and textured reference. The characteristics of both cells are included as an inset.

Figure 5−5 displays the current density-voltage (JV)-curves for the folded honeycomb and the reference cell (statistical data are provided as in appendix C, Table C−1). The curves were recorded under illumination of a WACOM dual lamp solar simulator, according to standard test conditions (AM 1.5G spectrum, 1000 W/m$^2$, 25 °C). As expected from the EQE curves, the short circuit current density $J_{SC}$ of the honeycomb cell is larger (by 9.6%) compared to the textured reference cell (the characteristics of both cells are included as a Table embedded in Figure 5−5). The increase in $J_{SC}$ implies an overall enhanced efficiency; however, a slight deterioration in the electrical performance of the honeycomb cell is also evident in Figure 5−5.

The smaller open circuit voltage $V_{OC}$ measured from the honeycomb cell (relative to the reference) is not a fundamental limitation, in contrast to what is known from nanostructured ZnO electrodes with small structure sizes (< 400nm).[17,19,39] In the case of small structures, the loss in $V_{OC}$ is due to thickness variations in the a-Si:H layer, leading to a less homogeneous carrier distribution and thereby lower splitting of the quasi-Fermi levels.[39] For the honeycomb folded cell, which has a constant absorber thickness (as shown in Figure 5−3a), the loss in $V_{OC}$ is attributed to a slightly increased shunt resistance due to imperfections in the cell stack. With further optimization of the fabrication process, these $V_{OC}$ losses can be minimized, as it has been demonstrated already for reactive ion etched folded solar cells.[36,38]

The reduction in the fill factor FF for the honeycomb cell (inset in Figure 5−5) is induced by a series resistance related to a lower conductivity of the electrodeposited ZnO. Despite an intrinsic doping mechanism in the electrodeposition process,[32,40] the carrier density (5 x $10^{19}$ $cm^{-3}$, according to Tena-Zaera et al.[41]) is approximately one order of magnitude lower than in conventional sputtered ZnO:Al (6.3 x $10^{20}$ $cm^{-3}$). Earlier experiments, involving smaller electrodeposited ZnO nanostructures, showed no detrimental effects on the series resistance.[19] However, the conductivity in the electrodeposited ZnO is more important here for the honeycomb folded solar cell as the tips of the structure have to collect all charge carriers of the surrounding absorber material (this is a similar drawback due low conductivity material used as discussed in chapter 4 for $SO_2$ NP-modified solar cell). However, the optimization of the ion concentrations in the electrodeposition process,[41] as well as the addition of precursors for extrinsic doping to the growth solution,[42] promise further improvement of the carrier concentration of the electrodeposited ZnO. Therefore, by considering these options to further electrically optimize the structure, it is possible to affirm that honeycomb folded solar cells without losses in the electrical performance and the full benefits from the strongly enhanced optical properties are feasible.

With the commercial software Sentaurus TCAD, 3D optical and electrical simulations were performed to quantify the effect of an increased absorber volume and to study photon absorption in the folded honeycomb cell. Based on the results, the effect of different honeycomb periodicities on $J_{SC}$ is discussed, referring to the trade-off between increased absorber volume and higher parasitic absorption in the electrochemically deposited ZnO. Cells with 500 nm, 750 nm and 1µm honeycomb periodicity were simulated, similar to the series shown in Figure 5−2. The cell stack consisted of glass, flat ZnO:Al, electrochemically deposited ZnO (ECD-ZnO) with honeycomb pattern, an a-Si:H p-i-n structure with 100 nm i-layer thickness, and an Ag back contact. The a-Si:H p-i-n structure was modeled with the isotropic growth algorithm to obtain cells with constant absorber thickness along the surface normal as illustrated in Figure 5−2a. Details about the isotropic growth and electrical and optical input parameters for the simulations can be found in a previous study by Geißendörfer et al.[39]

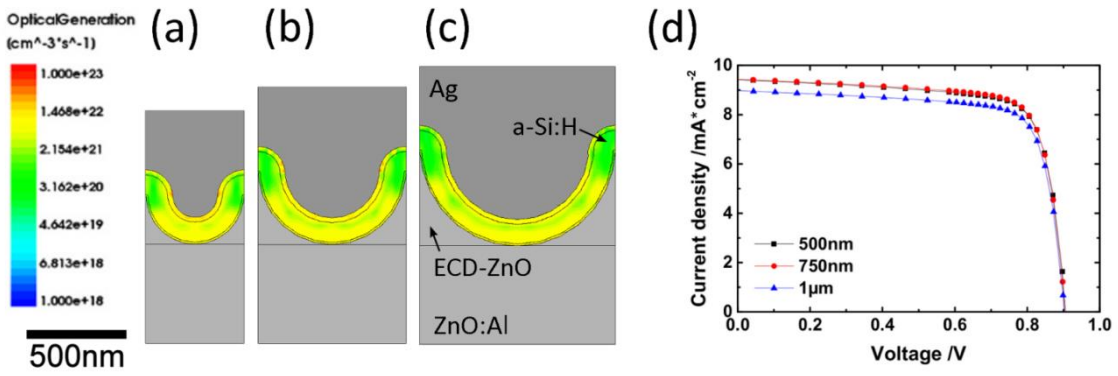


**Figure 5−6** Profiles of the optical generation rate of simulated honeycomb cells with periodicities of (a) 500 nm, (b) 750 nm, (c) 1 µm and (d) simulated *JV*-curves of the cells with different periodicities

Plots of the optical generation rate $G_{opt}(\lambda)$, calculated by finite difference time domain method (FDTD), are shown in Figure 5−6 a-c; Figure 5−6d displays the JV-curves of the structures which will be discussed below. The JSC values of the simulated cells are smaller compared to the experimental data shown in Figure 5−5, as optimized oxidic p- and n-a-Si:H layers were used in the experimental cell.

Due to the small cell thickness, the profiles of the optical generation rate Figure 5−6a-c mainly show homogeneous absorption with small influence of thin-film interference. On the tips of the honeycomb structure, the optical generation rate is reduced as part of the light is lost by absorption in underlying a Si:H material and in the subjacent electrochemically deposited ZnO. However, for all periodicities, the optical generation profiles look similar, and no distinct scattering features are observed for these thin a-Si:H cells, as it has been reported for other nanostructured cells with larger cell thickness.[43]

Table 5−1 shows the increase of the absorber volume for the simulated structures illustrated in Figure 5-6 (a)-(c), related to a flat structure with equal cell configuration. All structures have a strongly enhanced absorber volume >70%, and the absorber volume increases for larger honeycomb periodicity, because the folding of the cell becomes more pronounced. However, this leads not necessarily to an enhancement in $J_{SC}$ as it can be observed in the simulated JV-curves of the cells plotted in Figure 5−6d; the corresponding $J_{SC}$ values are listed in Table 5−1. In fact, parasitic absorption is enhanced for larger periodicities, as the amount of electrochemically deposited ZnO is increased

which is necessary to generate the honeycomb pattern. This is illustrated in the schematic cross-sections in Figure 5−6a-c, as for larger honeycomb periodicity, the structure has at the same time a larger depth and therefore a larger overall volume.

The $J_{SC}$ values in Table 5−1 underline this trade-off between increased absorber volume and parasitic absorption; $J_{SC}$ first slightly increases from 500 nm to 750 nm periodicity, but the increase in the absorber volume of only 4% from 750 nm to 1 μm periodicity is fully compensated by parasitic absorption loss in the electrochemically deposited ZnO, and thereby $J_{SC}$ is significantly reduced. The effect of parasitic absorption in the electrochemically deposited ZnO was already evident in Figure 5−4, where the honeycomb cell had a lower EQE in the wavelength region of ZnO absorption (<370nm) compared to the reference cell.

| Honeycomb periodicity /nm | Increased absorber volume /% | $J_{SC}$ /mA•cm$^{-2}$ |
|---|---|---|
| 500 | 71.4 | 9.41 |
| 750 | 77.6 | 9.43 |
| 1000 | 81.0 | 8.97 |

**Table 5−1** Increased optical absorber volume for folded honeycomb cells.

## 5.3 Conclusion

In conclusion, a low-cost and scalable bottom-up approach to fabricate nanostructured ZnO electrodes for enhanced optical absorption in thin-film solar cells was presented. The concept is based on the growth of honeycomb patterned ZnO structures by electrochemical deposition, preceded by a nanosphere lithography step. This approach induces a folding of the solar cell around the ZnO structure, resulting in strongly enhanced optical properties due to an overall increased absorber volume. Thin a-Si:H solar cells, with an intrinsic absorber layer thickness of 100 nm, were used as proof of concept, and a significantly enhanced EQE was observed. The short circuit current density was almost 10% higher compared to a solar cell on an optimized commercial textured ZnO reference electrode.

The process suggested here is compatible with low-cost substrates, such as polymers and metal foils, and allows an optimization of the structure for any desired cell concept. The periodicity can be easily controlled by the nanosphere size. No sophisticated layer stacks or expensive techniques are required, and therefore, the concept is highly promising for a low-cost industrial fabrication of nanostructured thin-film solar cells.

## 5.4 Reference


(1) S. Hegedus, *Prog. Photovolt: Res. Appl.* **2006**, *14*, 393.

(2) V. Krishnakumar, A. Barati, H.-J. Schimper, A. Klein, W. Jaegermann, *Thin Solid Films* **2013**, *535*, 233.

(3) P. Würfel, *Physics of Solar Cells*, WILEY-VCH, Weinheim, **2009**.

(4) H. A. Atwater, A. Polman, *Nat. Mater.* **2010**, *9*, 205.

(5) S. Mokkapati, K. R. Catchpole, *J. Appl. Phys.* **2012**, *112*, 101101.

(6) P. Jackson, D. Hariskos, E. Lotter, S. Paetel, R. Wuerz, R. Menner, W. Wischmann, M. Powalla, *Prog. Photovolt: Res. Appl.* **2011**, *19*, 894.

(7) I. Repins, M. A. Contreras, B. Egaas, C. DeHart, J. Scharf, C. L. Perkins, B. To, R. Noufi, *Prog. Photovolt: Res. Appl.* **2008**, *16*, 235.

(8) S. Bag, O. Gunawan, T. Gokmen, Y. Zhu, T. K. Todorov, D. B. Mitzi, *Energy Environ. Sci.* **2012**, *5*, 7060.

(9) L. Kranz, C. Gretener, J. Perrenoud, R. Schmitt, F. Pianezzi, F. La Mattina, P. Blösch, E. Cheah, A. Chirilă, C. M. Fella, H. Hagendorfer, T. Jäger, S. Nishiwaki, A. R. Uhl, S. Buecheler, A. N. Tiwari, *Nat. Commun.* **2013**, *4*, 2306.

(10) S. Fay, L. Feitknecht, R. Schlüchter, U. Kroll, E. Vallat-Sauvain, A. Shah, *Sol. Energy Mater. Sol. Cells* **2006**, *90*, 2960.

(11) M. Berginski, J. Hüpkes, M. Schulte, G. Schöpe, H. Stiebig, B. Rech, M. Wuttig, *J. Appl. Phys.* **2007**, *101*, 74903.

(12) J. Escarré, K. Söderström, M. Despeisse, S. Nicolay, C. Battaglia, G. Bugnon, L. Ding, F. Meillaud, F.-J. Haug, C. Ballif, *Sol. Energy Mater. Sol. Cells* **2012**, *98*, 185.

(13) K. R. Catchpole, A. Polman, *Opt. Express* **2008**, *16*, 21793.

(14) P. Spinelli, V. E. Ferry, J. van de Groep, M. van Lare, M. A. Verschuuren, R. E. I. Schropp, H. A. Atwater, A. Polman, *J. Opt.* **2012**, *14*, 24002.

(15) H. Tan, R. Santbergen, A. H. M. Smets, M. Zeman, *Nano Lett.* **2012**, *12*, 4070.

(16) V. E. Ferry, M. A. Verschuuren, M. C. Van Lare, R. E. I. Schropp, H. A. Atwater, A. Polman, *Nano Lett.* **2011**, *11*, 4239.

(17) Y. Kuang, K. H. M. van der Werf, Z. S. Houweling, R. E. I. Schropp, *Appl. Phys. Lett.* **2011**, *98*, 113111.

(18) L. Aé, D. Kieven, J. Chen, R. Klenk, T. Rissom, Y. Tang, M. C. Lux-Steiner, *Prog. Photovolt: Res. Appl.* **2010**, *18*, 209.

(19) R.-E. Nowak, M. Vehse, O. Sergeev, T. Voss, M. Seyfried, K. von Maydell, C. Agert, *Adv. Optical Mater.* **2014**, *2*, 94.

(20) A. P. Vasudev, J. A. Schuller, M. L. Brongersma, *Opt. Express* **2012**, *20*, A385.

(21) Y. Yao, J. Yao, V. K. Narasimhan, Z. Ruan, C. Xie, S. Fan, Y. Cui, *Nat. Commun.* **2012**, *3*, 664.

(22) J. Zhu, C.-M. Hsu, Z. Yu, S. Fan, Y. Cui, *Nano Lett.* **2010**, *10*, 1979.

(23) C.-M. Hsu, C. Battaglia, C. Pahud, Z. Ruan, F.-J. Haug, S. Fan, C. Ballif, Y. Cui, *Adv. Energy Mater.* **2012**, *2*, 628.

(24) K.-H. Tsui, Q. Lin, H. Chou, Q. Zhang, H. Fu, P. Qi, Z. Fan, *Adv. Mater.* **2014**, doi:10.1002/adma.201304938.

(25) N. D. Denkov, O. D. Velev, P. A. Kralchevsky, I. B. Ivanov, H. Yoshimura, K. Nagayama, *Langmuir* **1992**, *8*, 3183.

(26) X. Ye, L. Qi, *Nano Today* **2011**, *6*, 608.

(27) H. Zeng, X. Xu, Y. Bando, U. K. Gautam, T. Zhai, X. Fang, B. Liu, D. Golberg, *Adv. Funct. Mater.* **2009**, *19*, 3165.

(28) B. Cao, F. Sun, W. Cai, *Electrochem. Solid-State Lett.* **2005**, *8*, G237.

(29) Z. Liu, Z. Jin, J. Qiu, X. Liu, W. Wu, W. Li, *Semicond. Sci. Technol.* **2006**, *21*, 60.

(30) D. Ramírez, H. Gómez, D. Lincot, *Electrochim. Acta* **2010**, *55*, 2191.

(31) J. Elias, R. Tena-Zaera, C. Lévy-Clément, *J. Electroanal. Chem.* **2008**, *621*, 171.

(32) R. Tena-Zaera, J. Elias, C. Lévy-Clément, C. Bekeny, T. Voss, I. Mora-Seró, J. Bisquert, *J. Phys. Chem. C* **2008**, *112*, 16318.

(33) S. Peulon, D. Lincot, *J. Electrochem. Soc.* **1998**, *145*, 864.

(34) S. Peulon, D. Lincot, *Adv. Mater.* **1996**, *8*, 166.

(35) G. Bugnon, G. Parascandolo, S. Hänni, M. Stuckelberger, M. Charrière, M. Despeisse, F. Meillaud, C. Ballif, *Sol. Energy Mater. Sol. Cells* **2014**, *120*, 143.

(36) M. Vanecek, O. Babchenko, A. Purkrt, J. Holovsky, N. Neykova, A. Poruba, Z. Remes, J. Meier, U. Kroll, *Appl. Phys. Lett.* **2011**, *98*, 163503.

(37) H. Sai, K. Saito, N. Hozuki, M. Kondo, *Appl. Phys. Lett.* **2013**, *102*, 053509.

(38) C. Battaglia, C.-M. Hsu, K. Söderström, J. Escarré, F.-J. Haug, M. Charrière, M. Boccard, M. Despeisse, D. T. L. Alexander, M. Cantoni, Y. Cui, C. Ballif, *ACS Nano* **2012**, *6*, 2790.

(39) S. Geißendörfer, M. Vehse, T. Voss, J.-P. Richters, B. Hanke, K. von Maydell, C. Agert, *Sol. Energy Mater. Sol. Cells* **2013**, *111*, 153.

(40) I. Mora-Seró, F. Fabregat-Santiago, B. Denier, J. Bisquert, R. Tena-Zaera, J. Elias, C. Lévy-Clément, *Appl. Phys. Lett.* **2006**, *89*, 203117.

(41) R. Tena-Zaera, J. Elias, C. Lévy-Clément, I. Mora-Seró, Y. Luo, J. Bisquert, *phys. stat. sol. (a)* **2008**, *205*, 2345.

(42) M. Kemell, F. Dartigues, M. Ritala, M. Leskelä, *Thin Solid Films* **2003**, *434*, 20.

(43) M.G. Deceglie, V.E. Ferry, A.P. Alivisatos, and H.A. Atwater, Nano Lett. **2012** 12, 2894.

# Chapter 6: Polarization-Dependent Extraordinary Optical Transmission from Upconversion Nanoparticles

*This chapter is a manuscript in preparation for submission. Peng Hui Wang, Walter J. Salcedo, Jothirmayanantham Pichaandi, Frank C. J. M. van Veggel, Alexandre G. Brolo are the authors.*

*This work is a collaboration project with Dr. Frank van Veggel at the University of Victoria and Dr. Walter J. Salcedo at the University of Sao Paulo, in Brazil. Dr. Walter J. Salcedo performed the numerical simulation analysis. Jothirmayanantham Pichaandi synthesized the $NaYF_4$:$Yb^{3+}$/$Er^{3+}$nanoparticle. I fabricated the nanostructures; prepared the samples and performed all measurements.*

Enhanced (maximum ~6 times) upconversion (UC) emission was experimentally demonstrated using gold nanoparticles double antennas coupled to nanoslits in gold films. The transmitted red emission from UC ytterbium ($Yb^{3+}$) and erbium ($Er^{3+}$) co-doped sodium yttrium fluoride ($NaYF_4$:$Yb^{3+}$/$Er^{3+}$) nanoparticles (UC NPs) at ~665 nm (excited with a 980 nm diode laser) was enhanced relative to the green emission at ~550 nm. The relative enhanced UC NPs emission could be tuned by the different polarization-dependent extraordinary optical transmission (EOT) modes coupled to the gold nanostructures. Finite-difference time-domain (FDTD) calculations suggest that the preferential enhanced UC emission was related to a combination of different surface plasmon (SP) modes excitation coupling to cavity Fabry-Perot (FP) interactions.

## 6.1 Introduction

Extraordinary optical transmission (EOT) through metallic gratings, such as sub-wavelength holes and slits in thin metallic films, has been extensively studied[1-5] since reported by Ebbesen[6] in 1998. The EOT phenomenon has been implemented in several applications, including bio-sensing,[7] beam focusing[8, 9], and enhanced photovoltaics. [10-12] Lanthanide-doped upconversion (UC) emitters, which are capable of converting near-infrared radiation into visible fluorescence, also attract much research attention due to its potential for novel applications. For instance, when used as biological labels, UC nanomaterial present low photo-bleaching and their near-infrared excitation (typically 980 nm) falls within the optical biological window, allowing long penetration depth in tissues.[13] UC materials can also be used in microlasers[14] devices and up-conversion solar cells.[15, 16] UC nano-materials, however, often have poor external quantum efficiency, due to the low absorption coefficient, parasitic processes and quenching.[17, 18] It has been demonstrated that UC nanoparticles (UC NPs) luminescence can be enhanced when coupled to metallic nanostructures through resonant energy transfer (ET) involving surface plasmons (SPs).[17, 19, 20] The capability of engineering SP-active nanostructures[21] (geometry and surrounding dielectric) for enhanced UC EOT might have a potential for applications in photonics,[22, 23] and as sensitive single emitter detectors.[24-27]

In this work, polarized EOT from UC emissions were experimentally demonstrated by using Au double-antenna nanoparticles (DA NPs) nested in nanoslits in thin gold films. The roles of SP mode coupling and field confinement were evident in the EOT process.[28] It has also been shown that the presence of nanoparticles chains inside nanoslits significantly enhances light transmission relative to the slits without NPs.[2] The DA NPs inside nanoslits are expected to concentrate large electromagnetic fields in gap modes.[24, 29, 30] The nanoslits and DA NPs geometries were optimized to have their SP resonance overlapping with the UC NPs emission spectrum, facilitating the EOT at those wavelengths. The experimental results show a maximum overall UC enhancement (relative to a window reference) and an enhancement in the ratio between the transmitted UC red emission (~665 nm) and the green emission (~550 nm) of about 6-fold. The

preferential enhanced UC NPs emissions were strongly polarization dependent and could be tuned by different EOT modes, as confirmed by FDTD calculations.

## 6.2 Experimental section

### 6.2.1 Fabrication of the plasmonic nanostructures

The nanostructures were fabricated on 100 nm gold film (5 nm Cr was used as adhesion layer) deposited on 1 mm thick glass slide (commercially available from EMF, Ithaca, NY) by focused-ion-beam (FIB) milling. In general, the gallium ion beam was set with 40 keV at 12K magnification and the dwell time for each pixel was 5 ms. Two kinds of slit: 300 nm and 470 nm slit opening width (named as S300 and S470, respectively) were fabricated. The dimensions (length x width x height) of the DA NPs were 120 nm x 80 nm x 100 nm (characterized by scanning electron microscope (SEM) images, as shown in the inset of Figure 6−2b). DA NPs were fabricated in the center of the slits with different DA NPs gap distances: 14, 30, 120 and 180 nm, respectively (measured from SEM images, named as G14, G30, G120 and G180). SEM of all structures are shown as supplementary information (SI) Figure D−SI−1, Figure D−SI−2, and in Figure 6−2). The distance between two DA NPs dimer was kept constant at 250 nm. The slit periodicity was also kept constant at 700 nm. In addition, control samples consisting of a 80 nm width lines (instead of DA NPs) inside the slits (S300-Line, for instance) and empty slits (S) were also fabricated on the same gold film slide for comparison (Figure D−SI−1d, Figure D−SI−2d and Figure 6−7 inset SEM images). Each nanostructured square array was about 11.6 μm x 11.6 μm with 17 slits in each array. Furthermore, square windows with the same opening area slit structures (Figure D−SI−1e, without DA NPs and Line) were fabricated (for instance, the 7.7 μm x 7.7 μm S300-window matches the area of the S300-slit structure) as additional references (Figure D−SI−1f, Figure 6−6 and Figure 6−7 bottom inset SEM, and Figure D−SI−2). Lastly, a 10 nm $TiO_2$ layer was e-beam evaporated on top of FIB-fabricated nanostructure to further tune the DA NPs SP resonance to the UC NPs emission range.

### 6.2.2 Materials and sample preparation

All chemicals were purchased from Sigma Aldrich and used without further purification. The UC NPs were prepared in chloroform (3% w/v) according to the previous published experimental procedure.[31, 32] Then, the UC NPs suspension was spin coated on the nanostructured gold film glass slide at 1200 revolutions per minute. This resulted in an UC NPs film with a thickness of 220 ± 20 nm (estimated from the FIB cut cross section near the nanostructures).

### 6.2.3 Instrumentation

The experiment setup for the UC emission measurement is presented as Figure 6−1. The emission spectra were obtained under 980 nm continuous wave laser excitation with a fixed power density of 200 W/cm$^2$. The illumination area was about 100 μm$^2$ (shown in Figure 6−2d). The laser beam was incident normally onto the UC covered sample, then the UC emission was collected at the back of the sample with an objective lens (20X, NA 0.4), a spectrograph (HoloSpec VPT System from Kaiser) coupled to a CCD camera (DV-401-BV from ANDOR Technology) was used as a detection system (Figure 6−1). The sample orientation and light polarization directions were rotated accordingly to measure the UC emission spectra under different polarizations (Figure 6−3). The transmittance experiments for UC film covered nanostructures were measured using a fiber (400 μm core diameter) coupled optical microscope (OLYMPUS MS PLAN ULWD 50X NA 0.55 objective) with polarized white light and a UV/VIS/NIR spectrometer (Ocean Optics 4000) were used as a detection system. SEM images were taken using a scanning electron microscope Hitachi S4800 at 1kV acceleration voltage.

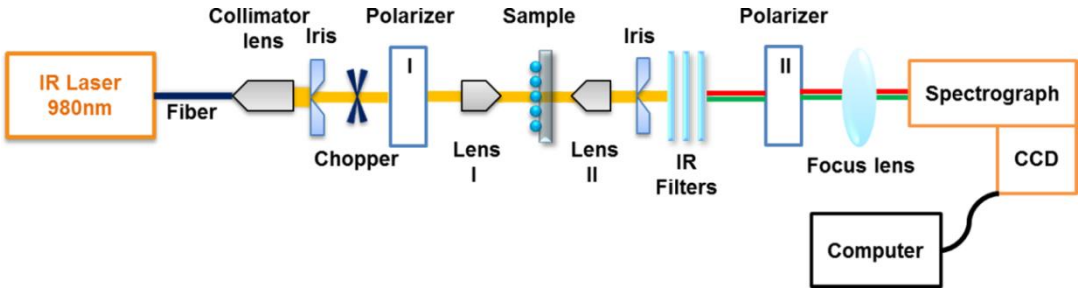


**Figure 6−1** Schematic of experiment measurement system for UC emission measurement. Sample and polarizer II are rotated 90º accordingly in this experiment.

### 6.2.4 FDTD simulations

FDTD simulations (Lumerical software Inc.) were performed to visualize the electric field intensity profiles around the nanostructures. The dimensions of the nanostructures were based on the average measurements from the SEM images as mentioned above. A rectangular polygon with rounded corners was used to model the DA NPs. The dielectric properties of the gold and chromium were the default data reported by Johnson and Christy[33] and Palik[34] respectively, imported directly from the Lumerical material data base. Periodic boundary conditions were used in xy direction and with PML (perfect metal layers) in the ±z directions. Plane wave source was placed 1µm above Au nanostructures. The UC NP film refractive index[35] (n) was set as 1.50 above Au metallic structure with 240 nm thickness assuming an uninform coverage; the glass substrate refractive index[34] (n) was import from Lumerical material data base. 10 nm $TiO_2$ dielectric layer was placed on top of Au slits bars, and the $TiO_2$ dielectric refractive index was obtained from the tabulated data.[36] An effective refractive index inside the slits was chosen as 1.85, considering non-uniform coverage of the $TiO_2$ layer UC NPs inside the slits, and a better transmittance agreement between the simulation and experiment. Near field and transmission monitor were placed at the back of the nanostructures (12 nm and 1.3 µm away from the DA nanostructures, respectively). 3 nm mesh size was used near Au nanostructures.

## 6.3 Result and discussions

The gold nanostructures were fabricated by FIB milling on 100 nm gold film. Figure 6−2a and b present SEM images of two slits arrays with 300 and 470 nm openings containing DA NPs with a gap distance of 30 nm (S300-G30 and S470-G30, respectively). Other arrays are shown as in Figure D−SI−1 and Figure D−SI−2 (see method section for the details). Figure 6−2c shows an SEM image of the UC NPs covering a nanostructured Au substrate. The SEM image indicates a homogenous coverage with a random UC NPs (UC NPs diameter was ~ 30 nm) packed film on top of the nanostructured Au surface. Figure 6−2d presents an optical image of a gold film containing two nanostructured square arrays. The whole surface (including the nanostructures) was covered with UC NPs. One of the arrays in Figure 6−2d is illuminated by laser, and the inset shows details of a dark field image under laser illumination. Each square array in a given slide consisted of different nanostructures (as indicated above) and was excited individually using a 980 nm laser (illustrated by the bright spot in Figure 6−2d). The UC emission from each array was collected under various excitation and collection configurations defined in Figure 6−3. The UC experimental measurement setup details are shown in Figure 6−1.

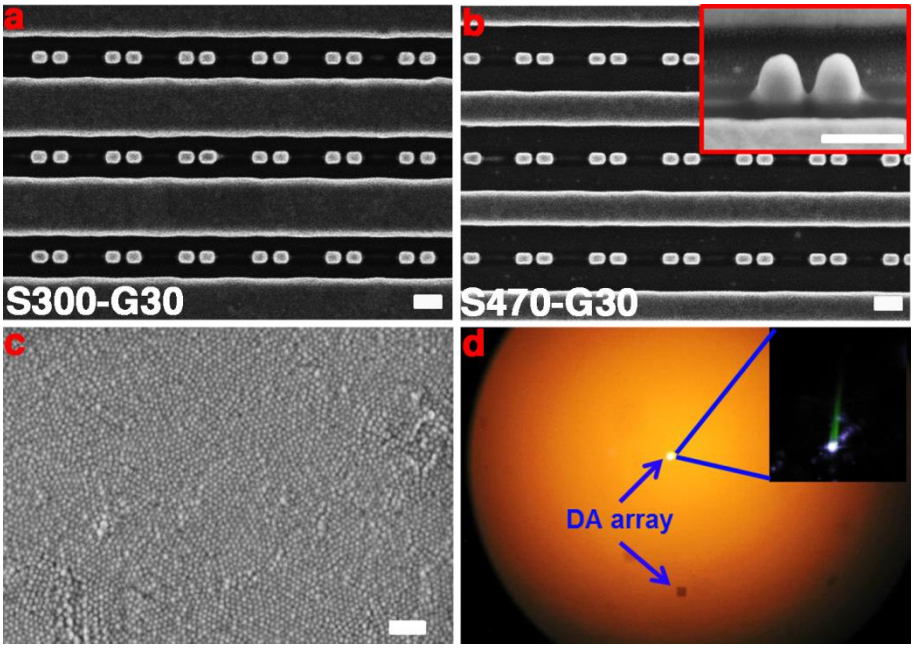


**Figure 6−2**(a) and (b) SEM image top view of double antenna (DA) Au DA NPs structure inside a nanoslit: S300-G30 and S470-G30 respectively; the side view of a pair of DA is shown (as an inset image, substrate titled at 45º). (c) UC NPs film covering nanostructured array on the gold substrate. (d) Optical microscope image of UC NPs covered DA arrays on the gold film, one array is shown with 980 nm laser excitation from an nanostructured DA array, the inserted optical image shows the UC emission in the dark. Dimensions: scale bar (a), (b) and (c) 200nm, (d) each nanostructured square array is about 11.6 x 11.6 μm$^2$.

It is known that the light transmitted through a periodic slit structure strongly depends on its polarization.[2] The coupling of UC emissions to these polarization effects might be useful, for instance, in the generation of optical switches and polarization sensitive detectors.[37] In this work, the excitation polarization was fixed, but the relative orientation of the sample and polarizer II (Figure 6−3 and Figure 6−1) ) were adjusted for different measurements. Figure 6−3 defines the four types of excitation/collection configurations: named as xxx, xxy, xyx, and xyy, respectively, where the first letter “x” defines the fixed incident light polarization (either white light or the 980 nm laser, red color arrow); the second letter either “x” or “y” defines the slits orientation relative to the incident polarization; and the third letter either “x” or “y” indicates the direction of polarizer

(analyzer) used in the measurement of the transmitted UC emission from the back of the sample oriented relative to the incident light polarization.

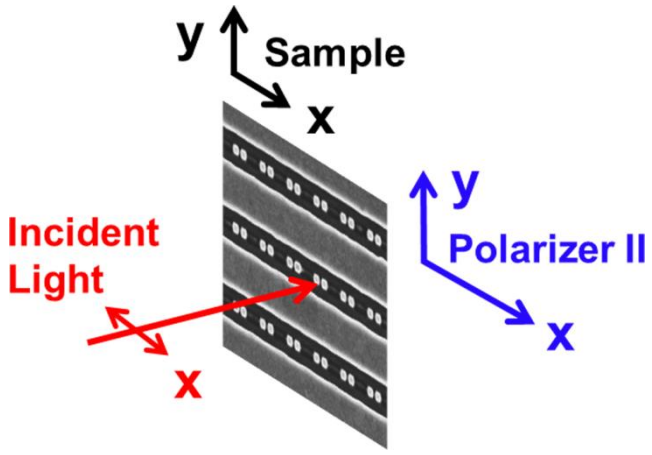


**Figure 6−3** Schematic of experiment configurations and definitions for UC emission measurement. Incident light polarization was fixed at normal incidence (red color); sample and polarizer II were rotated 90° accordingly during the measurement.

Before measuring the UC emission, each nanostructured array was characterized by polarized white light transmission (the same conditions as the laser excitation experiment, at normal incidence) to map the relative position of the SP resonances of the nanostructures relative to the UC NPs emission bands. Figure 6−4 presents an example of white light transmittance spectra with xxx (Figure 6−4a) and xyx (Figure 6−4b) configuration for the DA NPs nanostructure with S300-G14 and S300-Slit array (the results for the other arrays are summarized in the SI, Figure D−SI−3), respectively. The white light transmission spectra with the other xxy and xyy configurations have very small transmission detected due to the crossed polarizers (Figure 6−1 I and II) that significantly blocked the amount of light that reached the detector. The transmittance spectra was calculated from the white light transmission spectra ($\frac{I^{WL}_{array}}{I^{WL}_{window}}$), where $I^{WL}_{array}$ is the measured white light transmission from a nanostructured array, and $I^{WL}_{window}$ is the measured white light transmission from the window reference (see Figure D−SI−1f). An UC emission spectrum is also included in Figure 6−4 (black plot at the bottom of the

figures) for comparison. FDTD calculations (dashed lines in Figure 6−4) were performed to provide additional insights about the optical processes. Due to the complicated nature of the systems investigated here, including the presence of fabrication defects; the variations in packing density for solid UC NPs films; the quality of the $TiO_2$ film; and the precise geometry of the metallic nanostructures;[38] an exact quantitative agreement between the experiments and simulations is not to be expected. However, the transmittance peaks/dips features predicted by FDTD qualitatively agree with the experimental results. The experimental measurements (solid lines) in Figure 6−4 present a broadening of the features due to fabrication defects and measurement conditions. Normally, periodic nanoslits in gold film do not support strong white light transmission in the xxx configuration (transverse electric – TE polarization).[39, 40] However, the presence of a thin dielectric (UC NPs) film coating the slit-only arrays enables significant white light transmission (blue lines in Figure 6−4) in that configuration (xxx). This observed EOT for slits in transverse electric (TE) configuration (xxx) in presence of a dielectric film has been reported from other groups.[41-43] Figure 6−4 illustrates that the UC green and red emission bands present different degrees of overlap with the transmittance spectrum, as expected (see dashed vertical lines in Figure 6−4). FDTD calculations indicate that the dip positions at ~ 800 nm (Figure 6−4a) correspond to a Fabry-Perot (FP) destructive mode in the transmission. The transmittance dip position at ~667 nm (Figure 6−4a red color) in the presence of Au DA NPs is also related to a FP destructive mode that couples to the Au DA NPs localized SP mode. Under the xyx configuration, Figure 6−4b, the transmittance dip positioned at ~700 nm corresponds to the activation of grating induced SP polariton and increased back reflection. The presence of Au DA NPs inside the slits (Figure 6−4 S300-G14, red color) decreases the white light transmittance due to the combination of decreased opening area (~13%), increased back reflection, and additional Au NPs parasitic absorption compared to the slits without Au DA NPs (blue color). Most importantly, the EOT mechanism with additional nanostructures inside nanoslits is different than for the slit only nanostructures. The characteristics of these different EOT modes are further visualized in the numerical simulations presented in Figure 6−5.

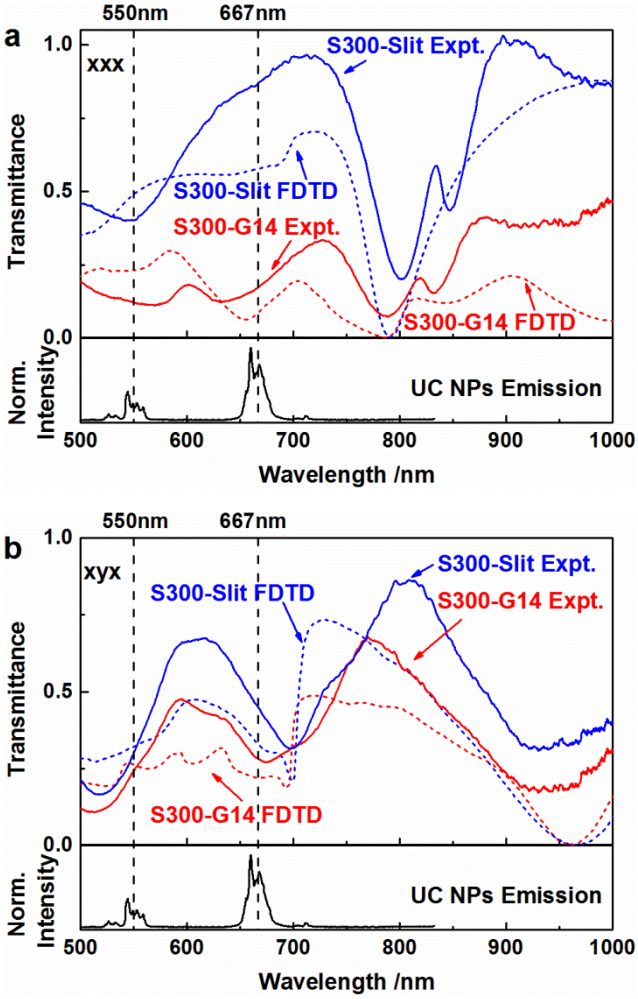


**Figure 6−4** Experimental (solid lines) and FDTD calculated (dashed lines) xxx (a) and xyx (b) transmittance spectrum for S300-G14 DA and S300-Slit nanostructured array, respectively. A normalized UC emission spectrum from S300-window reference is added (black color) for comparison.

FDTD-calculated electric field profiles (at the position of the dashed lines in Figure 6−4, which correspond to the UC emission positions) for some of the nanostructures studied here are presented in Figure 6−5. Figure 6−5a presents the selected SEM images of the different types of arrays investigated (S300 set). The near electric field intensity distributions at the transmitted position (12 nm bellow the DA Au NPs) were plotted in Figure 6−5b-e for wavelengths at 667 nm (red) and 550 nm (green). The incident light was polarized either parallel or perpendicular to the slit (indicated as the red arrow on the

right side). Figure 6−5b-e shows that different SP resonance modes is activated under different polarizations, and the electric field intensity is distributed spatially differently around the nanostructures in the red and green spectral regions. These different polarization-dependent modes affect the characteristics of the enhanced UC, as will be demonstrated later. Two major characteristics are observed from the numerical FDTD-calculations:

(1) The enhanced electric field intensity is concentrated near the Au NPs (in x direction) when light coupled to DA NPs in the parallel polarization direction (x-direction). In this case the DA NP-NP gap mode (named as "NP-NP gap mode") is activated (Figure 6−5b and c DA NPs). On the other hand, when light couple to slit in perpendicular polarization (Figure 6−5d and e), the electric field is distributed along the y direction; concentrated in the gap between the lateral of the DA nanoparticles and the slit walls. In this case, DA-slit wall modes (named as "DA-slit wall mode") are activated (Figure 6−5d and e).

(2) The magnitude of the local electric field intensity for red light is always greater than the green electric field near the DA NPs for the particular geometries investigated here.

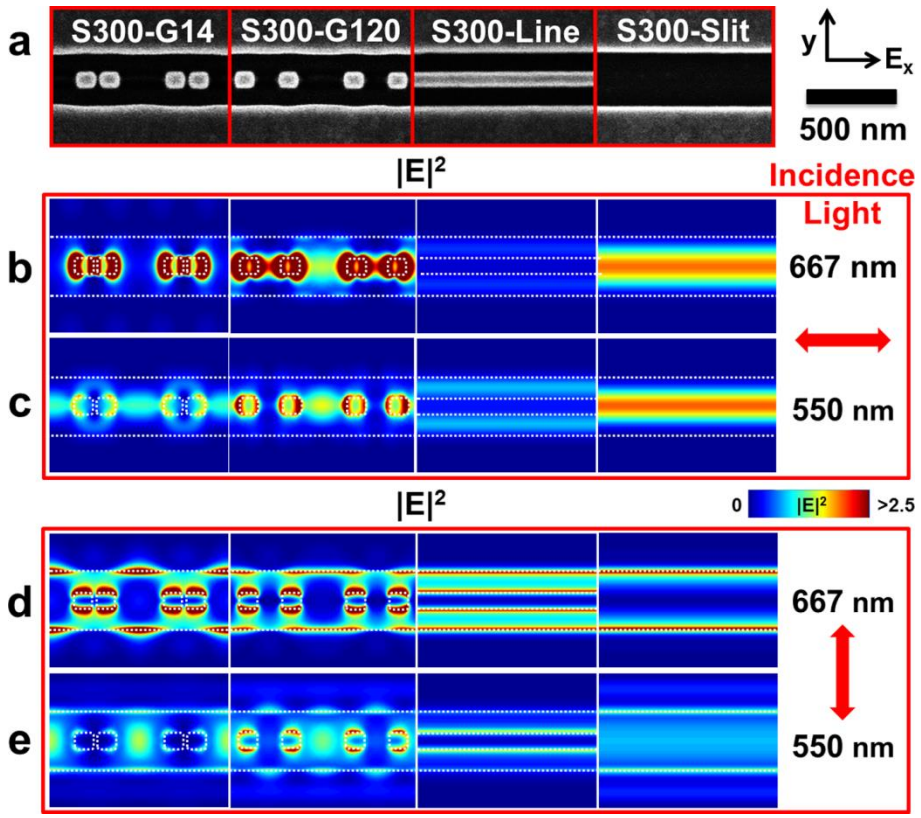


**Figure 6−5** FDTD-calculated near field electric intensity ($|E|^2$) distribution for (a) S300-G14, S300-G120, S300-Line and S300-Slit nanostructures at the transmission position with the incidence light (red arrow) parallel (b-c) and perpendicular (d-e) to the nanoslits, respectively. The color scale is optimized to view the near field at different wavelengths (indicated beside the graph); the slit and DA NPs positions are outlined (white dashed lines).

As for the S300-Line and S300-Slit samples, references without DA NPs inside (Figure 6−5b and c), an enhanced electric field is also observed for xxx polarization. The electric field in this case is centered on the slit gap, and, consequently, less bounded to the metallic surface. This indicates the activation of FP-like interference due to the thin dielectric film present on top of the slit structures; note that this is not related to the SP resonance. On the other hand, when light is polarized perpendicular to the slit (Figure 6−5d and e), the “slit wall mode” is activated due to the activation of SP modes (Figure 6−5d and e). The SP modes overlapped better with the red emission than with the green under perpendicular polarization. In summary, the activation of the different modes

("NP-NP gap mode" and "DA-slit wall mode") are responsible for the polarization dependence of the observed white light transmittance features observed in Figure 6−4.

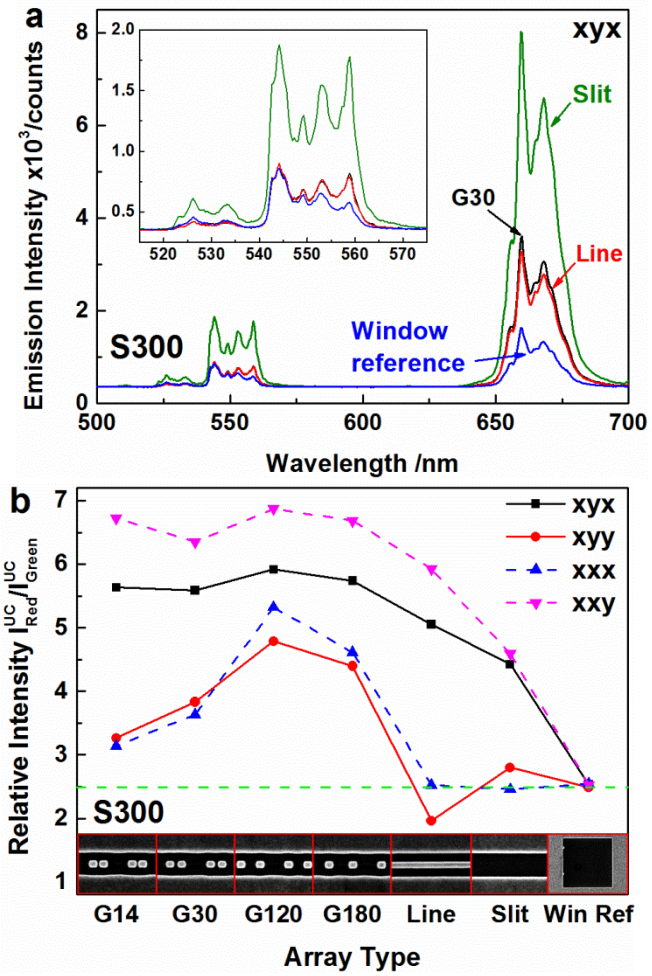


**Figure 6−6** (a) Samples of UC NPs emission spectra from different nanostructures as indicated in the figure, all the spectra were taken under the same xyx condition with S300 sample. (b) Relative integrated UC emission intensity between the red (from 640 nm to 690 nm) and the green (from 520 nm to 570 nm) emission ($\frac{I^{UC}_{Red}}{I^{UC}_{Green}}$) for each nanostructured S300 array under different measurement configurations (indicated in the figure) are presented.

Figure 6−4 and Figure 6−5 provide important insights into the EOT mechanisms through the nanostructures enabled by distinct optical modes. The effect of these modes on the transmitted UC will now be explored. As presented in the experimental section, the UC NPs were excited by a 980 nm laser, reaching the particles directly at normal

incidence, and the UC emission was measured in transmission mode. It is assumed that each UC NP emits as a dipole source, since the UC NPs are typically single crystals, all the photoluminescent-active $Ln^{3+}$ dopant ions are in a well-defined crystals field. The UC NPs film on top of the nanostructures was relatively thick (~240 nm), and the emission from that collective random distribution of dipoles can be considered, at a first approximation, as an un-polarized plane wave source travelling towards the nanostructured surface. This un-polarized UC emissions would have different transmissions in the x and y directions, as discussed above. A polarizer after the slit nanostructures (Figure 6−3 and Figure 6−1) allows the experimental evaluation of the enhanced UC emission transmission for the different polarizations. Examples of UC emission spectra obtained with xyx orientation from some of the nanostructures are shown in Figure 6−6a. The UC material exhibited characteristic green emissions ~530 nm and ~550 nm, assigned to the $^2H_{11/2} \rightarrow {}^4I_{15/2}$ and $^4S_{3/2} \rightarrow {}^4I_{15/2}$ transitions from $Er^{3+}$ ions, respectively, and a red emission, ~665 nm, associated with the $^4F_{9/2} \rightarrow {}^4I_{15/2}$ $Er^{3+}$ transition.[31] In Figure 6−6a, the red transmitted UC emission intensities are enhanced selectively for the different types of nanostructures, when compared to the window reference. The intensities of the transmitted emissions were dependent on the type of nanostructure and on the measurement configuration. A summary of the relative absolute effect of the nanostructures in the UC emission (using the window as reference) is presented in the SI file (Figure D−SI−4). The red emission was enhanced in all structures and the slit structure presented the maximum (~ 6 fold) UC increase.

The enhanced transmitted UC emission is induced by the interactions between the UC NPs and the metallic nanostructures. Plasmonic-enhanced UC photoluminescence is often due to the UC NPs interaction with the enhanced local electric field near the metallic nanostructures.[28, 44-46] In EOT, light is able to pass through metallic openings smaller than its wavelength mediated by SP resonance. The enhanced near electric field intensity plays then a significant role on both enhanced UC and transmission.[2, 28, 38, 46] The UC film in this experiment was relative thick (~240 nm, in order to obtain an uniform coverage) compared to the normal “skin deep” (~30 nm) enhanced plasmonic near field spatial extension. Since the average UC NP diameter is also ~30 nm, only the first layer of UC NPs (about 15% of the film) are expected to be strongly affected by the

enhanced plasmonic near field. The enhanced transmitted UC emission mechanisms are hard to decouple due to complicated nature of the experiment setup, this would be a subject of future work with only a single UC NP layer coverage. Nevertheless, the effect of the nanostructures (DA NPs and line) inside the slits led to tunable enhancement effect, illustrated by the variation in the relative red and the green UC transmitted emission intensity ($\frac{I_{Red}^{UC}}{I_{Green}^{UC}}$). The relative intensity ratios ($\frac{I_{Red}^{UC}}{I_{Green}^{UC}}$), for both green (integrated from 520 nm to 570 nm) and red emissions (from 640 nm to 690 nm), were calculated and are plotted in Figure 6−6b. Figure 6−6b shows a polarization dependent tunable preferential enhancement of the red UC transmitted emission for the nanostructured arrays compared to the window reference. The presence of the Au DA nanostructures insides the slits (S300-G14 to G180) induces even higher preferential enhanced red UC transmitted emission relative to green emission compare to the slit only (S300-Slit) structure. As for the window reference, there are no polarization dependence ($\frac{I_{Red}^{UC}}{I_{Green}^{UC}}$ = ~2.5) as expected.

Through the activation of the different EOT mode ("NP-NP gap mode" and "DA-slit wall mode"), the observed UC emissions show strong polarization dependence. The free-space light and SP resonance mode coupling efficiency[29, 47] often affects the EOT intensities. Both experimental and FDTD-calculated results indicated an enhanced red light relative to the green light as expected. The highest preferential enhanced $\frac{I_{Red}^{UC}}{I_{Green}^{UC}}$ emission is observed from the S300-Slit under the "DA-slit wall mode" (Figure 6−6b, xyx black and xxy magenta color) polarization. Increases the slit width generally decreases the theoretical slit mode SP resonance coupling efficiency.[46, 47] This should also affect the UC emissions EOT intensities. Figure 6−7 presents an experimental result of the relative enhanced UC emission with the same set of nanostructures as S300 arrays (dashed lines, Figure 6−7 SEM inset on the top) but a large slits nanostructures (S470) and a large window reference (solid line, Figure 6−7 SEM inset on the bottom) on the same substrate. The preferential enhanced red emission ($\frac{I_{Red}^{UC}}{I_{Green}^{UC}}$) was significantly lower for the larger slit (S470) width compared to the narrow nanoslits (S300). This is

corresponding to the "DA-slit wall mode" interaction blue shifts with the increase of the NP-wall distance, favoring an increase in the green UC emission.

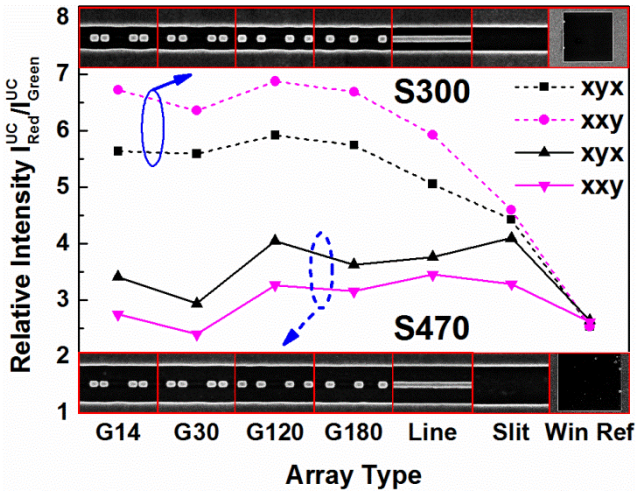


**Figure 6−7** Comparison of the tunable feature of the relative UC emission between the red (from 640 nm to 690 nm) and the green (from 520 nm to 570 nm) emission ($\frac{I^{UC}_{Red}}{I^{UC}_{Green}}$) with a large slit (S470, solid lines) and the narrow slits (S300, dashed lines) for each nanostructured array are presented.

## 6.4 Conclusion

The enhanced upconversion (UC) emission through plasmonic interactions between $NaYF_4$:Yb/Er and gold nanostructures was investigated. The UC transmission presented a polarization effect, tuned by the plasmonic nanostructures. In general, a preferential enhancement of the red emission over the green UC emission was observed for all nanostructures (double antenna nanoparticles and lines) nested in two kinds (300 and 470 nm slit opening) of nanoslits. FDTD-calculations suggest that the UC enhancement and the polarization effects resulted from different electric field modes activated by different polarizations. We hope our finding would provide a new insight for applications, such as efficient UC polarizer for possible single photon quantum computation, communication [27, 48] and solar cell devices.

## 6.5 Reference


(1) Lalanne, P.; Hugonin, J. P.; Rodier, J. C. Theory of Surface Plasmon Generation at Nanoslit Apertures. Phys. Rev. Lett. 2005, 95, 263902.

(2) Kofke, M. J.; Waldeck, D. H.; Walker, G. C. Composite Nanoparticle Nanoslit Arrays: A Novel Platform for Lspr Mediated Subwavelength Optical Transmission. *Opt. Express* **2010,** *18*, 7705-7713.

(3) Gordon, R.; Brolo, A. G.; Sinton, D.; Kavanagh, K. L. Resonant Optical Transmission through Hole-Arrays in Metal Films: Physics and Applications. *Laser & Photonics Reviews* **2010,** *4*, 311-335.

(4) Garcia-Vidal, F. J.; Martin-Moreno, L.; Ebbesen, T. W.; Kuipers, L. Light Passing through Subwavelength Apertures. *Rev. Mod. Phys.* **2010,** *82*, 729-787.

(5) Weiner, J. The Physics of Light Transmission through Subwavelength Apertures and Aperture Arrays. *Rep. Prog. Phys.* **2009,** *72*, 064401.

(6) Ebbesen, T. W.; Lezec, H. J.; Ghaemi, H. F.; Thio, T.; Wolff, P. A. Extraordinary Optical Transmission through Sub-Wavelength Hole Arrays. *Nature* **1998,** *391*, 667-669.

(7) Brolo, A. G. Plasmonics for Future Biosensors. *Nat Photon* **2012,** *6*, 709-713.

(8) Chrostowski, L. Optical Gratings: Nano-Engineered Lenses. *Nat Photon* **2010,** *4*, 413-415.

(9) Søndergaard, T.; Bozhevolnyi, S. I.; Novikov, S. M.; Beermann, J.; Devaux, E. s.; Ebbesen, T. W. Extraordinary Optical Transmission Enhanced by Nanofocusing. *Nano Lett.* **2010,** *10*, 3123-3128.

(10) Ferry, V. E.; Munday, J. N.; Atwater, H. A. Design Considerations for Plasmonic Photovoltaics. *Adv. Mater.* **2010,** *22*, 4794-4808.

(11) Gao, T.; Wang, B.; Ding, B.; Lee, J.-k.; Leu, P. W. Uniform and Ordered Copper Nanomeshes by Microsphere Lithography for Transparent Electrodes. *Nano Lett.* **2014**.

(12) Ashwin, C. A.; Aitzol, G.-E.; Hadiseh, A.; Jennifer, A. D. Toward High-Efficiency Solar Upconversion with Plasmonic Nanostructures. *Journal of Optics* **2012,** *14*, 024008.

(13) Pichaandi, J.; Boyer, J.-C.; Delaney, K. R.; van Veggel, F. C. J. M. Two-Photon Upconversion Laser (Scanning and Wide-Field) Microscopy Using Ln3+-Doped Nayf4 Upconverting Nanocrystals: A Critical Evaluation of Their Performance and Potential in Bioimaging. *J. Phys. Chem. C* **2011,** *115*, 19054-19064.

(14) Shi, C.; Soltani, S.; Armani, A. M. Gold Nanorod Plasmonic Upconversion Microlaser. *Nano Lett.* **2013,** *13*, 5827-5831.

(15) van Sark, W.; de Wild, J.; Rath, J.; Meijerink, A.; Schropp, R. E. Upconversion in Solar Cells. *Nanoscale Research Letters* **2013,** *8*, 81.

(16) Zhou, Z.; Wang, J.; Nan, F.; Bu, C.; Yu, Z.; Liu, W.; Guo, S.; Hu, H.; Zhao, X.-Z. Upconversion Induced Enhancement of Dye Sensitized Solar Cells Based on Core-Shell Structured [Small Beta]-Nayf4:Er3+, Yb3+@Sio2 Nanoparticles. *Nanoscale* **2014,** *6*, 2052-2055.

(17) Rivera, V. A. G.; Ferri, F. A.; Jr., E. M., *Localized Surface Plasmon Resonances: Noble Metal Nanoparticle Interaction with Rare-Earth Ions*. 2012.

(18) Auzel, F. Upconversion and Anti-Stokes Processes with F and D Ions in Solids. *Chem. Rev.* **2004,** *104*, 139-173.

(19) Luu, Q.; Hor, A.; Fisher, J.; Anderson, R. B.; Liu, S.; Luk, T.-S.; Paudel, H. P.; Farrokh Baroughi, M.; May, P. S.; Smith, S. Two-Color Surface Plasmon Polariton Enhanced Upconversion in Nayf4:Yb:Tm Nanoparticles on Au Nanopillar Arrays. *J. Phys. Chem. C* **2014,** *118*, 3251-3257.

(20) Sun, Q.-C.; Mundoor, H.; Ribot, J. C.; Singh, V.; Smalyukh, I. I.; Nagpal, P. Plasmon-Enhanced Energy Transfer for Improved Upconversion of Infrared Radiation in Doped-Lanthanide Nanocrystals. *Nano Lett.* **2013,** *14*, 101-106.

(21) Nathan, C. L.; Prashant, N.; Kevin, M. M.; David, J. N.; Sang-Hyun, O. Engineering Metallic Nanostructures for Plasmonics and Nanophotonics. *Rep. Prog. Phys.* **2012,** *75*, 036501.

(22) Livneh, N.; Strauss, A.; Schwarz, I.; Rosenberg, I.; Zimran, A.; Yochelis, S.; Chen, G.; Banin, U.; Paltiel, Y.; Rapaport, R. Highly Directional Emission and Photon Beaming from Nanocrystal Quantum Dots Embedded in Metallic Nanoslit Arrays. *Nano Lett.* **2011,** *11*, 1630-1635.

(23) Zhang, T.; Shan, F. Development and Application of Surface Plasmon Polaritons on Optical Amplification. *Journal of Nanomaterials* **2014,** *2014*, 16.

(24) Aouani, H.; Rahmani, M.; Navarro-Cia, M.; Maier, S. A. Third-Harmonic-Upconversion Enhancement from a Single Semiconductor Nanoparticle Coupled to a Plasmonic Antenna. *Nat Nano* **2014,** *9*, 290-294.

(25) Aouani, H.; Mahboub, O.; Devaux, E.; Rigneault, H.; Ebbesen, T. W.; Wenger, J. Plasmonic Antennas for Directional Sorting of Fluorescence Emission. *Nano Lett.* **2011,** *11*, 2400-2406.

(26) Wong, T.-H.; Yu, J.; Bai, Y.; Johnson, W.; Chen, S.; Petros, M.; Singh, U. N. Sensitive Infrared Signal Detection by Upconversion Technique. *OPTICE* **2014,** *53*, 107102-107102.

(27) Ma, L.; Slattery, O.; Tang, X. Single Photon Frequency up-Conversion and Its Applications. *Phys. Rep.* **2012,** *521*, 69-94.

(28) Verhagen, E.; Kuipers, L.; Polman, A. Field Enhancement in Metallic Subwavelength Aperture Arrays Probedby Erbium Upconversion Luminescence. *Opt. Express* **2009,** *17*, 14586-14598.

(29) Zhang, W.; Ding, F.; Chou, S. Y. Large Enhancement of Upconversion Luminescence of Nayf4:Yb3+/Er3+ Nanocrystal by 3d Plasmonic Nano-Antennas. *Adv. Mater.* **2012,** *24*, OP236-OP241.

(30) Thyagarajan, K.; Rivier, S.; Lovera, A.; Martin, O. J. F. Enhanced Second-Harmonic Generation from Double Resonant Plasmonic Antennae. *Opt. Express* **2012,** *20*, 12860-12865.

(31) Johnson, N. J. J.; Sangeetha, N. M.; Boyer, J.-C.; van Veggel, F. C. J. M. Facile Ligand-Exchange with Polyvinylpyrrolidone and Subsequent Silica Coating of Hydrophobic Upconverting [Small Beta]-Nayf4:Yb3+/Er3+ Nanoparticles. *Nanoscale* **2010,** *2*, 771-777.

(32) Boyer, J.-C.; Manseau, M.-P.; Murray, J. I.; van Veggel, F. C. J. M. Surface Modification of Upconverting Nayf4 Nanoparticles with Peg−Phosphate Ligands for Nir (800 Nm) Biolabeling within the Biological Window. *Langmuir* **2009,** *26*, 1157-1164.

(33) Johnson, P. B.; Christy, R. W. Optical Constants of the Noble Metals. *Phys. Rev. B* **1972,** *6*, 4370-4379.

(34) Palik, E. D., *Handbook of Optical Constants of Solids*. Acad. Press: Boston u.a., 1997.

(35) Fischer, S.; Steinkemper, H.; Löper, P.; Hermle, M.; Goldschmidt, J. C. Modeling Upconversion of Erbium Doped Microcrystals Based on Experimentally Determined Einstein Coefficients. *J. Appl. Phys.* **2012,** *111*, 013109.

(36) Devore, J. R. Refractive Indices of Rutile and Sphalerite. *J. Opt. Soc. Am.* **1951,** *41*, 416-417.

(37) Wang, J.; Gudiksen, M. S.; Duan, X.; Cui, Y.; Lieber, C. M. Highly Polarized Photoluminescence and Photodetection from Single Indium Phosphide Nanowires. *Science* **2001,** *293*, 1455-1457.

(38) Liang, Y.; Peng, W.; Hu, R.; Zou, H. Extraordinary Optical Transmission Based on Subwavelength Metallic Grating with Ellipse Walls. *Opt. Express* **2013,** *21*, 6139-6152.

(39) Zhang, D.; Wang, P.; Jiao, X.; Min, C.; Yuan, G.; Deng, Y.; Ming, H.; Zhang, L.; Liu, W. Polarization Properties of Subwavelength Metallic Gratings in Visible Light Band. *Appl. Phys. B* **2006,** *85*, 139-143.

(40) Schwarz, I.; Livneh, N.; Rapaport, R. General Closed-Form Condition for Enhanced Transmission in Subwavelength Metallic Gratings in Both Te and Tm Polarizations. *Opt. Express* **2012,** *20*, 426-439.

(41) Zhijun, S.; Tengpeng, G.; Wei, C.; Xiaoliu, Z. Transmission of Te-Polarized Light through Metallic Nanoslit Arrays Assisted by a Quasi Surface Wave. *Applied Physics Express* **2014,** *7*, 032001.

(42) Esteban, M.; Martín-Moreno, L.; García-Vidal, F. J. Extraordinary Optical Transmission without Plasmons: The S-Polarization Case. *Journal of Optics A: Pure and Applied Optics* **2006,** *8*, S94.

(43) Guillaumée, M.; Nikitin, A. Y.; Klein, M. J. K.; Dunbar, L. A.; Spassov, V.; Eckert, R.; Martín-Moreno, L.; García-Vidal, F. J.; Stanley, R. P. Observation of Enhanced Transmission for S-Polarized Light through a Subwavelength Slit. *Opt. Express* **2010,** *18*, 9722-9727.

(44) Schietinger, S.; Aichele, T.; Wang, H.-Q.; Nann, T.; Benson, O. Plasmon-Enhanced Upconversion in Single Nayf4:Yb3+/Er3+ Codoped Nanocrystals. *Nano Lett.* **2009,** *10*, 134-138.

(45) Zhang, H.; Li, Y.; Ivanov, I. A.; Qu, Y.; Huang, Y.; Duan, X. Plasmonic Modulation of the Upconversion Fluorescence in Nayf4:Yb/Tm Hexaplate Nanocrystals Using Gold Nanoparticles or Nanoshells. *Angew. Chem. Int. Ed.* **2010,** *49*, 2865-2868.

(46) Lu, D.; Cho, S. K.; Ahn, S.; Brun, L.; Summers, C. J.; Park, W. Plasmon Enhancement Mechanism for the Upconversion Processes in Nayf4:Yb3+,Er3+ Nanoparticles: Maxwell Versus Förster. *ACS Nano* **2014,** *8*, 7780-7792.

(47) Mehfuz, R.; Maqsood, M. W.; Chau, K. J. Enhancing the Efficiency of Slit-Coupling to Surface-Plasmon-Polaritons Via Dispersion Engineering. *Opt. Express* **2010,** *18*, 18206-18216.

(48) Rakher, M. T.; Ma, L.; Slattery, O.; Tang, X.; Srinivasan, K. Quantum Transduction of Telecommunications-Band Single Photons from a Quantum Dot by Frequency Upconversion. *Nat Photon* **2010,** *4*, 786-791.

# Chapter 7 Summary and Outlook

This chapter contains the summary and conclusion for this thesis. An outlook and future direction is briefly discussed.

## 7.1 Summary and conclusion

In this work, we performed a systematic investigation on the energy transfer mediated by metallic surface plasmon (SP) nanostructures. The fabrication, characterization and application of surface plasmon active material in energy conversion field have been investigated, and the photonic nanostructures for thin film silicon solar cell also demonstrated

For the application of SP nanostructures in the photovoltaic device in part II, we have successfully shown that mixed Ag and Au NPs can be immobilized on the top of Si PV devices to improve their overall efficiency. The surface coverage and size dependence of Au NPs on the EQE were studied systematically. $\%\Delta EQE(\lambda)$ enhancement was strongly dependent on the forward scattering efficiency. The enhancement of the far field electromagnetic radiation is the main contribution from random immobilized Au/Ag mixture on top of a c-Si solar cell (Chapter 3). As for the application of the SP nanostructures on the back of thin film solar cell, we were able to show that similar light trapping properties are obtained with identically shaped Al-, Au- and Ag-NPs and $SiO_2$-NPs features. As significant improvements were achieved with both metallic and nonmetallic NPs over the commercial textured reference, we conclude that the geometry of the structure has a much higher influence on the light trapping properties compared to its material. Specifically, the front side textures seem to have a major influence on the light distribution inside the cell. Finally, we deduce two major findings from our study: Firstly, one should aspire to use non-metallic particles because of the lower parasitic absorption associated with them. Secondly, but not of less importance, the influence of the light trapping structure on the electrical properties of the solar cell needs to be taken into account (Chapter 4).

Then, a low-cost and scalable bottom-up approach to fabricate nanostructured ZnO electrodes for enhanced optical absorption in thin-film solar cells was presented (chapter 5. The concept is based on the growth of honeycomb patterned ZnO structures by electrochemical deposition, preceded by a nanosphere lithography step. This approach induces a folding of the solar cell around the ZnO structure, resulting in strongly

enhanced optical properties due to an overall increased absorber volume. Thin a-Si:H solar cells, with an intrinsic absorber layer thickness of 100 nm, were used as proof of concept, and a significantly enhanced EQE was observed. The short circuit current density was almost 10% higher compared to a solar cell on an optimized commercial textured ZnO reference electrode. The process suggested in Chapter 5 is compatible with low-cost substrates, such as polymers and metal foils, and allows an optimization of the structure for any desired cell concept. The periodicity can be easily controlled by the nanosphere size. No sophisticated layer stacks or expensive techniques are required, and therefore, the concept is highly promising for a low-cost industrial fabrication of nanostructured thin-film solar cells.

Furthermore, enhanced upconversion (UC) emission through plasmonic interactions between $NaYF_4$:Yb/Er and gold nanostructures was investigated. The UC transmission presented a polarization effect, tuned by the plasmonic nanostructures. In general, a preferential enhancement of the red emission over the green UC emission was observed for all nanostructures (double antenna nanoparticles and lines) nested in two kinds (300 and 470 nm slit opening) of nanoslits. FDTD-calculations suggest that the UC enhancement and the polarization effects resulted from different electric field modes activated by different polarizations (Chapter 6).

We hope that the fabrication and engineering the plasmonic and photonic light trapping material could benefit the silicon solar cell energy conversion efficiency. The SP enhanced UC could bring more insight about the plasmonic-excitation-emission interaction.

### 7.2 Outlook and future direction

The application of plasmonic nanostructures will continue to gather more research interest, due to its extraordinary light manipulation capability; especially, but not limited in the field of improved thin film photovoltaic and enhanced energy conversion. The different plasmonic nanostructures have to be optimized for a specific type of photovoltaic device. The integration of either plasmonic or photonic structure with the silicon photovoltaic requires to be utilized effectively, since not only the optical property, but also the electrical property of the devices is very important for archiving overall

improved energy conversion efficiency. Another important aspect of the nanostructured photovoltaic devices is that the total material and fabrication cost has to be reasonable and applicable in a large scale production in the real life application.

As for the proof of concept, the integration of upconverters in solar cell application has been demonstrated in literature[1-3] to minimize energy losses due to the spectral mismatch between the photovoltaic and incident solar spectrum. Plasmonic enhanced upconversion concept has been shown great enhancement[4,5] for potential energy conversion applications. The fabrication of a highly efficient luminescent solar cell will be exciting to be explored in the future work; the plasmonic material is a promising material to overcome the low upconversion efficiency and small absorption cross-section of lanthanide for solar cell application. Moreover, a broadband absorption upconverters that could convert the sunlight efficiently in the near infrared region would be more benefit for the solar cell energy conversion application. The tunable enhanced upconversion with plasmonic structures based on our work would also provide potential applications to other field, such as plasmonic laser[6, 7] and photovoltaic etc.

**7.3 Reference**

(1) Huang, X.; Han, S.; Huang, W.; Liu, X. Enhancing Solar Cell Efficiency: The Search for Luminescent Materials as Spectral Converters. *Chem. Soc. Rev.* **2013,** *42*, 173-201.

(2) van Sark, W.; de Wild, J.; Rath, J.; Meijerink, A.; Schropp, R. E. Upconversion in Solar Cells. *Nanoscale Research Letters* **2013,** *8*, 81

(3) Zhou, Z.; Wang, J.; Nan, F.; Bu, C.; Yu, Z.; Liu, W.; Guo, S.; Hu, H.; Zhao, X.-Z. Upconversion Induced Enhancement of Dye Sensitized Solar Cells Based on Core-Shell Structured β-$NaYF_4$:$Er^{3+}$, $Yb^{3+}$@$SiO_2$ Nanoparticles. *Nanoscale* **2014,** *6*, 2052-2055.

(4) Aouani, H.; Rahmani, M.; Navarro-Cia, M.; Maier, S. A. Third-Harmonic-Upconversion Enhancement from a Single Semiconductor Nanoparticle Coupled to a Plasmonic Antenna. *Nat Nano* **2014,** *9*, 290-294.

(5) Zhang, W.; Ding, F.; Chou, S. Y. Large Enhancement of Upconversion Luminescence of $NaYF_4$:$Yb^{3+}$/$Er^{3+}$ Nanocrystal by 3D Plasmonic Nano-Antennas. *Adv. Mater.* **2012,** *24*, 236-241.

(6) Shi, C.; Soltani, S.; Armani, A. M. Gold Nanorod Plasmonic Upconversion Microlaser. *Nano Lett.* **2013,** *13*, 5827-5831.

(7) Zhou, W.; Dridi, M.; Suh, J. Y.; Kim, C. H.; Co, D. T.; Wasielewski, M. R.; Schatz, G. C.; Odom, T. W. Lasing Action in Strongly Coupled Plasmonic Nanocavity Arrays. *Nat Nano* **2013,** *8*, 506-511.

# Appendix A

## A.1 Supporting Information (SI): Optimizing Plasmonic Silicon Photovoltaics with Ag and Au Nanoparticles Mixtures

### A.1.1 Experiment data

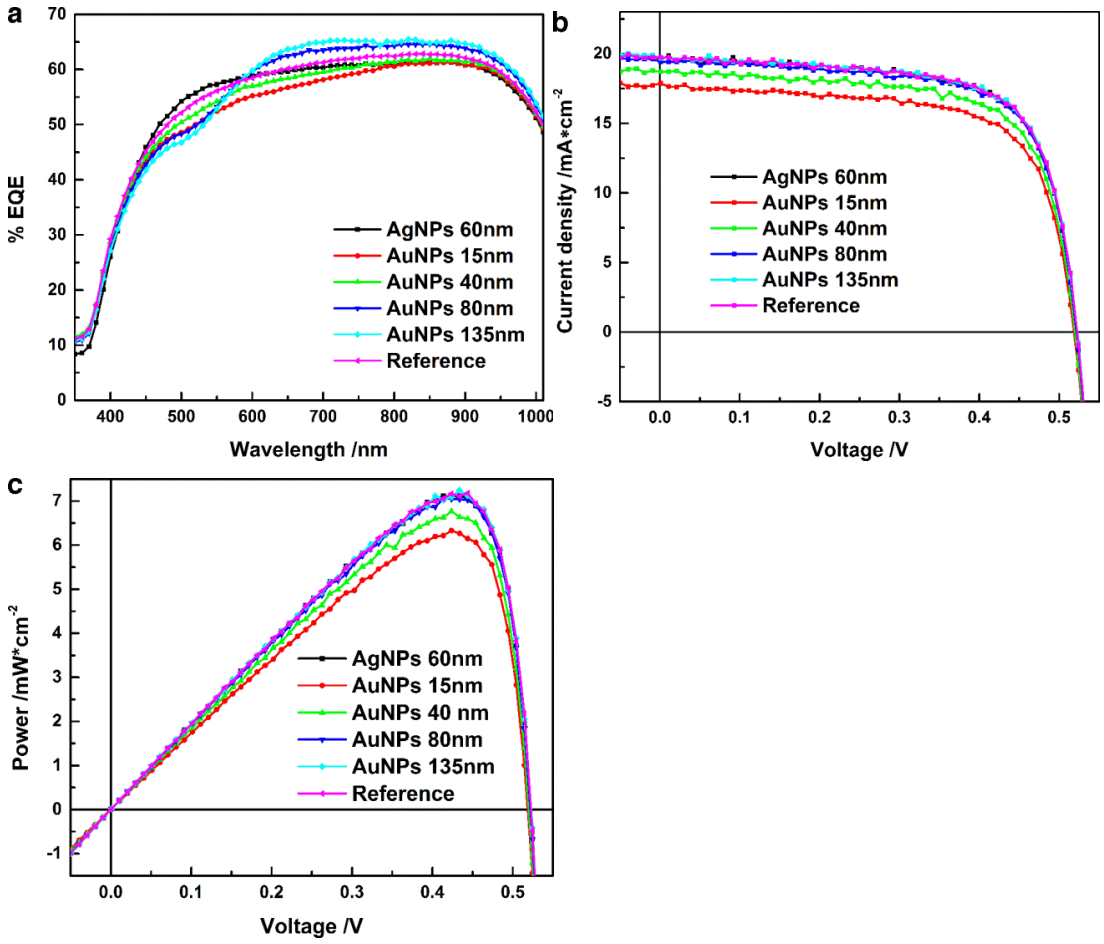


**Figure A−SI−1** (a) EQE% measured for NPs-modified and reference Si PVs under monochromatic light, with 10 nm steps, on the same device (as shown in Figure 3−1 Example of Au and Ag NPs modified Si photovoltaic device. The lanes were modified with 15, 40, 80, 135nm Au NPs and 60nm Ag NPs, respectively. The references were taken just beside each modified area, as indicated in the Figure. of the manuscript). (b) Si PV current-voltage (IV) curve under white light illumination (c) power under white light illumination before and after NPs

immobilization. Surface coverage (calculated from SEM images at several random places) for 60nm AgNPs is 7.1 ± 1.2 $\mu m^2$; for 15, 40, 80 and 135 nm AuNPs are 298 ± 35, 39.8 ± 2.2, 5.4 ± 1.5 and 7.9 ± 3.1 $\mu m^{-2}$, respectively.

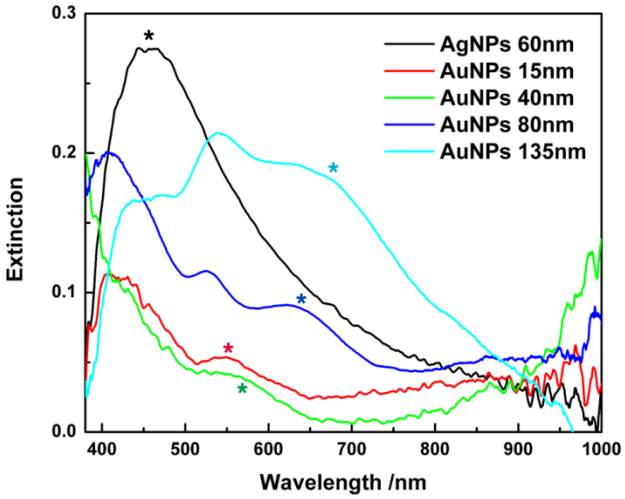


**Figure A−SI−2** Measured extinction of NPs immobilized on Si PV device from reflectance. The broad SPR peaks are indicated (*) on the graph for each difference size and type of NPs.

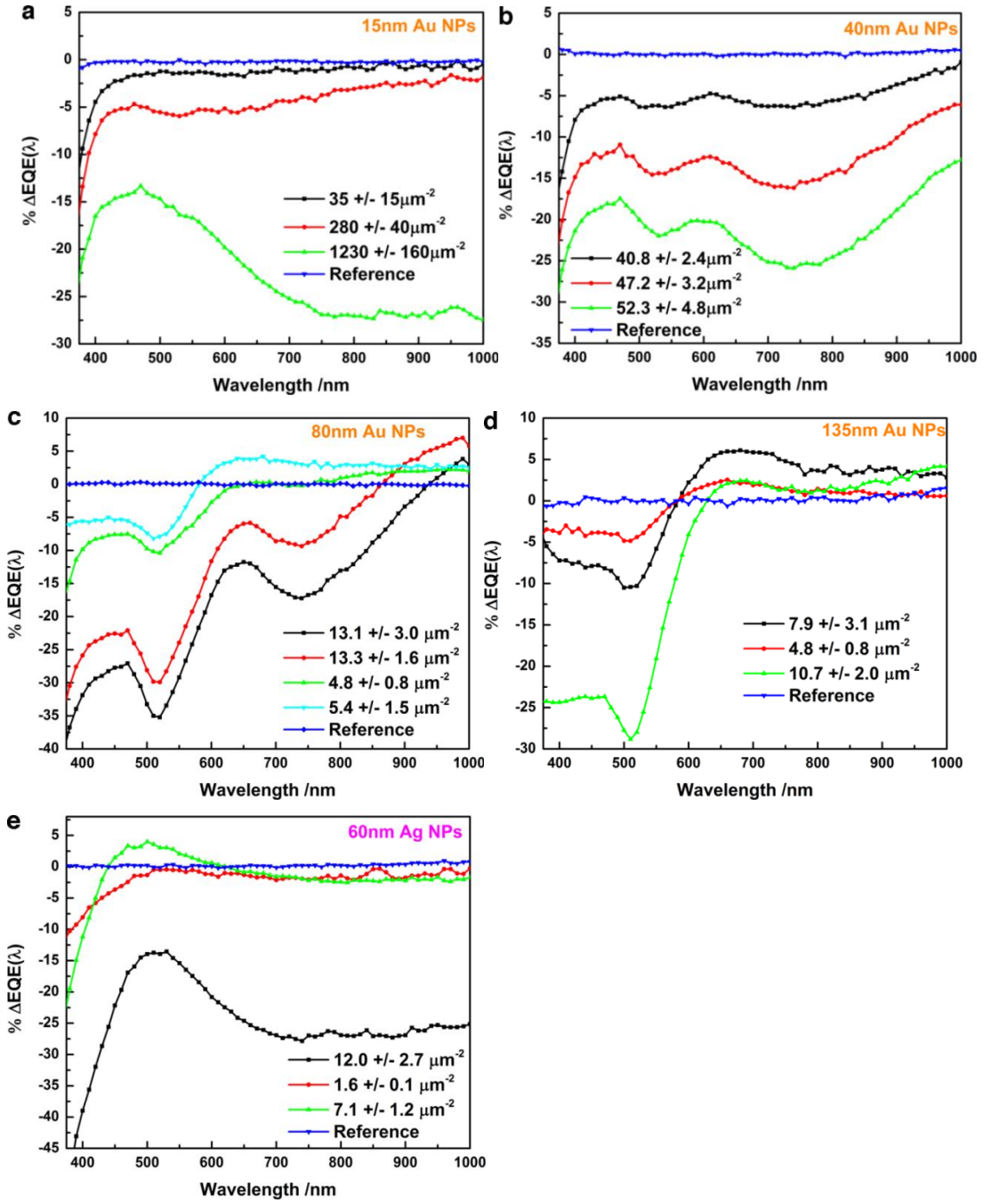


**Figure A−SI−3** %ΔEQE(λ) for (a) 15 nm (b) 40 nm (c) 80 nm, (d) 135 nm Au NPs and (e) 60 nm Ag NPs modified Si PV. The surface coverage (from SEM images at 3~4 random places) is indicated for each type of NPs. Reference in each case is one of the reference lane measured (without NPs) compared to another reference lane (without NPs) on the same Si PV device.

**A.1.2 FDTD simulation:**

The FDTD simulation model is simply applied as Lim. at el, proposed in the reference 11 to demonstrate the enhancement profile. Basically, the multi-coefficient models (MCMs) are used for Ag and Au material model fitting and the solar spectrum range from 400 nm to 1100 nm. The absorbed powers inside Si were calculated from the difference of two power monitors which located at the Si PV surface and 500 nm below the surface (doping of depth of the Si PV). The %ΔEQE(λ) is calculated from the relative absorption enhancement inside Si in the presence and absence of NPs. As for the Ag and Au combined NPs system, the simple individual NP model system is still valid, assuming that there is no significant aggregation on the surface; Ag and Au NPs are distanced enough that there is no significant particle to particle interference at the SPR. Thus, the EQE% enhancement profile would be shown as addition from the individual Ag NPs in the blue part and Au NPs in the red part.

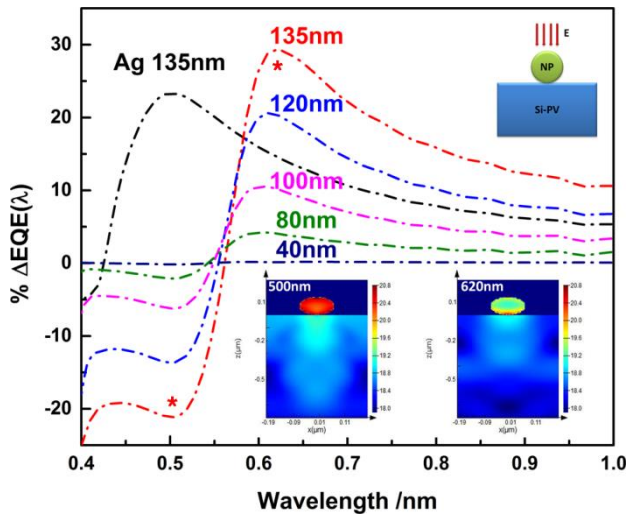


**Figure A−SI−4** FDTD simulated %ΔEQE(λ) for different sizes and types of NPs-modified Si PVs (Ag NPs modified is shown as a black curve, the rest are Au NPs modified Si PV). Note that the 135 nm Ag NPs modified Si PV (%ΔEQE(λ) normalized by a factor of 0.5) is shown here since the simulated SPR is more close to the experimental result. The light absorption intensity inside Si at 500 nm and 620 nm (indicated by (*) on the graph) for the 135 nm Au NPs modified Si PV are presented as insets. The log scalar color bars are adjusted to better compare the pictures to the absorption profile.

# Appendix B

## B.1 Comparison of Ag and $SiO_2$ Nanoparticles for Light Trapping Applications in Silicon Thin Film Solar Cells

*Appendix B is published. Theuring, M.; Wang, P. H.; Vehse, M.; Steenhoff, V.; von Maydell, K.; Agert, C.; Brolo, A. G., Comparison of Ag and Sio2 Nanoparticles for Light Trapping Applications in Silicon Thin Film Solar Cells. J. Phys. Chem. lett.* ***2014****, 3302-3306. Copyright: Reproduced with permission.*

Plasmonic and photonic light trapping structures can significantly improve the efficiency of solar cells. This work presents an experimental and computational comparison of identically shaped metallic (Ag) and non-metallic ($SiO_2$) nanoparticles integrated to the back contact of amorphous silicon solar cells. Our results show comparable performance for both samples, suggesting that minor influence arises from the nanoparticle material. Particularly, no additional beneficial effect of the plasmonic features due to metallic nanoparticles could be observed.

### B.1.1 Introduction

The design of low-cost solar cells with high power conversion efficiencies (PCE) has been one of the key challenges in energy technology in the past decades. Nanotechnology is a driving force in this research field. For instance, increased efficiency was demonstrated for organized arrays of dielectric nanoparticles (NPs) in the front and back side of thin film solar cells.[1-4]Also metallic NPs have shown great promise as scattering structures in thin film solar cells to enhance light absorption within the localized surface plasmon resonance (SPR) region.[5-8]However, when integrated at the front end of the cell, the characteristic energy losses associated to metals limit the solar cell performance.[9, 10] On the other hand, plasmonic structures placed at the back of a thin film solar cell have been demonstrated to enhance photocurrents.[11-14]

The beneficial properties of plasmonic structures in solar cells remain a controversial topic. Computational work, carried out by van Lare et al.,[15] showed that silver NPs covered with a transparent conductive oxide (TCO) and incorporated in the back contact of silicon thin film solar cells show a lower performance compared to a TCO layer with the same surface texture but without the silver NPs. It was concluded that the silicon/TCO interface is the main cause for the light trapping process. Furthermore, parasitic absorption due to plasmonic effects limits the beneficial properties of metallic NPs.[16] Solar cells modified with non-metallic structures should therefore outperform plasmonic solar cells. However, other groups have shown deviating results where plasmonic structures yielded higher efficiencies.[6, 7, 17]

This work attempts to solve this controversy by providing a comparative study on the effect of metallic and dielectric NPs on the performance of hydrogenated amorphous silicon (a-Si:H) solar cells. Ag and $SiO_2$ structured samples were fabricated by nanosphere lithography to ensure that the shape of the NPs was identical for both materials. With this approach, we want to determine experimentally whether plasmonic scattering structures offer advantages over non-metallic structures for this solar cell design. Besides additional parasitic absorption from the plasmonic structure, only minor differences were found between the two materials. Using finite-difference time-domain (FDTD) simulations, the similar scattering characteristics of the two samples were

visualized. Our findings confirm that the interface textures are the main contribution for light trapping in this solar cell configuration.

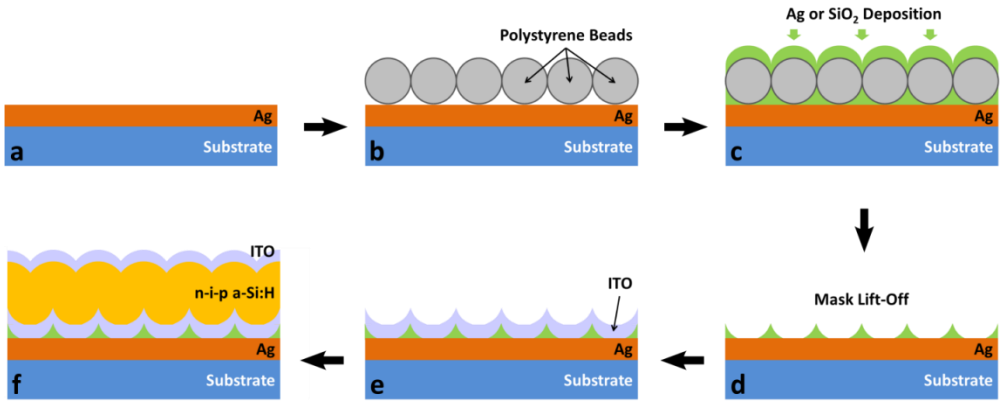


**Figure B−1** Fabrication process of the nanostructure and n-i-p a-Si:H solar cell. A glass sheet coated with a metal back contact (30 nm Al / 50 nm Ag) is used as a substrate (a). A monolayer of polystyrene beads is deposited as an evaporation mask (b), followed by an electron beam evaporation of either Ag or $SiO_2$ (c). After the lift-off process, a lattice of hexagonally packed pyramid NPs is formed (d). Subsequently, the NPs are encapsulated in a layer of ITO (e). The layers of the a-Si:H solar cell in n-i-p configuration are fabricated by plasma-enhanced chemical vapor deposition followed by an ITO front electrode (f).

### B.1.2 Result and discussion

The sample fabrication was carried out as depicted in Figure B−1. For the nanosphere lithography step, a monolayer of polystyrene (PS) beads in hexagonal packing was used as an evaporation mask.[18] The nanosphere mask fabrication process has also been employed in previous works on thin-film organic solar cells to integrate large area plasmonic sub-wavelength holes[19, 20] and nanostructured back electrodes.[21] This method allowed a homogenous coating of substrates up to 100 $cm^2$ (Figure B−1a) with only minor defects in the hexagonal lattice. After the lift-off process, three-sided pyramidal NPs with an edge length of approximately 200 nm (see Figure B−2b and c) are obtained. Silver is commonly used in plasmonic solar cells because of its high scattering efficiency in the red spectral region due to SPR.[11] $SiO_2$ was picked exemplarily as dielectric material because of its low absorption in the visible range. The NPs size and the

periodicity are optimized for SPR scattering in the red-region of the visible spectrum region inside the cell.[11, 22, 23]

A flat glass substrate and a textured substrate, both coated with a silver back contact, were used as references. The commercially available textured substrate consists of a glass sheet covered with a wet-etched rough layer of fluorine doped tin oxide. NP and reference substrates were covered with 70 nm of indium tin oxide (ITO) in order to prevent silver contamination of the processing chambers during the solar cell fabrication and to minimize plasmonic absorption[16] in the back contact. Scanning electron micrographs (SEM) of focused ion beam (FIB) milled cross sections of the different cells are shown in Figure B−2d-g. Figure B−2 illustrates that the a-Si:H layers grow isotropically, resulting in a broadening of the particle texture and ultimately in a dome-shaped surface.

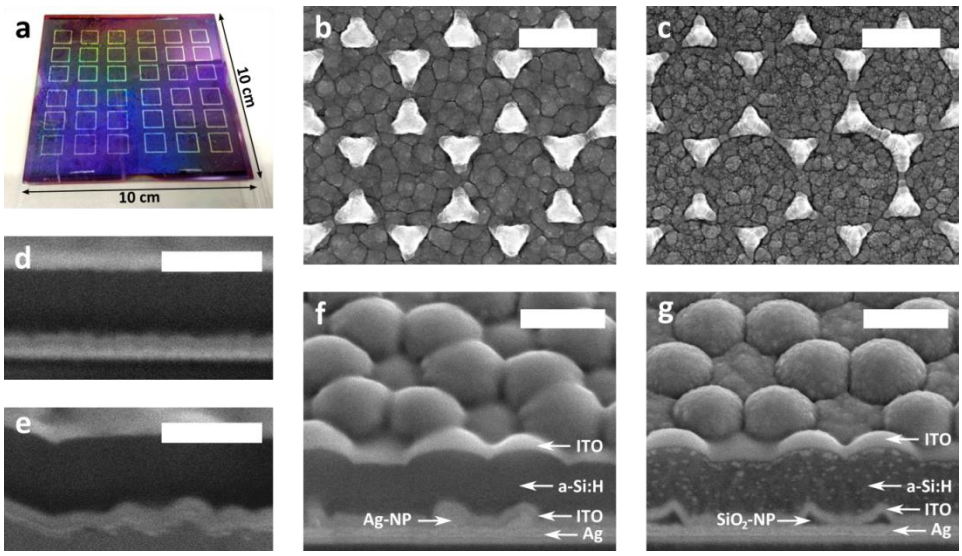


**Figure B−2** (a) Photograph of a-Si:H n-i-p solar cell on a 10 x 10 cm² substrate modified with NPs. (b,c) SEM images of Ag-NPs (b) and $SiO_2$-NPs (c), respectively. (d-g) Cross section SEM images of n-i-p a-Si:H solar cells fabricated on different substrates imaged at 45 degrees tilt: flat (d), textured (e), Ag-NPs (f) and $SiO_2$-NPs (g). (f) and (g) show the solar cell surface in the upper half of the image. White dots in a-Si:H layer in (g) originate from milling process. Scale bars in all SEM images are 500 nm.

| | $J_{SC}$ [mA/cm²] | $V_{OC}$ [V] | FF [%] | PCE [%] |
|---|---|---|---|---|
| Ag-NP | 12.5 | 0.901 | 64.9 | 7.33 |
| $SiO_2$-NP | 12.7 | 0.885 | 62.2 | 7.01 |
| Textured | 11.9 | 0.889 | 66.0 | 6.99 |
| Flat | 10.8 | 0.897 | 62.2 | 6.06 |

**Table B−1** Short circuit current density ($J_{SC}$), open circuit voltage ($V_{OC}$), fill factor (FF) and power conversion efficiency (PCE) comparison of the different types of n-i-p a-Si:H solar cells. $J_{SC}$ was determined by convolution of the EQE and the AM1.5G spectrum. $V_{OC}$ and FF were obtained from current density - voltage measurements (details see the method section in the SI file).

Table B−1 lists the devices characteristics from four different solar cells. The best PCE was obtained with the Ag-NPs, although the photocurrent was higher for the $SiO_2$ sample. The electrically insulating $SiO_2$-NPs are most likely the reason for a higher series resistance and decreased charge separation in this device. Figure B−3a depicts the external quantum efficiency (EQE) and absorption (1-R) measurements for the four different solar cells. In contrast to the flat substrate, the textured reference and the NPs samples show no pronounced Fabry-Perot resonances.[23] The light incident upon the cell is scattered by both the front and the back side interfaces causing an EQE enhancement for wavelengths above 550 nm compared to the flat reference. Comparing all textured cells, the highest quantum efficiencies are found for the NPs samples. Here, the cell absorption (1-R) is further enhanced for almost the entire investigated spectrum and the EQE increases accordingly. For wavelengths bellow 500 nm, the absorption coefficient of a-Si:H is high and photons are absorbed before reaching the back contact. Hence, the improvements in this region found for the nanoparticle structures can be attributed to better light in-coupling at the front interface.[23]

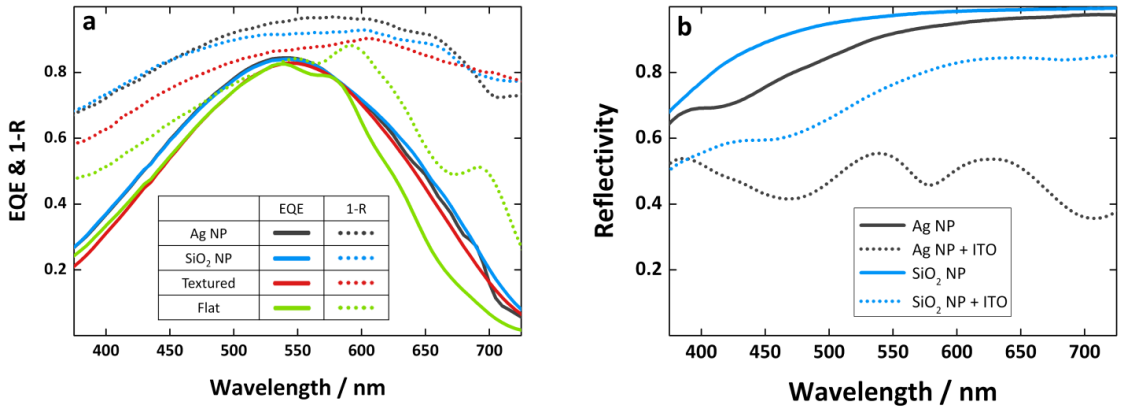


**Figure B−3** (a) EQE and total cell absorption (1-R) measurements for a-Si:H n-i-p cells on different substrates as indicated in the plot. (b) Measured reflectivity of substrates coated with Ag-NPs and $SiO_2$-NPs with and without the ITO buffer layer.

Comparing the Ag or $SiO_2$-NP samples, the EQE curves show very similar characteristics. However, for wavelengths > 600 nm, we measured a slightly higher EQE for the $SiO_2$ sample. Due to the lower absorption coefficient of the a-Si:H at longer wavelengths, a significant amount of light reaches the back contact. Therefore, a highly reflecting back contact is required to maximize the PCE. For wavelengths between 450 nm and 680 nm, the Ag-NPs sample absorbs more light than the cell modified with $SiO_2$-NPs. In the same range, the latter shows similar or even higher quantum efficiencies. As both cell geometries were identical, we assigned the decreased back contact reflectivity to an increase of the parasitic absorption by the Ag-NPs.

Figure B−3b shows the reflectivity of both Ag-NPs- and $SiO_2$-NPs-modified substrates without and with the ITO cover layer (see Figure B−1d and Figure B−1e, respectively). High reflectivity is found for the relevant part of the spectrum for both substrates without ITO. In the presence of the buffer layer, the reflectivity decreases significantly as a result of additional absorption in the structure. This especially applies to the Ag-NPs sample, indicating the occurrence of strong plasmonic interaction[15] as expected for nanostructured metal surfaces.

In order to investigate the detailed characteristics of the absorption distribution, we carried out FDTD simulations of the nanostructured solar cells (see simulation domain in Figure B−4a). Figure B−4b shows the computed EQE and 1-R data being in good

agreement with our experimental findings: The calculated EQE is inferior for the Ag-NPs device, although the total cell absorption is higher. Exemplarily, the calculated absolute power flux density at 600 nm excitation wavelength in the z- and x-planes (see indications in Figure B−4a) are plotted in Figure B−4c and Figure B−4d, respectively. The simulation indicates that strong field enhancements, are found mainly in the ITO layer adjacent to the Ag-NPs. As a consequence, more light is absorbed in this region, which reduces the reflectivity of the back contact. Apart from that, the absorption distributions in the silicon layers resemble each other (see Figure B−4d). The simulation shows that light is focused in an area above the particles independent of the NPs material.

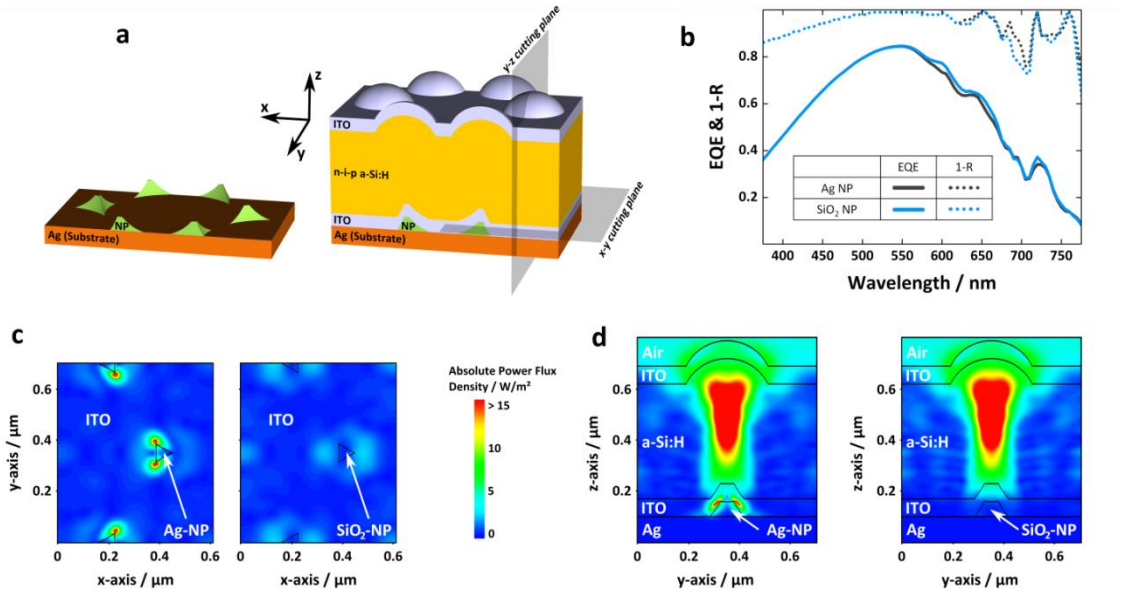


**Figure B−4** (a) Left: geometric structure of the simulated back contact; right: domain of the simulated n-i-p a-Si:H solar cells. (b) Simulated EQE and 1-R data of n-i-p a-Si:H solar cells with Ag and $SiO_2$ NPs in the back contact. EQE is calculated from the absorption in the intrinsic a-Si:H layer. (c,d) Absolute power flux density in the xy-plane at 50 nm above the substrate surface (c) and in the yz-plane at x ≈ 0.4 µm (d) for the Ag-NP and $SiO_2$-NP simulation. The excitation wavelength is 600 nm in all graphs. Note that for a clearer representation, the red areas in all images mark absolute power flux densities > 15 $W \cdot m^{-2}$.

As already mentioned, a barrier in the back contact (between the metal and the silicon layer) is required in the substrate configuration. But even without this layer, plasmonic field enhancements would only affect the doped section of the silicon. Charge carriers excited in this part of the cell are usually loss, due to increased defect densities.[24] For the same reason, the concept of absorption enhancement due to surface plasmon polaritons[25] is not applicable. The evanescent fields of plasmonic oscillations are highest close to the metal structures, where a barrier layer or the defect rich doped section of the absorber is located. While different photovoltaic device concepts[21, 26] may benefit from the field enhancements, silicon thin film solar cells are not preferential for plasmonic light trapping. Previous studies[5, 27, 28] have concluded that metal particles, applied to solar cell interfaces, contribute to an increased photocurrent not by local field enhancements but rather by an efficient forward scattering. Our work corroborates that by demonstrating dielectric scattering structures showing similar optical performance than metallic nanostructures.

### B.1.3 Conclusion

In summary, we were able to show that similar light trapping properties are obtained with identically shaped Ag-NPs and $SiO_2$-NPs features. As significant improvements were achieved with both NPs types over the textured reference, we conclude that the geometry of the structure has a much higher influence on the light trapping properties compared to its material. Specifically, the front side textures seem to have a major influence on the light distribution inside the cell. Finally, we deduce two major findings from our study: Firstly, one should aspire to use non-metallic particles because of the lower parasitic absorption associated with them. Secondly, but not of less importance, the influence of the light trapping structure on the electrical properties of the solar cell needs to be taken into account. In our example, the insulating nature of the $SiO_2$-NPs in the contact layer hinders an efficient charge extraction. Hence, shifting the SPR away from the absorber band gap or using non-metallic but conductive scattering features such as TCO structures might be the best options to optimize the performance of thin film silicon solar cells.

**B.1.4 Reference**

(1) Brongersma, M. L.; Cui, Y.; Fan, S. Light Management for Photovoltaics Using High-Index Nanostructures. *Nat. Mater.* **2014,** *13*, 451-460.

(2) Spinelli, P.; Verschuuren, M. A.; Polman, A. Broadband Omnidirectional Antireflection Coating Based on Subwavelength Surface Mie Resonators. *Nat. Commun.* **2012,** *3*, 692.

(3) Spinelli, P.; Macco, B.; Verschuuren, M. A.; Kessels, W. M. M.; Polman, A. $Al_2O_3/TiO_2$ Nano-Pattern Antireflection Coating with Ultralow Surface Recombination. *Appl. Phys. Lett.* **2013,** *102*, 233902/4.

(4) Mokkapati, S.; Catchpole, K. R. Nanophotonic Light Trapping in Solar Cells. *J. Appl. Phys.* **2012,** *112*, 101101.

(5) Atwater, H. A.; Polman, A. Plasmonics for Improved Photovoltaic Devices. *Nat. Mater.* **2010,** *9*, 205-213.

(6) Deceglie, M. G.; Ferry, V. E.; Alivisatos, A. P.; Atwater, H. A. Design of Nanostructured Solar Cells Using Coupled Optical and Electrical Modeling. *Nano Lett.* **2012,** *12*, 2894-2900.

(7) Tan, H.; Santbergen, R.; Smets, A. H. M.; Zeman, M. Plasmonic Light Trapping in Thin-Film Silicon Solar Cells with Improved Self-Assembled Silver Nanoparticles. *Nano Lett.* **2012,** *12*, 4070-4076.

(8) Morawiec, S.; Mendes, M. J.; Mirabella, S.; Simone, F.; Priolo, F.; Crupi, I. Self-Assembled Silver Nanoparticles for Plasmon-Enhanced Solar Cell Back Reflectors: Correlation between Structural and Optical Properties. *Nanotechnology* **2013,** *24*, 265601.

(9) Lim, S. H.; Mar, W.; Matheu, P.; Derkacs, D.; Yu, E. T. Photocurrent Spectroscopy of Optical Absorption Enhancement in Silicon Photodiodes via Scattering from Surface Plasmon Polaritons in Gold Nanoparticles. *J. Appl. Phys.* **2007,** *101*, 104309.

(10) Wang, P. H.; Millard, M.; Brolo, A. G. Optimizing Plasmonic Silicon Photovoltaics with Ag and Au Nanoparticle Mixtures. *J. Phys. Chem. C* **2014,** *118*, 5889-5895.

(11) Paetzold, U. W.; Moulin, E.; Pieters, B. E.; Carius, R.; Rau, U. Design of Nanostructured Plasmonic Back Contacts for Thin-Film Silicon Solar Cells. *Opt. Express* **2011,** *19*, A1219-A1230.

(12) Dai, W.; Yap, D.; Chen, G. Wideband Enhancement of Infrared Absorption in a Direct Band-Gap Semiconductor by Using Nonabsorptive Pyramids. *Opt. Express* **2012,** *20*, A519-A529.

(13) Ferry, V. E.; Munday, J. N.; Atwater, H. A. Design Considerations for Plasmonic Photovoltaics. *Adv. Mater.* **2010,** *22*, 4794-4808.

(14) Ferry, V. E.; Verschuuren, M. A.; van Lare, M. C.; Schropp, R. E. I.; Atwater, H. A.; Polman, A. Optimized Spatial Correlations for Broadband Light Trapping Nanopatterns in High Efficiency Ultrathin Film a-Si:H Solar Cells. *Nano Lett.* **2011,** *11*, 4239-4245.

(15) van Lare, M. C.; Lenzmann, F.; Polman, A. Dielectric Back Scattering Patterns for Light Trapping in Thin-Film Si Solar Cells. *Opt. Express* **2013,** *21*, 20738-20746.

(16) Haug, F.-J.; Söderström, T.; Cubero, O.; Terrazzoni-Daudrix, V.; Ballif, C. Plasmonic Absorption in Textured Silver Back Reflectors of Thin Film Solar Cells. *J. Appl. Phys.* **2008,** *104*, 064509.

(17) Spinelli, P.; Ferry, van de. Groep, J.; van Lare, M. C.; Verschuuren, M. A.; Schropp, R. E. I.; Atwater, H. A.; Polman, A. Plasmonic Light Trapping in Thin-Film Si Solar Cells. *J. Opt.* **2012,** *14*, 024002.

(18) Hulteen, J. C.; Treichel, D. A.; Smith, M. T.; Duval, M. L.; Jensen, T. R.; Van Duyne, R. P. Nanosphere Lithography: Size-Tunable Silver Nanoparticle and Surface Cluster Arrays. *J. Phys. Chem. B* **1999,** *103*, 3854-3863.

(19) Reilly, T. H.; van de Lagemaat, J.; Tenent, R. C.; Morfa, A. J.; Rowlen, K. L. Surface-Plasmon Enhanced Transparent Electrodes in Organic Photovoltaics. *Appl. Phys. Lett.* **2008,** *92*, 243304.

(20) Luhman, W. A.; Hoon Lee, S.; Johnson, T. W.; Holmes, R. J.; Oh, S.-H. Self-Assembled Plasmonic Electrodes for High-Performance Organic Photovoltaic Cells. *Appl. Phys. Lett.* **2011,** *99*, 103306.

(21) Niesen, B.; Rand, B. P.; Van Dorpe, P.; Cheyns, D.; Tong, L.; Dmitriev, A.; Heremans, P. Plasmonic Efficiency Enhancement of High Performance Organic Solar Cells with a Nanostructured Rear Electrode. *Adv. Energy Mater.* **2013,** *3*, 145-150.

(22) Micco, A.; Ricciardi, A.; Pisco, M.; La Ferrara, V.; Mercaldo, L. V.; Veneri, P. D.; Cutolo, A.; Cusano, A. Light Trapping Efficiency of Periodic and Quasiperiodic Back-Reflectors for Thin Film Solar Cells: A Comparative Study. *J. Appl. Phys.* **2013,** *114*, 063103/9.

(23) Ferry, V. E.; Polman, A.; Atwater, H. A. Modeling Light Trapping in Nanostructured Solar Cells. *ACS Nano* **2011,** *5*, 10055-10064.

(24) Shah, A. V.; Schade, H.; Vanecek, M.; Meier, J.; Vallat-Sauvain, E.; Wyrsch, N.; Kroll, U.; Droz, C.; Bailat, J. Thin-Film Silicon Solar Cell Technology. *Prog. Photovoltaics* **2004,** *12*, 113-142.

(25) Haug, F.-J.; Söderström, T.; Cubero, O.; Terrazzoni-Daudrix, V.; Ballif, C. Influence of the ZnO Buffer on the Guided Mode Structure in Si/ZnO/Ag Multilayers. *J. Appl. Phys.* **2009,** *106*, 044502.

(26) Luk, T. S.; Fofang, N. T.; Cruz-Campa, J. L.; Frank, I.; Campione, S. Surface Plasmon Polariton Enhanced Ultrathin Nano-Structured CdTe Solar Cell. *Opt. Express* **2014,** *22*, A1372-A1379.

(27) Harada, Y.; Imura, K.; Okamoto, H.; Nishijima, Y.; Ueno, K.; Misawa, H. Plasmon-Induced Local Photocurrent Changes in GaAs Photovoltaic Cells Modified with Gold Nanospheres: A Near-Field Imaging Study. *J. Appl. Phys.* **2011,** *110*, 104306.

(28) Diukman, I.; Orenstein, M. How Front Side Plasmonic Nanostructures Enhance Solar Cell Efficiency. *Sol. Energy Mater. Sol. Cells* **2011,** *95*, 2628-2631.

## B.2 Supporting information (SI): Comparison of Ag and $SiO_2$ Nanoparticles for Light Trapping Applications in Silicon Thin Film Solar Cells

*Theuring, M.; Wang, P. H.; Vehse, M.; Steenhoff, V.; von Maydell, K.; Agert, C.; Brolo, A. G., Comparison of Ag and Sio2 Nanoparticles for Light Trapping Applications in Silicon Thin Film Solar Cells. J. Phys. Chem. lett.* ***2014****, 3302-3306. Copyright: Reproduced with permission.*

### B.2.1 Experiment method

***Fabrication of Nanoparticle Substrates.*** 30 nm of Al and 50 nm of Ag were electron beam evaporated on flat glass substrates (Schott AF 32 eco) as a metallic back contact. Then, a monolayer of PS nanospheres (ordered from microParticles GmbH Berlin in an aqueous dispersion of 10 wt%) with a diameter of 700 nm was deposited on top of the substrate as an evaporation mask (Figure B−1b). Therefore, we diluted the PS dispersion with one part of $H_2O$ and two parts of ethanol. The substrates and a sacrifice glass slide of similar height were stored in a petri dish filled with $H_2O$, covering the substrate's surface. The NP dispersion was poured dropwise onto the sacrifice sample until the entire water surface was covered with a monolayer of PS beads. The water was then removed with a Pasteur pipette and the samples dried under incandescent light. To obtain the different types of NPs, 140 nm of Ag or $SiO_2$ were electron beam evaporated on the PS beads, followed by a lift-off in toluene (Figure B−1d) and a cleaning step by sonication in ethanol and blow drying with $N_2$. A 70 nm layer of ITO was deposited by DC magnetron sputtering on top of the NPs, serving as a diffusion barrier and optical spacer between the metallic/dielectric NPs and the a-Si:H (Figure B−1e).

***Solar Cell Fabrication and Characterization*****.** Solar cells were fabricated on all substrates in n-i-p configuration (deposition order: n-doped / intrinsic / p-doped) by plasma-enhanced chemical vapor deposition and in a shared process to ensure comparability. $SiH_4$, $H_2$ and $PH_3$ were used as precursors for the n-doped layer (30 nm), $SiH_4$ and $H_2$ for the intrinsic layer (400 nm) and $SiH_4$, $H_2$ and $B_2H_6$ for the p-doped layer (20 nm), respectively. An ITO layer of 70 nm thickness was used as a transparent front

electrode. All solar cells were annealed for 30 min at 160°C before characterization. The active cell area of the solar cells was defined by the size of the front contact to a square opening of 0.25 $cm^2$ using a marker pen and a lift-off process. Short circuit current densities ($J_{SC}$) were obtained from external quantum efficiency (EQE) measurements by convolution with the AM1.5G spectrum. Open circuit voltage ($V_{OC}$), fill factor (FF) and PCE were measured with a solar simulator under standard test conditions. Solar cells were attached to a spectrophotometer (Varian Cary 5000) using an integrating sphere for the reflectivity characterization. A Hitachi FB-2100 FIB was used to cut the cross section and a Hitachi S4800 FESEM was used to obtain scanning electron micrographs with an in-lens secondary electron backscattering detector and an accelerating voltage of 5 kV.

**B.2.2 FDTD simulation**

Optical material parameters were obtained by spectroscopic ellipsometry and subsequent modeling except for the Ag parameters, which were taken from the reference book[1] The software Sentaurus TCAD by Synopsys Inc. was used for the finite-difference time-domain (FDTD) simulation. To speed up the computation, calculations were partly performed on graphics processing units using the CUDA platform by Nvidia Inc. and the corresponding implementation from Acceleware Ltd. The simulation domain as shown in Figure B−4a was designed according to the experimental structure using basic geometrical shapes. For the electromagnetic field calculation a discretization (tensor mesh) of 6 nm in x and y directions and of 3 nm in z direction was applied. Individual simulations for each wavelength (step size 5 nm) were carried out with plane wave excitation. For the EQE calculation, only the absorption in the intrinsic layer and not in the doped layers was taken into account. The absorbed photon flux was related to the incident photon flux to obtain an absorption spectrum. The simulated EQE spectrum equals this absorption spectrum under the assumption that each absorbed photon generates one charge carrier pair which is perfectly extracted from the absorber layer.

(1) Palik, E. D., Handbook of optical constants of solids. Acad. Press: Boston u.a., 1997.

# Appendix C

## C.1 Supplementary information (SI): Cost-Effective Nanostructured Thin-Film Solar Cell with Enhanced Absorption

The following table shows the statistical data of the full series of seven honeycomb cells with 500 nm honeycomb diameter and thirteen textured reference cells, all fabricated under equal conditions.

| | $J_{SC}$ /mA·cm$^{-2}$ | $V_{OC}$ /mV | $FF$ /% | $\eta$ /% |
|---|---|---|---|---|
| Honeycomb | 10.50 ± 0.24 | 891 ± 9 | 61 ± 3 | 5.8 ± 0.3 |
| Textured Ref. | 9.69 ± 0.10 | 912 ± 11 | 64 ± 6 | 5.7 ± 0.6 |

**Table C−1** Average cell performance parameters and standard deviations of full experimental series of seven honeycomb and thirteen textured reference cells

# Appendix D

## D.1 Supplementary information (SI): Polarization-Dependent Extraordinary Optical Transmission from Upconversion Nanoparticles

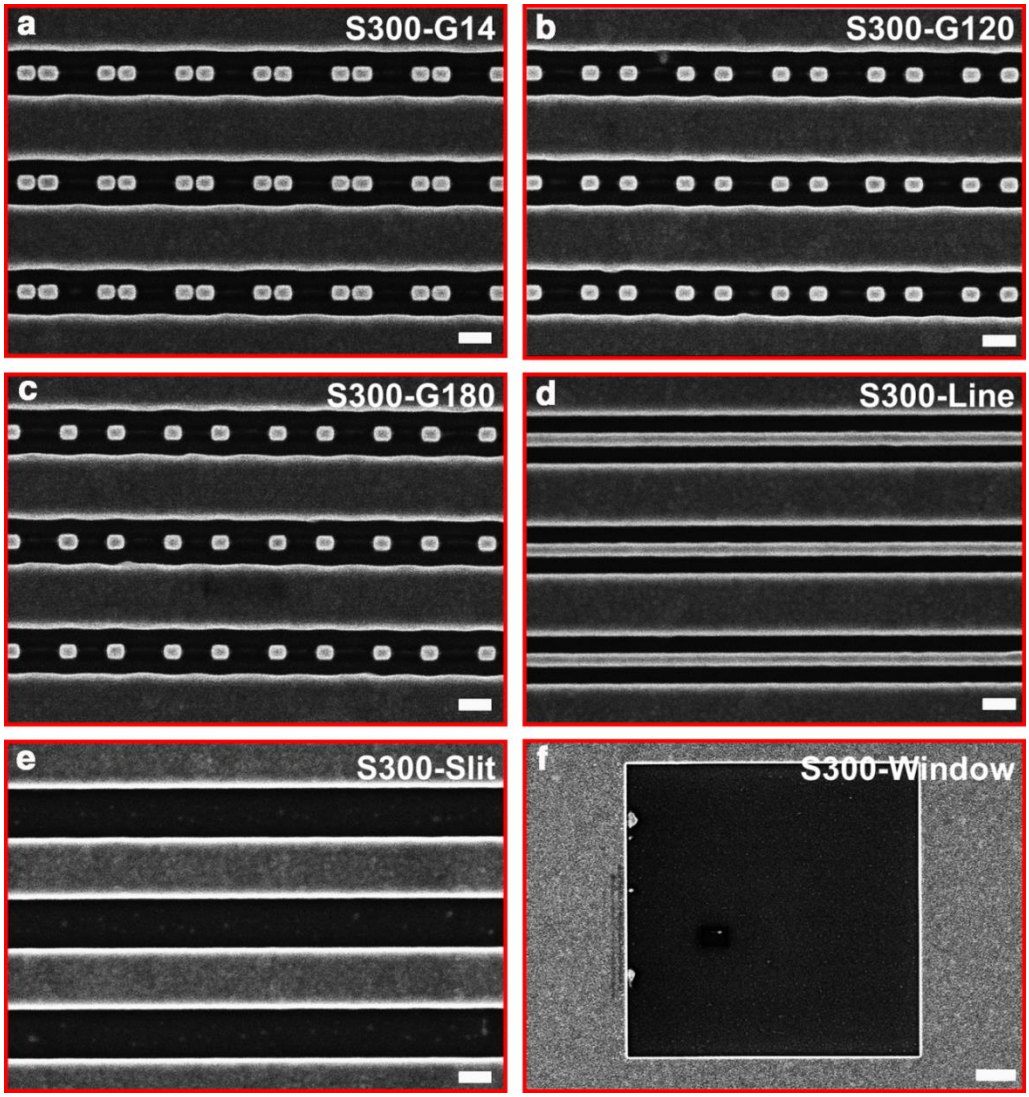


**Figure D−SI−1** SEM images: (a) S300-G14, (b) S300-G120, (c) S300-G180, (d) S300-Line, (e) S300-Slit, (f) S300-Window structures. Scale bars in (a-e) are 200 nm and (f) 1 μm, respectively

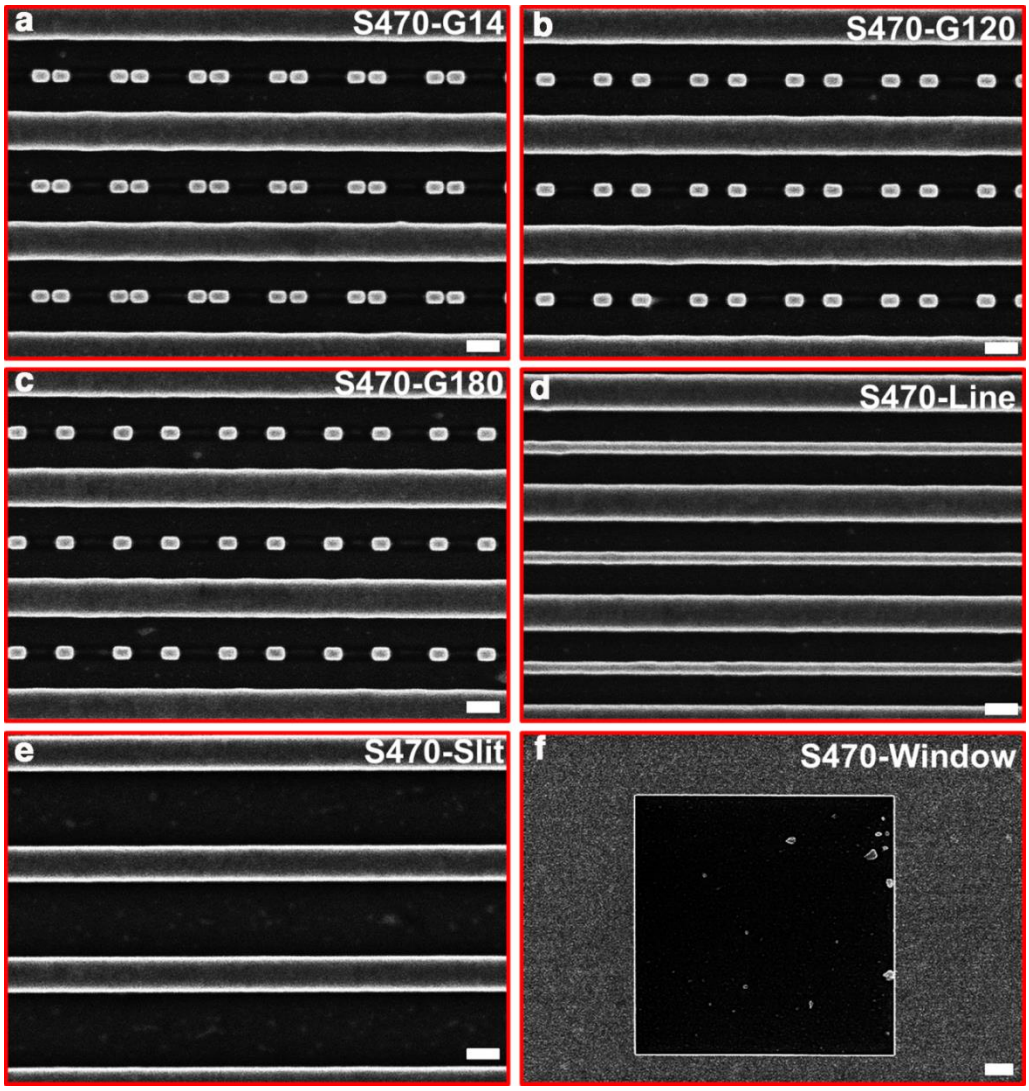


**Figure D−SI−2** SEM images: (a) S470-G14, (b) S470-G120, (c) S470-G180, (d) S470-Line, (e) S470-Slit, (f) S470-Window structures. Scale bars in (a-e) are 200 nm and (f) 1 μm, respectively

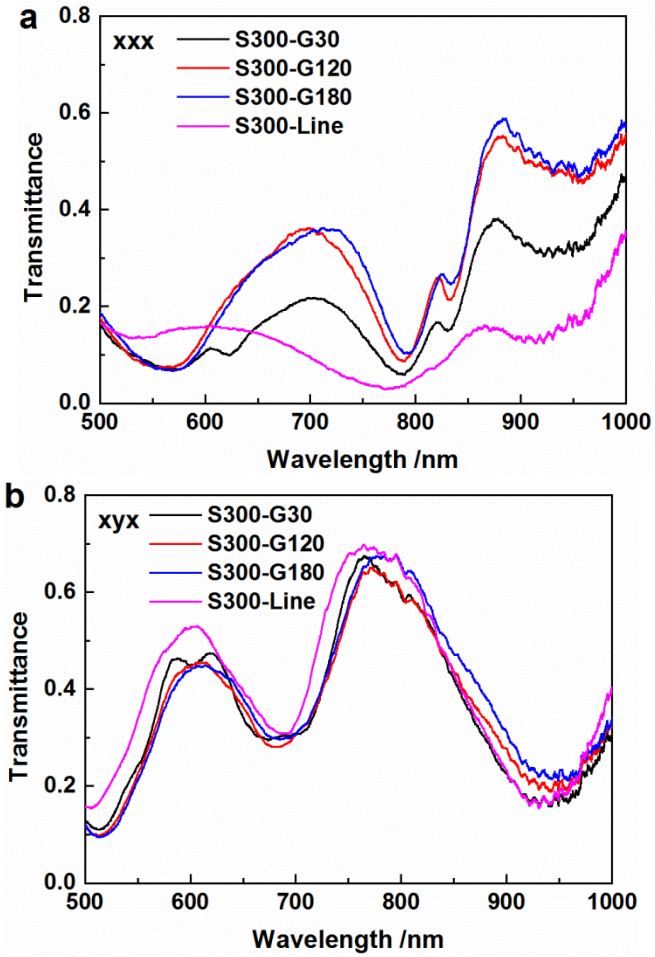


**Figure D−SI−3** Experiment measured white light transmittance spectra for S300-G30, S300-G120, S300-G180, and S300-Line array with (a) xxx and (b) xyx configuration, respectively.

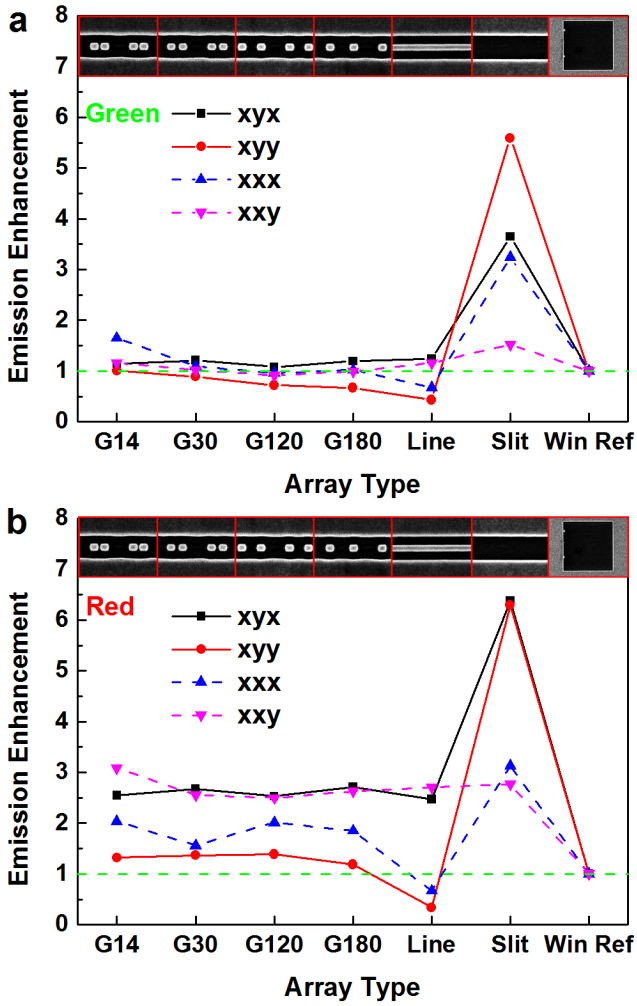


**Figure D−SI−4** Summary of the relative enhancement of green (a) and red emission (b) using the window as reference for each array ( $\frac{I^{UC}_{Structured}}{I^{UC}_{Win\ ref.}}$ ) with different measurement configuration (indicated on the graph).